CRANFIELD UNIVERSITY

Daniel Omatsola Gagar

Validation and Verification of the Acoustic Emission Technique for Structural Health Monitoring

School of Applied Sciences

PhD
Academic Year: 2012 - 2013

Supervisor: Professor Phil Irving

July 2013

CRANFIELD UNIVERSITY

School of Applied Sciences

PhD

Academic Year: 2012 - 2013

Validation and Verification of the Acoustic Emission Technique for Structural Health Monitoring

Supervisor: Professor Phil Irving
July 2013

Abstract

The performance of the Acoustic Emission (AE) technique was investigated to establish its reliability in detecting and locating fatigue crack damage as well as distinguishing between different AE sources in potential SHM applications.

Experiments were conducted to monitor the AE signals generated during fatigue crack growth in coupon 2014 T6 aluminium. The influence of stress ratio, stress range, sample geometry and whether or not the load spectrum was of constant or variable amplitude were all investigated. Timing filters were incorporated to eliminate extraneous AE signals produced from sources other than the fatigue crack. AE signals detected were correlated with values of applied cyclic load throughout the tests. Measurements of Time difference of arrival were taken for assessment of errors in location estimates obtained using time of flight algorithms with a 1D location setup.

It was found that there was significant variability in AE Hit rates in otherwise identical samples and test conditions. However common trends characteristic of all samples could be observed. At the onset of crack growth high AE Hit rates were observed for the first few millimetres after which they rapidly declined to minimal values for an extended period of crack growth. Another peak and then decline in AE Hit rates was observed for subsequent crack growth before yet another increase as the sample approached final failure.

The changes in AE signals with applied cyclic load provided great insights into the different AE processes occurring during crack growth. AE signals were seen to occur in the lower two-thirds of the maximum load in the first few millimetres of crack growth before occurring at progressively smaller values as the crack length increased. These emissions could be associated with crack closure. A separate set of AE signals were observed close to the maximum cyclic stress throughout the entire crack growth process. At the failure crack length AE signals were generated across the entire loading range.

Novel metrics were developed to statistically characterise variability of AE generation with crack growth and at particular crack lengths across different samples.

A novel approach for fatigue crack length estimation was developed based on monitoring applied loads to the sample corresponding with generated AE signals which extends the functionality of the AE technique in an area which

was previously deficient. It is however limited by its sensitivity to changes in sample geometry.

Experiments were also performed to validate the performance of the AE technique in detecting and locating fatigue crack in a representative wing-box structure. An acousto-ultrasonic method was used to calibrate the AE wave velocity in the structure which was used to successfully locate the 'hidden' fatigue crack. A novel observation was made in the series of tests conducted where the complex propagation paths in the structure could be exploited to perform wide area sensing coverage in certain regions using sensors mounted on different components of the structure. This also extends current knowledge on the capability of the AE technique.

Keywords:

Fatigue crack, Probability of Detection, Diagnostics, Prognostics

Acknowledgments

I would like to acknowledge the sponsorship for this project provided by the Cranfield University IVHM Centre and BAE Systems.

I would like to thank my supervisor Prof. Phil Irving for his constant support and guidance throughout this research programme. I would also like to thank Prof. Peter Foote for his continued mentorship as well.

The collaborations made in this project would have not been possible without the commitment of Jim McFeat, Dr. Marcias Martinez and Prof. Ian Jennions. For that I am particularly grateful.

I very much appreciate the camaraderie of all my colleagues at the IVHM Centre and the Damage Tolerance group which was always a source of motivation.

I would finally like to thank my wife Olubukola for being my inspiration throughout this journey.

Contents

List of Figures

List of Tables

List of Publications

Gagar, D., Irving, P., Jennions, I., Foote, P., Read, I., McFeat, J. (2011), "Development of probability of detection data for structural health monitoring damage detection techniques based on acoustic emission", *8th International Workshop on Structural Health Monitoring*, Stanford, CA.

Gagar, D., Irving, P., Foote, P., McFeat, J. (2012), "Investigation of acoustic emission generation from fatigue cracks for structural health monitoring in 2014 aluminium alloy", *6th European Workshop on Structural Health Monitoring*, Dresden.

Gagar, D., Martinez, M., Yanishevsky, M., Rocha, B., McFeat, J., Foote, P., Irving, P. (2011), "Detecting and locating fatigue cracks in a complex wing-box structure using the acoustic emission technique: A verification study", *9th International Workshop on Structural Health Monitoring*, Stanford, CA.

List of Abbreviations

AE	Acoustic Emission
MT	Middle Tension Crack
NDI	Non Destructive Inspection
NDT	Non Destructive Testing
POD	Probability of Detection
SHM	Structural Health Monitoring
SEN	Single Edge Notch
TDOA	Time Difference of Arrival

Chapter 1

Introduction

1.1 Background

Structures such as airframes degrade via three major mechanisms: fatigue, environmental and accidental damage. For metallic structures, most of these damage mechanisms eventually manifest themselves as cracks which must be detected and rectified during maintenance. If gone unnoticed, these cracks can propagate up to a critical length where catastrophic failure will occur.

Aircraft maintenance is currently based on either the Safe Life or Damage Tolerant paradigms. In the Safe Life approach, the aircraft is designed to serve for a period as long as the conservatively predicted life until the onset of detectable damage, where the aircraft is taken out of service. This leaves the potential period of crack growth in the structure redundant. Inspections are however performed at fixed intervals during the service life using manual Non Destructive Inspection (NDI) techniques to check for inadvertent damage which will often require disassembly of complex structures to check for damage. The presence of damage will prompt early withdrawal from service.

The Damage Tolerant approach on the other hand allows a structure to safely sustain damage until repair can be done. This is performed at calculated intervals of service based on a worst-case prediction of crack growth, also using manual non-destructive inspection (NDI) techniques. If damage is detected, the structure is repaired before the aircraft is reintroduced into service. This process is illustrated in a schematic of crack growth over the service life of an aircraft shown in Figure 1-1, with indications of the discrete points of inspection after the threshold for minimum detectable damage has been exceeded.

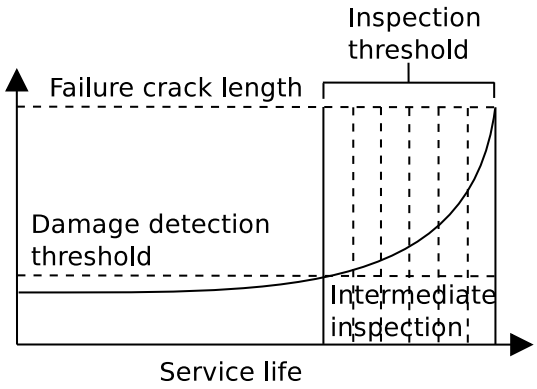

Figure 1.1: Damage tolerant approach to aircraft maintenance using NDT techniques

Frequently, the result of a scheduled inspection is that no damage is found. Thus, cost and down-time of the unnecessarily. This provides the motivation vehicle is incurred for development of Structural Health Monitoring (SHM) technologies where sensors are permanently located in structures that can perform continuous or on-demand diagnosis and damage detection without the need for a human inspector to manually intervene in the structure. This is an enabler for condition based maintenance where a structure is only taken out of service when a maintenance action is needed, hence eliminating costly and unnecessary precautionary inspections.

The Acoustic Emission (AE) technique is one of several technologies being developed for the purpose of SHM. This technique is particularly attractive because it operates passively and requires fewer sensors to cover a relatively wide area compared with other SHM techniques. Application of this technique to replace or augment manual NDT will however require equivalent levels of reliability and confidence in damage detection. This is currently largely unknown with no equivalent representation of their probability of detection (POD) as employed in quantitatively characterising the performance of NDT techniques. This type of information is essential if they are to be accepted as a credible method for use in real applications.

1.2 Research Aims and Objectives

This work aims to perform a validation and verification study on performance of the AE technique in SHM applications. The objectives are:

1. To quantitatively characterise the performance of the Acoustic Emission (AE) technique to establish probability of detection.
2. To characterise the factors controlling AE generation during fatigue crack growth.
3. To validate the performance of the AE technique in detecting and locating fatigue crack in realistic structures.

1.3 Thesis Structure

An overview of the thesis structure is given in Figure 1-2, where two strands of the theme can be seen in AE performance verification in coupon test samples and AE performance validation in a realistic structure. In Chapter 2, a literature review focused on the AE technology, its application in damage detection, location and characterisation as well as the sources of variability in AE monitoring was conducted. Fatigue crack damage in metallic structures was also reviewed.

The experimental methodology employed for both tests performed on coupon samples as well as those on a representative wing-box structure are given in Chapter 3. Test variables and testing configurations are also given here.

The results for the tests performed on the coupon samples are given in Chapters 4 and 5 in terms of fatigue crack detection and location as well as AE source classification. Chapter 6 provides the results from a series of 'blind' tests performed to detect and locate fatigue crack in complex wing-box structure.

Chapter 7 discusses the results presented in the preceding chapters in the context of AE performance verification and validation. The conclusions drawn and contributions made from the work in this thesis are presented in Chapter 8.

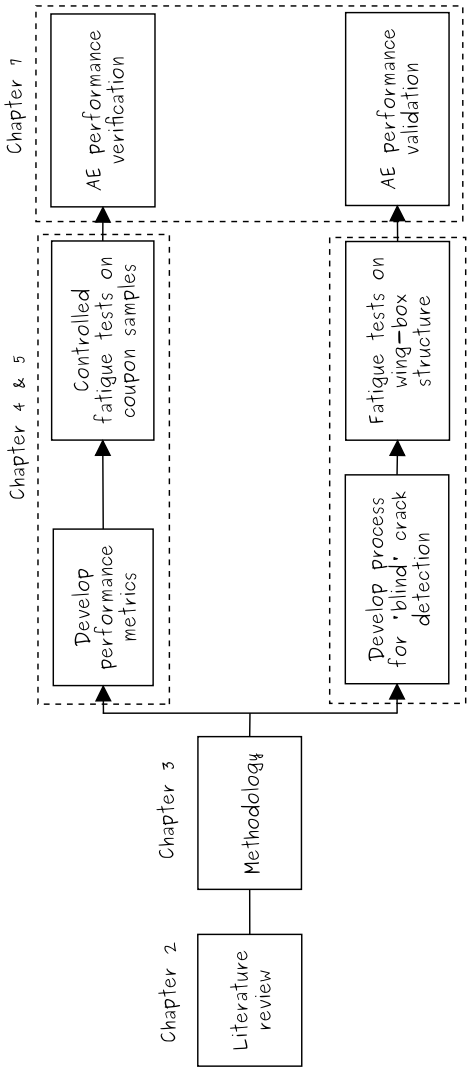

Figure 1.2: Thesis structure overview

Chapter 2

Literature Review

2.1 Introduction

A literature review focused on the AE technology, its application in damage detection, location and characterisation as well as the sources of variability in AE monitoring was conducted in this chapter. Fatigue crack damage in metallic structures is the primary failure mode considered in this study and a review was also conducted.

2.2 Acoustic Emission Monitoring

Acoustic Emissions (AE) are a burst of ultrasound signals with significant energy levels between about 100 kHz to 1 MHz which arise due to mechanical deformation of a material which leads to a transient release of stored elastic energy from that localized region [1]. These AE signals propagate through the object subjected to load and are dependent on the material properties, geometry and the source characteristics [2]. There are two typical types of AE signals; continuous and burst [2; 3] as illustrated in Figure 2-1. The Burst AE signals are characterised by a quick rise to maximum amplitude close the start of the signal and then a gradual decline with increase in time. These are qualitatively associated with discrete AE events. The continuous signals are characterised by quasi-random amplitude levels for the entire duration of the signals and are qualitatively associated with time-overlapping AE events.

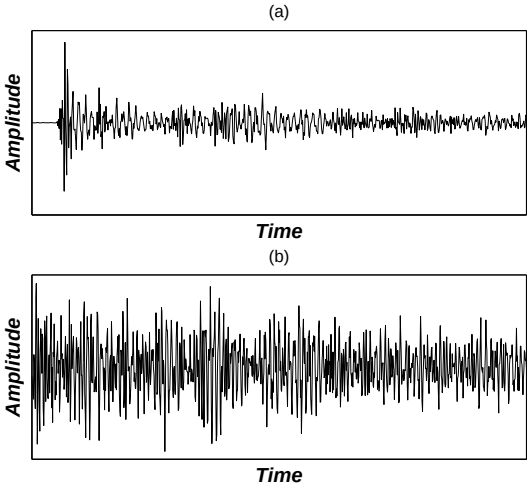

Figure 2.1: Typical AE signals (a) burst and (b) continuous

2.2.1 Wave Propagation Theory

The subject of wave propagation is well understood across several disciplines which apply electromagnetic or mechanical waves for transfer of energy; details are available in literature [4; 5]. Acoustic emission signals are a type of sound wave which is classified as mechanical. Sound waves can travel in a variety of elastic media by means of particle motion which is governed by Navier's equations of elasticity given in Equation 2-1 [6]. This is a partial differential equation representing displacement in a linear, elastic, homogenous and isotropic body with an external force applied. Solutions for this equation need to be obtained which also satisfies the boundary conditions of the propagating medium [7].

$$(\lambda + \mu)u_{j,ij} + \mu u_{i,jj} + \rho f_i = \rho u_i \tag{2.1}$$

Where,

i,j - 1,2,3

u_i *- Cartesian components of the particle displacement vector*

λ, μ *- Material parameters representing elastic properties of the medium*

ρ *- Density of the material*

ρf_i *- Applied force*

Studies have been conducted to characterise wave propagation in finite, semi-finite and infinite media.

2.2.2 Infinite medium

Elastic waves in infinite media, commonly referred to as bulk or body waves because they propagate in the 'bulk' of the material, fundamentally exist as longitudinal (compression or primary) and transverse (shear or secondary) wave modes [2; 8]. Schematics of these 4 wave modes are illustrated in Figure 2-2 and Figure 2-3 respectively. The longitudinal wave mode propagates as a succession of compression, where there is an increase in the medium's density, and rarefaction (reduction of the medium's density) of inter-atomic spacing along the direction of wave travel. The transverse wave mode on the other hand propagates as an oscillatory shearing motion between successive atomic planes perpendicular to the propagation direction.

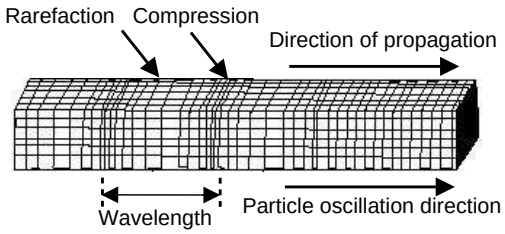

Figure 2.2: Longitudinal wave mode propagating in an infinite medium

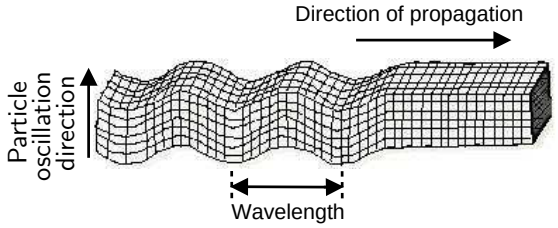

Figure 2.3: Transverse wave mode propagating in an infinite medium

The velocities of these wave modes are dependent on material properties as given by the following expressions [9].

$$C_L = \sqrt{\frac{E(1-v)}{p(1+v)(1-2v)}} \tag{2.2}$$

$$C_T = \sqrt{\frac{E}{2p(1+2v)}} \tag{2.3}$$

Where,

E - *Young's modulus*

ρ - *Density*

ν - *Poisson's ratio*

2.2.3 Semi-finite Medium

The introduction of boundaries causes interactions between the interfaces and the waves by way of reflection, refraction as well as conversions between modes which guide wave propagation [10]. Some examples of guided waves in semi-infinite media are Rayleigh, Love and Interface waves which include Sholte and Stonely waves.

Rayleigh Waves

These waves propagate along the plane surface of an elastic solid with the inter-atomic particles moving normal to the surface and the wave amplitude decreasing exponentially as the distance from the surface increases, as illustrated in Figure 2-4. An example can be found in waves travelling on the surface of water as a result of a stone thrown into it.

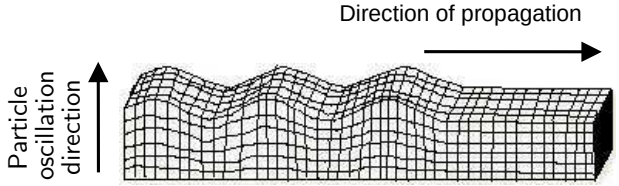

Figure 2.4: Rayleigh surface waves propagating in a semi-infinite medium

Interface Waves

These waves occur at the interface between two semi-infinite media. They are referred to as Stonely waves when the occur between two solid media as illustrated in Figure 2-5 and Scholte waves when they occur between a solid

and a liquid medium [11]. The amplitude of these waves decay rapidly with increased distance from the interface. They are also slightly dispersive, so that the waves at different frequencies propagate at different velocities [12]. An application for this kind of wave can be found in Non Destructive Evaluation (NDE) of boreholes.

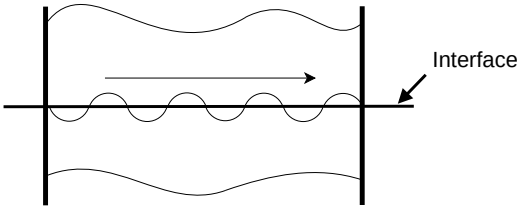

Figure 2.5: Stonely waves propagating at the interface between two solid semi-infinite media

Love Waves

These waves which can occur in semi-infinite media with an elastic layer [13]. They are similar to the transverse (shear) waves where displacement by the wave is perpendicular to the plane of wave propagation; however this is underpinned by particle movement is in the horizontal direction [14]. They are also referred to as horizontally polarised shear (SH) waves. An illustration of this wave is shown in Figure 2-6.

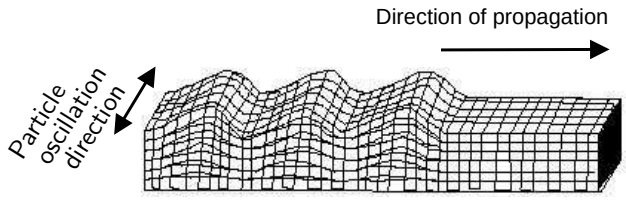

Figure 2.6: Love waves propagating in a semi-infinite medium

Application of this kind of wave is most common in the field of seismology where horizontal shifting of the earth can be observed during earthquakes.

2.2.4 Finite Medium

A medium bounded by two surfaces can couple surface waves on its boundaries to produce more complex propagation modes called Lamb waves [2;8]. These

waves fundamentally occur in the symmetric (extensional or S_0) and asymmetric (flexural or A_0) wave modes as illustrated in Figure 2-7. However in theory an infinite number of higher order modes can also exist in the medium.

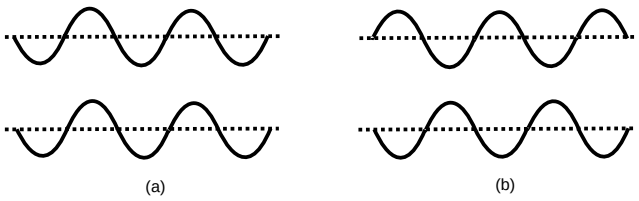

Figure 2.7: (a) Symmetric (extensional) (b) Anti-symmetric (flexural) wave modes

Application for this kind of waves can be found in the field of Non-destructive Testing (NDT) where techniques such as Acoustic Emission and Guided Ultrasonic testing are being developed for a variety of applications.

2.3 Properties of Guided Waves

2.3.1 Dispersion

Waves generated in plate structures travel at velocities which are dependent on material properties as well the thickness of material. A wave packet travelling in a structure can have a different velocity from the individual waves in the packet [15]. The velocities of the individual waves are termed *phase velocity* and that of the wave packet called *group velocity*. For an isotropic and homogeneous plate the extensional and flexural wave group velocities are given by the following expressions [16-18].

$$C(\omega)_e = \sqrt{\frac{E}{\rho(1-\nu)}} \tag{2.4}$$

$$C(\omega)_f = \left[\frac{Eh^2}{12\rho(1-\nu)}\omega^2\right]^{\frac{1}{4}} \tag{2.5}$$

Where,

$C(\omega)_e$ - *Extensional mode*

$C(\omega)_f$ - *Flexural mode*

E - *Young's modulus*

h - *Thickness*

ρ - *Density*

ν - *Poisson's ratio*

Dispersion curves can be generated for a variety of structures and materials which show the relationship between velocity and the product of frequency and thickness.

2.3.2 Attenuation

The amplitude of guided waves as they travel through a medium can be expected to decrease with increased distance of propagation. One factor contributing to this process is due to geometric spreading of the wave-front [6]. This is because waves generated from a localised source travels in all directions away from the source and the wave's finite energy is distributed over a much wider area with increased distance travelled and the amplitude of wave-front is decreased as a result.

Attenuation of guided waves can also occur due to a variety of energy loss mechanisms such as conversion from mechanical to thermal energy due to internal friction. Another source of attenuation could be attributed to dispersion.

Waves propagating in media containing complex boundaries and discontinuities would cause interactions at these features by way of scattering and diffraction which can also lead to a decrease in resulting amplitude wave. Attenuation due to both phenomena is difficult to characterise and has led to more empirical approaches to account for this kind of attenuation [6].

2.4 Damage monitoring using Acoustic Emission

The acoustic emission technique is used as a passive method for damage sensing by monitoring AE signals generated from a damage site using sensors bonded to the structure subjected to load. Advances in hardware and software have spurred AE research along three major themes; damage detection [19-21], location [22-28] and characterization [29-36].

2.4.1 Damage detection

The AE signals are sensed by transduction of dynamic local material displacement, caused by stress wave motion, to electrical signals which are measured at particular sampling rates. Different types of sensors have been developed based on different transduction methods. Commercially available AE sensors include non-contact optical sensing which measures surface displacement based on the Doppler Effect of an incident light beam [19; 37], fibre optic sensing based on Fibre Bragg Grating (FBG) techniques [20; 38; 39] and piezoelectric sensing which generates electric signals as a result of mechanical strain on piezoelectric elements [21]. Other sensing methods include capacitive [40] and Micro Electro-Mechanical Systems (MEMS) transducers [41]. Piezoelectric sensors appear to be most commonly used although the difference in performance compared with other sensor types is not clear. Initial research efforts in damage detection using AE started in the 1950s and 1960s [42; 43] however the development process has stuttered along with parallel advances in electronics and computing with present commercial systems able to operate across the entire AE frequency spectrum, with sampling rates up to 20 MS/s [44]. This technique has evolved over time and found applications in monitoring civil, aerospace, pressure vessels and pipeline structures [45; 46].

Acoustic emission testing is applied in Non Destructive Evaluation (NDE) of structures by subjecting them to static loads and monitoring the AE signals generated [42]. Examples of successful applications include detecting and locating active discontinuities in pressure vessels and monitoring resistance of welds during welding or cooling [47]. As a result the American Society for Testing Materials (ASTM) has developed standards for performing various tests using acoustic emission monitoring [48; 49].

Two major principles have been derived from such applications of AE testing as illustrated in Figure 2-8 which shows a schematic plot of cumulative AE against applied static load. The Kaiser Effect can occur when a particular level of load is applied to an object and then removed; additional acoustic emissions cease to occur until the previous maximum load is exceeded [47]. This can be seen between points B-C-B in Figure 2.8. The Felicity Effect is an exception to the Kaiser Effect which occurs in composite materials. It is observed when acoustic emissions re-emerge, after unloading and reloading of an object, even before the previous maximum stress is attained [47]. This can be observed between

points D-E-F, as illustrated in Figure 2.8, and is characterised by the Felicity Ratio which is the ratio of the stress where the acoustic emissions re-emerged to the previous maximum stress.

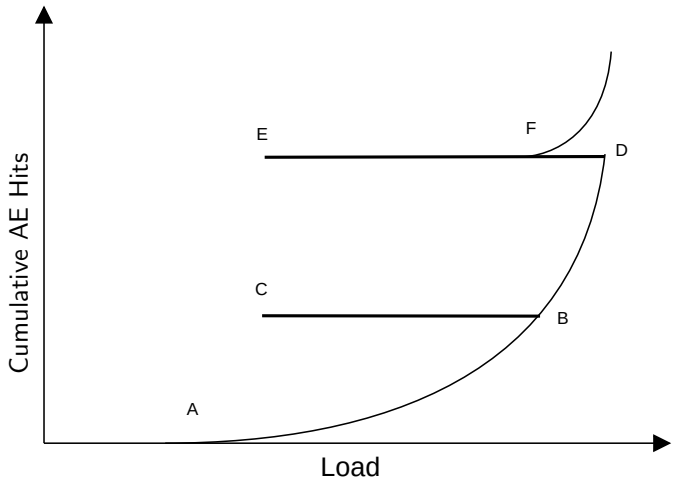

Figure 2.8: Cumulative AE history with applied load showing the Kaiser effect (B-C-B) and felicity effect (D-E-F)

AE monitoring has also been applied to test components and structures under dynamic loading as a means for damage detection [50-52]. This capability has often been demonstrated on simple test specimens with much fewer studies performed on realistic aircraft structures. Notable examples include Holford et al. (2009) [53] and Atherton et al. (2005) [54] where damage monitoring using AE was performed on a landing gear and wing structures respectively.

Other characteristic principles of AE have been demonstrated under dynamic loading, most notably in the area fatigue crack prognosis. Morton et al. (1973) showed a correlation between AE count rates per loading cycle ($d\eta/dN$) recorded within 10% of the peak load, and stress intensity factor range as expressed in Equation 2.6. In conjunction with the well established correlation between fatigue crack growth rates *(da/dN)* and stress intensity factor range Δk [30], the potential of the AE technique has been shown in predicting remaining useful fatigue life of a test component based on short term AE monitoring [31; 55-57]. Yu et al. (2011) showed that AE signal energy rates per cycle *de/dN* gave more accurate fatigue life prediction results than AE count rates per loading cycle *(dc/dN)*.

$$\frac{d\eta}{dN} = B(\Delta k)^p \tag{2.6}$$

Where,

Δk - *Stress intensity factor range*

η - *Counts i.e. number of time the AE signal amplitude exceeds a particular threshold*

N - *Number of fatigue load cycles*

B,p - *Material constants* [31;56]

Acoustic Emission event sources can be located using a variety of techniques based on measurements of the time difference of arrival (TDOA) of the AE signals at different sensors in an array. The start of the signal is usually detected by means of first threshold crossing (FTC), where the amplitude of the transient signal exceeds a predetermined threshold. A threshold-independent method called the Akaike Information Criterion (AIC) was developed by Kurz et al. (2005) [58] for detecting the onset of a signal. This was performed by dividing the signal into two parts at a point t and the variance of the sections is calculated as expressed in Equation 2.7 which represents their similarity in entropy [58]. Minimum *AIC(t)* is expected at the onset of a signal.

$$AIC(t) = tlog_{10}(var(x[1;t])) + (T - t - 1)log_{10}(var(x[t;T])) \tag{2.7}$$

Where,

var(x) - *Variance*

t - *Point of partition*

The most basic application is in zonal location of an AE event, where its location is associated with the vicinity of a particular sensor when AE signals are detected at that sensor before others in the same array [47;59]. The results obtained with this approach are however ambiguous as they only indicate a possible direction of the source and not a particular location.

Tobias et al. (1976) [60] developed a generic method for determining AE source location using TDOA measurements and demonstrated 2D location using an

array of three sensors. This approach can be used to determine the 1D, 2D and 3D locations of an AE event using a distributed array of AE sensors.

Two sensors are typically used for 1D location of an AE event as illustrated in Figure 2-9 and this can be calculated using the expression in Equation 2.8. However, Baxter et al. (2007) [27] demonstrated 1D location of AE events with only one sensor using the single sensor modal analysis location (SSMAL) method, where the time delay between the fundamental wave modes (S_0 and A_0) was used to calculated the distance of the AE source from the sensor, given a known wave velocity. This technique is most effective in applications where the AE signals generated propagate over long distances and the differences in wave velocities of the wave modes create even greater time delays which make them more distinguishable.

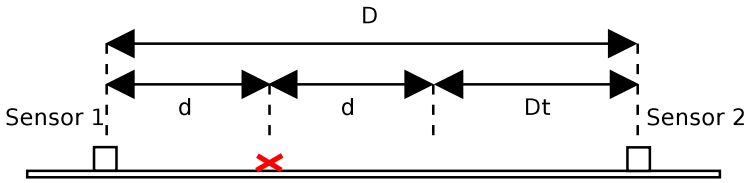

Figure 2.9: 1D AE source location using an array of two sensors

$$d = \frac{1}{2}(D - \Delta t V) \tag{2.8}$$

Where,

V - *Wave velocity*

The 2D and 3D locations of AE events require a minimum of 3 and 4 AE sensors respectively [61]. These could be determined by solving a set of non-linear equations shown in Equations 2-9, 2-10 and 2-11. [22]. Figure 2-10 illustrates an example of 2D location using TDOA measurements from a 4-sensor array.

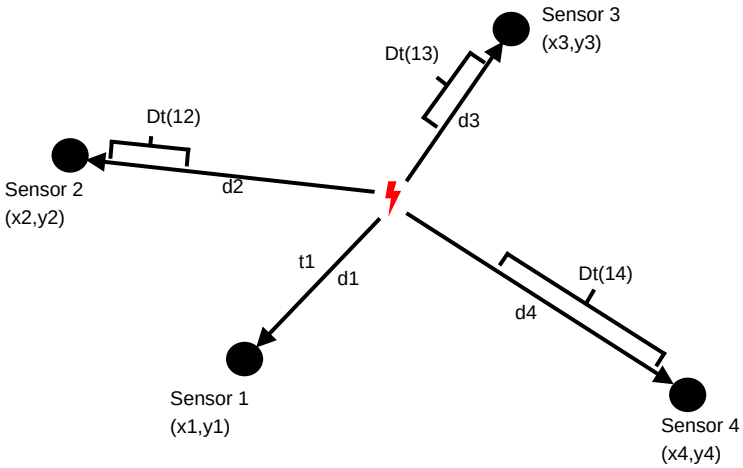

Figure 2.10: 2D AE source location using an array of four sensorss

$$d_i = \sqrt{(x_i - x_o)^2 + (y_i - y_o)^2} \tag{2.9}$$

$$t_j = t_1 \pm \Delta_{1,j} (j = 2, 3, 4) \tag{2.10}$$

$$t_i = t\frac{d_i}{V} (i = 1, ..., k) \tag{2.11}$$

Where,

V - *Wave velocity*

x_i, y_i - *Sensor locations*

x_o, y_o - *AE event location*

k - *Number of sensors*

The AE technique is typically applied to determine 2D location of AE events occurring in the area within a sensor array. However, Aljets et al. (2012) [59] developed a technique for performing 2D location on large plate structures using closely positioned sensors in a triangular array with extended coverage. This involves firstly performing zonal location to determine the direction of an AE source and then the distance is evaluated using time delay measurements between the fundamental wave modes at each sensor respectively. This method was demonstrated on a 1300 x 900 mm x 2.5 mm carbon fibre epoxy plate however the accuracy of location estimates was not reported.

There are two main challenges in performing AE source location which relate to the accuracy in obtaining timing measurements and estimation of propagating wave velocity. Baxter et al. (2007) [27] developed the "Delta T" method for AE source location in anisotropic structures which are known to have non-uniform wave velocities. This was done by creating AE events from an artificial source and recording the TDOA values at distributed locations. A look-up map was constructed from the TDOA values between various pairs of sensors and was used as a reference for actual AE events occurring in the component. Application of this technique showed an error of 1.77% compared to 4.81% obtained using the conventional location method.

Ciampa et al (2010) [22] developed a frequency-time based method for measuring TDOA values using the squared modulus of the Continuous Wavelet Transform (CWT) to obtain the highest local energy content of waveforms recorded at each transducer. Correlating these points in the time domain corresponds to the time of arrival of each wave from which TDOA values can be calculated. Application of this method in locating AE events in a quasi-isotropic Carbon Fibre Reinforced Plastic (CFRP) panel and a sandwich plate showed maximum errors of less than 2% and 1% respectively.

2.4.2 Acoustic Emission characterisation

Acoustic emission signals can be characterised by various features extracted from the signals. A schematic of a typical AE signal is illustrated in Figure 2-11, showing basic features of signal duration and amplitude. Additional features of the signals can be extracted in the frequency domain as well as others derived from combinations of existing features as a function of the source mechanism responsible for generating the respective AE signals. However, considerable variability in the magnitude of these features can be expected even in signals from similar sources which create a challenge in uniquely identifying AE signals.

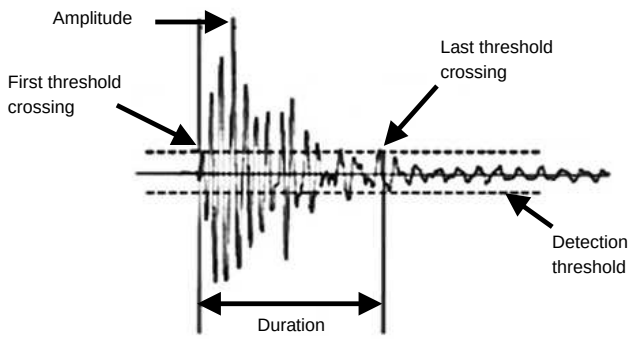

Figure 2.11: Acoustic emission signals with basic features of amplitude and duration

Application of the AE technique in realistic structures has a significant challenge in discriminating between genuine AE signals relating to an existing damage from other AE signals relating to benign mechanisms such as sliding at a joint of an assembled structure subject to load for example. Procedures have been developed to filter out noise from genuine AE signals based on their features. Fowler et al. (1989)[132] developed the Swansong filter which identifies groups of AE signals using combinations of their amplitude and duration predefined in specific ranges [56]. This method employs subjective values to configure the filter bounds depending on the application which may not be robust given the variability in these AE signal features.

With as many as 14 features derived from each AE signal, visualising geometric the properties of these features relating to each other which potentially demarcate AE signals from different sources are not easily comprehensible due to limited human cognition in a high multi-dimensional space. Advance data processing methods have been applied to AE data to optimise discrimination of AE signals recorded from different sources. Common methods adopted are Principal Component Analysis (PCA) which is used to perform multi-dimensional feature reduction [62], k-means for clustering [63; 64] and Kernel Density Estimation for visualising clusters [65].

Principal Component Analysis (PCA)

This is a mathematical procedure used to transform a multi-dimensional data set into latent variables of reduced dimension with the greatest variance of the original data set represented in the first latent variable, the second greatest variance represented in the second latent variable, and so on. Each latent

variable, also known as Principal Component, is a linear combination of the original data variables but computed orthogonal to each other. Details of the PCA method can be found in Nabney (2004) [62]. It is performed in the following steps:

- Calculate the mean of each variable in the data set and then subtract each observation from the means of their respective variables. This will adjust the data set to be centred on its mean.
- Determine the covariance matrix of the resulting data in step i.
- Determine eigenvectors and eigenvalues of the covariance matrix
- Derive latent data set

Each principal component represents a portion of the overall variance of the original data set which tends to decrease with increased number of principal components. A trade off needs to be made between the number of reduced latent variables (principal components) required and the percentage variance sufficient for analysis.

PCA has been applied to AE data to aid discrimination when AE signals are detected from different sources. Pullin et al. (2008) [66] applied PCA to AE data generated from several artificial sources in complex landing gear components of an aircraft and a clear distinction was observed between each of them. Analysis of data recorded on one sensor was recommended due to differences in sensor response and propagation path which can affect the features of the signals.

K-Means clustering

This method is used to partition a data set into k clusters with each observation located in a cluster with the nearest mean. It is a very mature technique and widely used across several fields; details can be found in Nabney (2004) [64]. Clustering is performed by first of all assigning initial values of mean of the k number of clusters and then the algorithm is implemented iteratively in two steps until the solution converges [64]:

- Assign each observation to the cluster with the nearest mean
- Calculate the new means for each of the k clusters which will become their new centroid.

Anastassopoulos et el. (2000) [67] developed an algorithm for unsupervised classification of AE signals from different sources. This involved performing feature reduction using PCA and clustering using the k-means method. The number of target clusters used in this procedure was estimated using the and criteria [67; 68]. The resulting partitions of the data are used to train a neural network for classification of subsequently recorded data. This algorithm has been reported to successfully classify AE signals from a variety of mechanisms which includes coating fracture, delamination and fatigue crack [68; 69].

Kernel Density Estimation (KDE)

This is a non-parametric method for estimating the probability density function of a random variable, which enables visualisation of the underlying probability distribution. Details of this technique can be found in Botev et al. (2010) [65]. It can be applied to both univariate and multivariate data sets in two steps:

- Assign a kernel function to each observation in the data set
- Sum all the kernels to obtain the density function

Holford et al. (2009 [53]) applied this method to AE data obtained from a fatigue test performed on an aircraft landing gear component. This was used to visualise the distribution of the 2D location estimates.

2.5 Fatigue cracks in metallic structures

Stress concentrations occur around geometric discontinuities in structures, for example notches, as they are subjected to tensile loading. This can result in local maximum stresses which exceed its elastic limit and will result in areas of permanent plastic deformation also known as plastic zones, with its size and shape expected to change with increased crack length and applied load [70]. Engineered metallic structures, like aircraft for example, contain a vast amount of such stress concentrations.

Fatigue is the process whereby if a component is subjected to repeated alternating stress, even though less than the values required to cause failure from a single load application, cracks can develop and grow to a critical length where spontaneous and catastrophic failure occurs [71]. Fatigue tests are conducted on specimens of different materials to characterise their fatigue performance

under constant amplitude loading [72; 73]. The data can be represented as plots of applied stress range versus number of cycles to cause failure, which can range from less than 10 cycles to over 10^8 cycles. The amplitude of the load cycles has a significant effect on fatigue performance and is characterised by the ratio of the minimum stress to maximum stress which is also termed the Stress ratio (R).

There are two main stages of fatigue life which are known as *Crack Initiation* and *Crack Growth* [74]. The scope of this thesis is focused on the crack growth phase. A schematic of a typical plot of crack growth with applied load cycles is illustrated in Figure 2-12 where an exponential relationship can be seen, which shows that the majority of crack growth occurs in the final few percent of fatigue life.

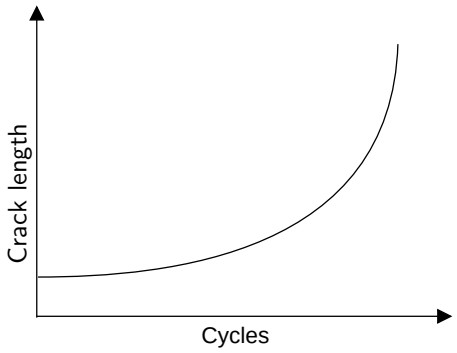

Figure 2.12: Crack growth versus applied load cycles

The principles governing crack growth are well understood in the field of fracture mechanics and extensive details are covered in available literature [70]. Figure 2-13 illustrates a schematic of a crack in an infinite plate under tensile load with denotations of stress tensors. The general solution of the resulting linear elastic stress field is given by Equations 2.12 and 2.13 [70]. The constant K and β are dependent on general solution of the resulting linear elastic stress field is given by the geometry of the specific problem. The magnitude of stress at any point around the crack tip is directly proportional to the K constant which is known as the stress intensity factor.

$$\sigma_{ij} = \frac{K}{\sqrt{2\pi r}} f(\theta) \tag{2.12}$$

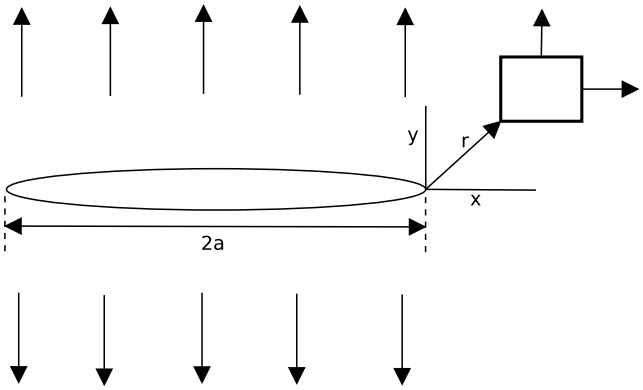

Figure 2.13: Crack in an infinite plate

$$K = \sigma\sqrt{\pi a}\beta \tag{2.13}$$

Where,

a - *Crack length*

σ - *Stress*

Fracture of a specimen will occur when k reaches a critical value denoted by $K_{I\ C}$. This is used as a measure for the crack resistance of a Fracture of a specimen will occur when K reaches a critical value material. Fatigue crack growth prior to the point of failure can be characterised using Paris Law, shown in Equation 2.14 [74], which correlates the crack tip stress intensity range to the crack growth rates. The stress intensity range (ΔK) can be calculated by substituting stress range ($\Delta\sigma$) for bulk stress (σ) in Equation 2.10 [74; 75].

$$\frac{da}{dN} = C\Delta K^m \tag{2.14}$$

Where,

a - *Crack length*

N - *Number of fatigue cycles*

k - *Stress intensity factor*

A schematic of a typical fatigue crack growth rates curve is shown in Figure 2-14. The three stages known to occur are indicated as well as the effect of increasing R ratio. Stage I is also known as the short crack propagation stage

where crack growth is along the high shear stress plane, 45 degrees to the applied load, and dependent on the microstructure of the material [74]. In Stage II crack growth follows stress intensity factor reaches a critical value (k_{IC}) where crack growth Paris Law with increased stress intensity factor and in Stage III the accelerates and catastrophic failure will occur. As illustrated in Figure 2-14, increasing R ratio will result in increased crack growth rates in all regions of the curve. This effect is most significant in Stages I and III [74; 76].

Fatigue crack are also known to start off in a plane perpendicular to the direction of loading, however after some time it start rotating around the direction of propagation until it attains an angle of 45^0 [77], as illustrated in Figure 2-15. This occurs as a result of a change in the stress state at the crack tip from triaxial, also referred to as plane strain, to biaxial or plane stress [78; 79].

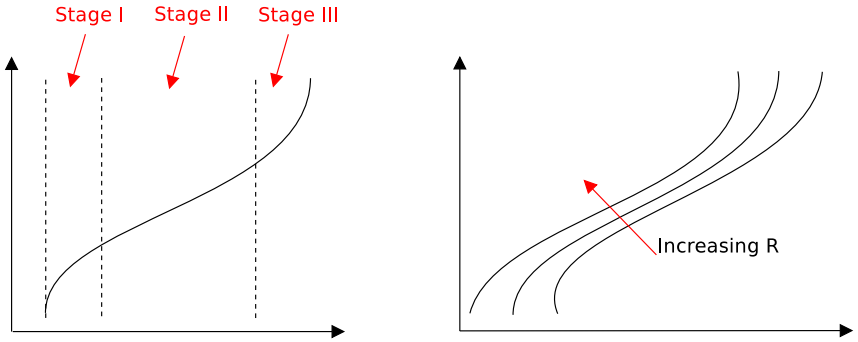

Figure 2.14: Schematic of a typical fatigue crack growth curve

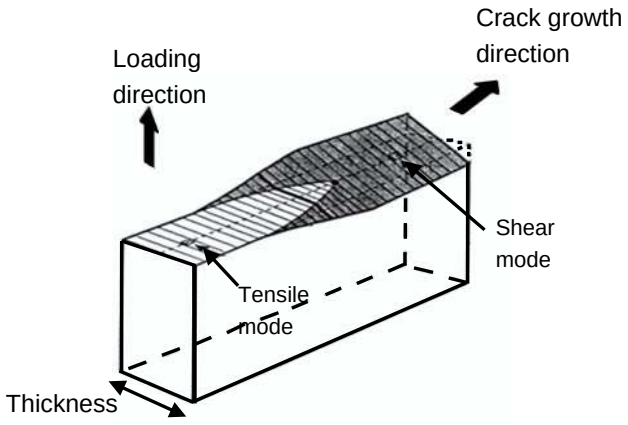

Figure 2.15: Crack rotation from tensile to shear mode

Crack closure behaviour, where the crack faces contact each other, can be expected even in global tension stress fields during fatigue crack propagation [75].

This phenomenon can be attributed to plastic zone formation in a specimen under fatigue loading, where compressive residual stresses are experienced in this region and causes reduced crack opening than would be expected in the case of static loading. With increased number of applied load cycles the crack would grow through this region of plasticity, leaving in its wake plastically deformed material which can cause the crack surfaces to come in contact with each other [75]. Figure 2-16 illustrates a schematic of a load cycle with indications of stress intensity parameters. The difference between $K_{opening}$ and K_{min} indicates the indicates the period in the load cycles where the crack is closed. The extent of crack closure is represented as the ratio of $K_{opening}$ or $K_{closing}$ to K_{max}. Which will be equal to the nominal stress ratio (R) when crack closure does not occur.

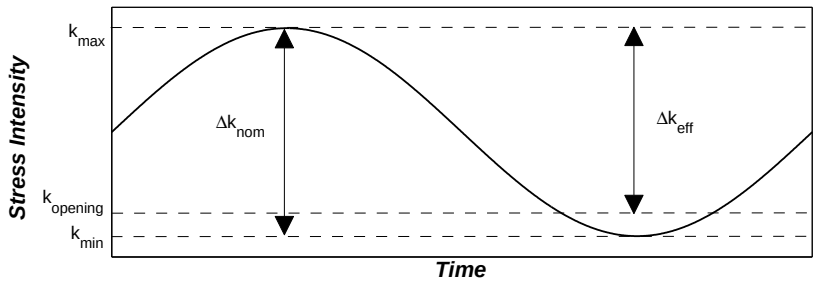

Figure 2.16: Crack closure occurring in load cycle

The vast majority of fatigue tests are conducted using constant amplitude loading [80]; however in real applications, loads of varying amplitudes are experienced. Standardised spectra for different applications include TWIST which is representative of the load history of the wing root of a transport aircraft and FALSTAFF which is representative of the load history of the wing root of a fighter aircraft. Figure 2-17 [81] illustrates some load sequences of a standardised FALSTAFF load spectrum which is characterised by low amplitude cycles, including a few of them entering compression, with intermittent excursions to greater loads.

Under such variable amplitude loading conditions crack closure behaviour can also be expected, due to large zones of reversed plasticity created as a result of application and removal of large load excursions, which also causes crack retardation [72].

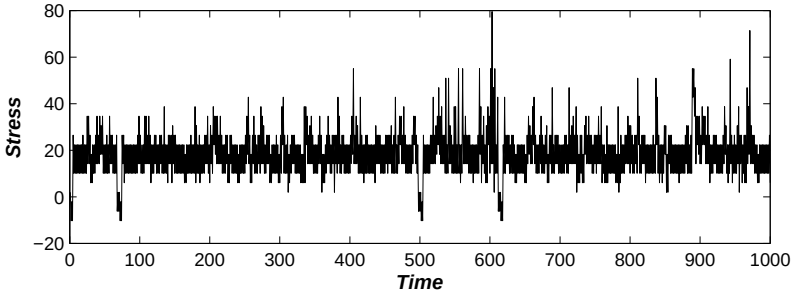

Figure 2.17: FALSTAFF variable amplitude loading spectrum

2.6 Acoustic Emission generation from cracks

Acoustic Emission (AE) signals generated during fatigue crack growth in metallic structures are monitored to detect the presence of damage and the sources of these signals are classified as either primary or secondary [2; 82]. Primary AE sources are generally associated with fracture mechanisms occurring around the crack tip which includes crack extension [33; 83; 84] and deformation of plastic zone around the crack tip which results to local failure of second phase particles [3; 33;85]. Secondary AE sources on the other hand are related to crack closure processes which results in fretting of crack surfaces [2; 69; 84].

Scruby et al [84] conducted a study to characterise AE generated from crack extension during fatigue crack growth in 7010 aluminium alloy. It was concluded that crack extension is not the dominant source of AE from fatigue crack growth since ductile tearing of the material occurs in every loading cycle and the rate of recorded AE was much lower, an average of about 1 AE signal in 20 cycles.

Morton et al. (1973) showed that the correlation between AE count rate per loading cycle $d\eta$/dN for AE signals recorded with 10% of the peak load, and stress intensity range (ΔK) was better than the correlation between AE count rate $d\eta$/dN and crack growth rate da/dN. This suggests that the AE signals observed were more closely related to the crack tip plastic volume [30].

Several studies have been conducted to investigate sources of AE during plastic deformation in aluminium alloys [3; 51; 83; 85; 86]. McBride et al (1981). [3] and Lugo et al. (2011) [51] similarly presented results that showed generation of AE from fatigue crack to be dependent on the existence and size of inclusions in aluminium alloys. McBride et al. (1981) [3] observed the influence of material

strength on the fracture of inclusions and the consequent generation of AE and a strong correlation was made between the number of fractured inclusion and the number of AE signals recorded.

Fretting of crack surfaces may also be expected during fatigue crack growth which could be dependent on crack closure. AE signals generated from this source are generally considered to be of the continuous type [3; 46; 57]. Moorthy et al. (1994) [33] noted that AE signals can be generated from plasticity-induced closure, which is more prominent in plane stress, as well as asperity or roughness-induced closure, which results from a mismatch between crack surfaces as a function of the coarse microstructure of a material. Quantitative studies on the contribution of these processes were not uncovered in preparation of this thesis.

Daniel et al.[87] and Han et al.[52] conducted investigations on trends exhibited by AE signals generated during fatigue crack growth in aluminium and welded steel samples respectively. Both studies presented results indicating 3 stages in accumulated AE signals over a period of applied cyclic load. Daniel et al. showed that Stage 1 was characterised by a rapid increase in number of AE signals generated at the start of crack growth, which lasted for about 15% of the sample's fatigue life, and then significantly fewer AE signals were observed in Stage 2 which lasted for about 65% of its fatigue life. Stage 3 occupied the final 20% of its fatigue life, where an increase in AE signals was observed.

2.7 Damage inspection of aircraft

Fatigue damage invariably occurs in aircraft structures and maintenance is triggered by inspections using Non Destructive Testing (NDT) techniques to manually check for damage at fixed service intervals. The reliability of the inspection process is assessed by the performance of the NDT techniques as well as their operators using Probability of Detection (POD) curves. This is defined as the probability of detecting damage, fatigue crack for example, in a given size group under inspection conditions and procedures specified [88]. It can be derived using either the Binary (hit/miss) or the signal response methods [89]. The hit/miss POD method considers binary indications of the presence or absence of damage at various levels of severity and binomial regression is applied to derive a probabilistic relationship. The signal response method on the other hand correlates signal response measurements with various levels of

damage and a probabilistic relation is derived using linear regression techniques [89].

The POD curves generated are typically monotonically increasing with increase in crack length and confidence intervals are also determined [90]. The performance of NDT techniques is judged by the crack length ($a_{90/95}$) which gives a 90% POD and 95% lower confidence, denoted by ($a_{90/95}$). A schematic of POD curves derived using these methods are shown in Figure 2-18 with indication of a90/95.

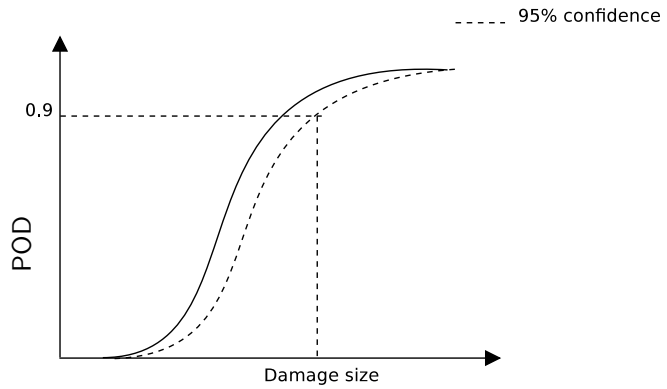

Figure 2.18: Schematic of a typical POD curve with lower confidence bound

Although scheduled maintenance is successfully applied based on manual inspections using NDT techniques; however there are some significant disadvantages which include the following:

- Cost and effort to disassemble complex structures to gain access to restricted areas
- Risk of inflicting damage in the process
- Cost of aircraft down-time when damage is not found.
- Errors due to variation in competence of operators

2.8 End-to-end variability in AE monitoring

The AE monitoring process begins with the AE signals being generated from a damage mode of interest and ends with the information obtained from the processed signal. Intermediate steps include mainly propagation through a medium and then detection by a sensor. The performance of the technique in damage detection and location is influenced by complex transfer functions

between the source and processed signal [45]. These can be grouped as AE signal generation [53], propagation medium [27], signal-sensor coupling [91; 92] and data processing [45], as illustrated in Figure 2-19.

AE signal generation from fatigue cracks can be produced as a result of processes such as fracture of inclusions, crack closure or crack extension occurring during fatigue crack propagation [47]. Depending on material properties, physical geometry and loading configurations, the prevalence of AE from these sources may be affected. Also, the integrity of sensor coupling with the structure can also compromise AE detection [92].

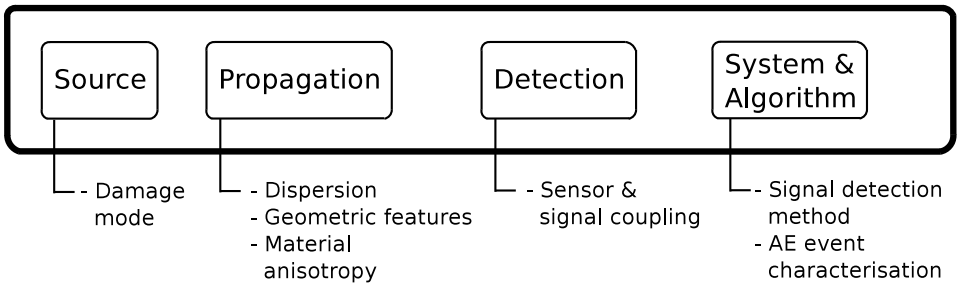

Figure 2.19: Sources of variability in the output of the AE system

Material properties and component geometry can affect the dispersion properties of AE signals from which the wave velocity is derived and used as an input in triangulation algorithms for determining AE event location estimates. Wave velocity calibration methods have been developed for improving the performance of this technique in anisotropic test samples, as well as those containing geometric features [27].

A survey of SHM techniques including AE was conducted and presented in Appendix A. It was interesting to find that there was a general lack of quantitative information on the performance of the various techniques with a lopsided emphasis on damage sensitivity. There were very few examples where the reliability and confidence of techniques were demonstrated.

Scholey et al. (2009) applied a predictive modelling approach to quantifying the performance of AE systems on plate-like structures. This involved simulation of a source waveform at many different locations relative to the AE sensors, taking into account known attenuation characteristics of the medium. Performance was evaluated by areas of AE signal generation where they were successfully detected at the sensors as well as location error. This study however did not take into account the variability associated with AE generation from a

particular source like fatigue crack for example.

Pullin et al. (2007) explored the Confidence of Detection (COD) of AE testing by means of examining clusters of location estimates from detected signals over a specific area. This involved creating a COD matrix consisting of cluster size and cluster threshold, number of AE events required to form a cluster, which is interpreted as 'high' COD where the predetermined cluster threshold is exceeded for smaller cluster sizes. This methodology is heavily dependent on the accuracy of the AE events location estimates which was not characterised. Pullin et al. (2007) and Scholey et al. (2009) were the only studies uncovered in the preparation of this thesis addressing the performance of fatigue crack detection using AE. Apparently, there are also currently no performance metrics available, akin to the POD curves utilised in NDT, to quantify and qualify changes in performance levels.

2.9 Concluding Remarks

There is a general lack of quantitative information on the performance of the SHM techniques and as a result, there is no current means of verifying their level of performance in specific installations. This will require development of measures to quantify and qualify its performance as well as building further understanding effects of the potential influencing factors. Also, given the sources of variability in the AE monitoring process, its level of performance can be expected to diminish with increased complexity in the subject structures. Validation of the AE technique in realistic structures needs to be performed to further understand its capabilities and challenges in such environments.

Chapter 3

Methodology

3.1 Introduction

Experiments were performed to characterise Acoustic Emission (AE) generation from fatigue crack in coupon test samples. This required sample preparation, fatigue testing, crack length measurement as well as AE monitoring. Details of how these steps were accomplished and also the configurations of the various tests conducted are given in this chapter. Also, experiments were conducted in collaboration with the National Research Council of Canada to validate the performance of the AE technique in 'blindly' detecting and locating fatigue crack damage in a representative wing-box structure. Details of the test setup are also provided in this chapter.

3.2 Coupon test samples

The material used in this study is 2 mm 2014 T6 aluminium alloy. This is a high strength aluminium alloy used in Military aircraft wings. The specified chemical composition is shown in Table 3 1 which shows that the different batches of the material used in this study were verified to be within specification.

Table 3.1: Chemical composition specification for 2014 T6 aluminium

	Si	Fe	Cu	Mn	Mg	Cr	Zn	Ti	V	Zr
Min	0.50	0.00	3.90	0.40	0.20	0.00	0.00	0.00	0.00	0.00
Max	0.90	0.50	5.00	1.20	0.80	0.10	0.25	0.15	0.05	0.05
Batch 1	0.82	0.18	4.40	0.71	0.59	0.05	0.04	0.01	0.01	0.00
Batch 2	0.74	0.17	4.30	0.59	0.62	0.01	0.20	0.02	0.00	0.01
Batch 3	0.79	0.19	4.50	0.66	0.59	0.00	0.06	0.01	0.01	0.00

Tensile tests were also performed according to the American Society for Testing and Materials (ASTM), designated E8/E8M – 09, to determine the mechanical properties of the different batches of the material. The results for Yield and

Ultimate Tensile Strength (MPa) are given in Table 3 2 and also illustrated in Appendix B. This shows repeatability between samples from the same batch of material but a slight difference across the batches, although this is only considered marginal.

Table 3.2: Mechanical properties of samples from three batches of 2014 T6 aluminium material

	Batch 1		Batch 2		Batch 3	
Sample	Yield (MPa)	UTS (MPa)	Yield (MPa)	UTS (MPa)	Yield (MPa)	UTS (MPa)
1	435	495	442	491	440	491
2	435	495	442	491	440	491
3	435	495	442	491	440	491
4	435	495	442	491	440	491

A total of 18 test samples were made and tested from three batches of this material. All test samples were of identical dimensions; 530 mm long, 250 mm wide and 2 mm thick with the sample length parallel to the rolling direction of the material. 16 of the test samples were Single Edge Notch (SEN) and 4 were Mid-crack Tension (MT) as illustrated in Figures 3-1 and 3-2 respectively. The edge notch was machined 10 mm deep and made using a 3 mm wide 60 degree cutter, while the centre notch was 18 mm long and 3 mm wide. A further 1 mm extension of the notch was introduced at either end using a jeweller's saw making a total crack length of 20 mm.

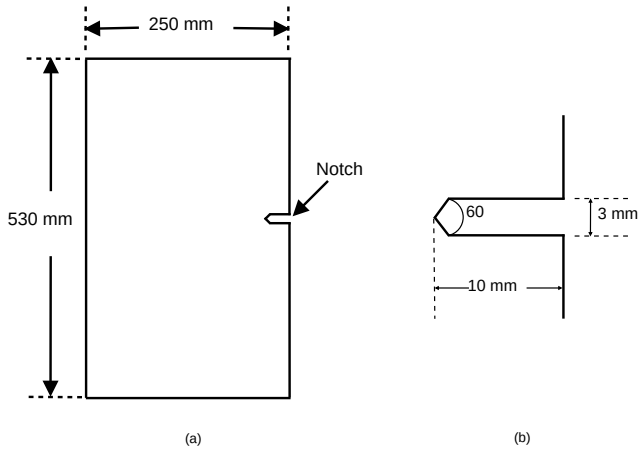

Figure 3.1: (a) Single edge notch test sample (b) Notch dimensions

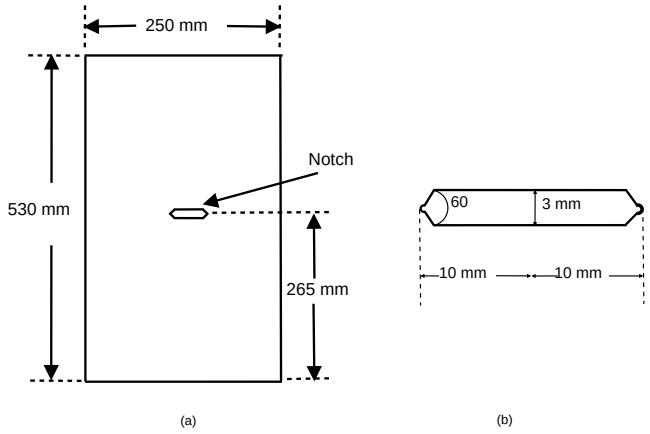

Figure 3.2: (a) Single edge notch test sample (b) Notch dimensions

The major difference between the two scenarios is that in the case of the M(T) samples there is no in-plane bending, where the sample rotates in the plane of the applied load, and consequently smaller displacements of crack opening, compared with the SEN samples where the presence of in-plane bending causes greater displacements when subjected to tensile loads. Also, the M(T) samples would have a crack initiated from either end of the notch; under ideal conditions symmetric crack growth rates can be expected.

3.2.1 Fatigue test machine and set-up

A 30 kN servo-hydraulic fatigue machine was used to perform all tests. This could be configured to apply constant amplitude loads to test specimens as well as being remotely controlled via a General Purpose Interface Bus (GPIB) port, where variable amplitude load settings can be used. There is also a $\pm 10V$ analogue output channel from which the applied loads can be monitored.

The top and bottom of the test samples were gripped using friction jaws which were manually fastened using bolts. The test machine grips were 200 mm wide which meant that the samples exceeded its width by approximately 25 mm on either side.

Before each fatigue test the samples were prepared to enable crack length measurement at various stages during fatigue crack development. This process involved polishing the sample surface along the anticipated crack path to make the crack more visible. This was done by applying horizontal strokes along the sample's surface using sand paper over several steps with decreasing grit size. Afterwards measurement inscriptions at 1 mm intervals were made using a

Vernier Calliper with an accuracy of approximately 0.2 mm.

A digital video system was used to monitor fatigue crack development during all of the fatigue tests conducted. A LabVIEW software was used to enable and control image acquisition. Images were captured at a rate of one frame every 20 seconds at the early stages of crack propagation where the growth rates were low and then gradually increased up to one frame every 2 seconds as the samples approached failure where the crack growth rates were relatively fast.

Each picture recorded also included appended information of time and the number of cycles elapsed. The software maintained cycle counts using the computer clock. Synchronisation between the software and the test machine was achieved by simultaneous activation at the start of the test.

3.3 Test matrix

A total of 17 fatigue tests were performed on test samples under constant amplitude sinusoidal loading as listed in Table 3-3. The variables in the experiment were the crack initiating notch locations, maximum stress, R ratio (minimum stress/maximum stress), frequency, sample material batch and stress range.

Test 17 was performed with a quasi-constant stress intensity range of 12.1MPa$\sqrt{m}$. This was performed by reducing the stress range at a constant stress ratio of 0.1 after every millimetre of crack growth until a total crack length of 69 mm. Figure 3-3 illustrates the stress intensity range values at the various crack lengths.

Another test was conducted with the test sample subjected to variable amplitude loading under identical conditions as outlined in Table 3 4. The FALSTAFF loading spectrum, which is representative of the loads experienced by the wing of a fighter jet, was adapted for these tests. This was generated using the GENESIS 4 Fatigue software with maximum stress specified as 58 MPa.

Table 3.3: Constant amplitude fatigue tests on coupon samples

Sample	Notch	Max. Stress (MPa)	Stress range (MPa)	Frequency (Hz)	Stress Ratio	Batch
1	SEN	58	52.2	2	0.1	1
2	SEN	58	52.2	2	0.1	1
3	SEN	58	52.2	2	0.1	1
4	SEN	58	52.2	2	0.1	2
5	SEN	58	52.2	2	0.1	2
6	SEN	58	52.2	2	0.1	3
7	SEN	58	52.2	2	0.1	3
8	M(T)	58	52.2	2	0.1	3
9	M(T)	58	52.2	2	0.1	3
10	M(T)	58	52.2	4	0.1	3
11	SEN	30	27	2	0.1	2
12	SEN	30	27	4	0.1	2
13	SEN	30	27	4	0.1	3
14	SEN	30	27	4	0.1	3
15	M(T)	30	27	2	0.1	3
16	SEN	58	27	2	0.5	2
17	SEN	Decreasing	Decreasing	2	0.1	2

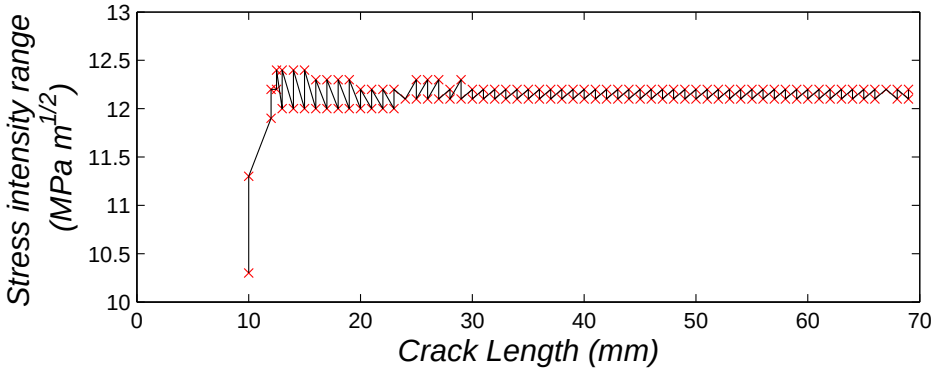

Figure 3.3: Quasi-constant stress intensity range values at the various lengths of crack growth

Table 3.4: Variable amplitude fatigue tests on coupon samples

Sample	Notch	Max. Stress (MPa)	Frequency (Hz)	Batch
18	SEN	58	2	2

Plots of the default FALSTAFF load spectrum and rain-flow count are illustrated in Figures 3-4 and 3-5 respectively. It can be observed that there are

some compressive loads which can be expected to cause buckling in the test samples as their thickness is small compared to it's length. To avoid this occurrence the largest absolute value of compressive load was added to the entire spectrum to ensure every turning point was in tension. Afterwards, the spectrum was normalised to the maximum stress which was translated to the maximum capacity of the fatigue test machine. The result of the formatted spectrum is illustrated in Figure 3 6 and the rain-flow count is also shown in Figure 3 7, where it can be seen the majority of load cycles had a stress range of less than 10 MPa, although the maximum was 55.7 MPa, and stress ratios were predominatly less than 0.7. Furthermore, there were no compressive loads present as can be seen from the absence of negative stress ratios in Figure 3 7.

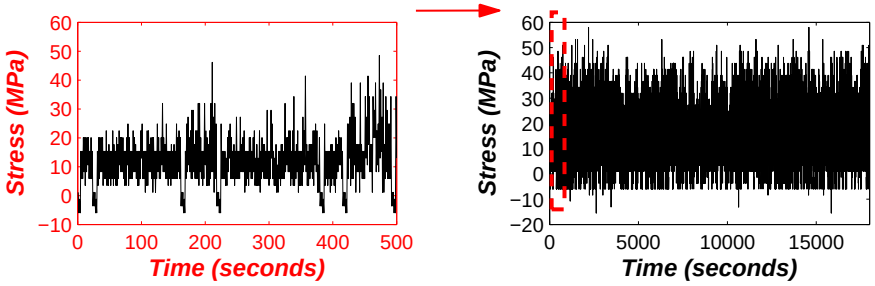

Figure 3.4: FALSTAFF load spectrum with maximum of 58 MPa and minimum stress of -15.4 MPa

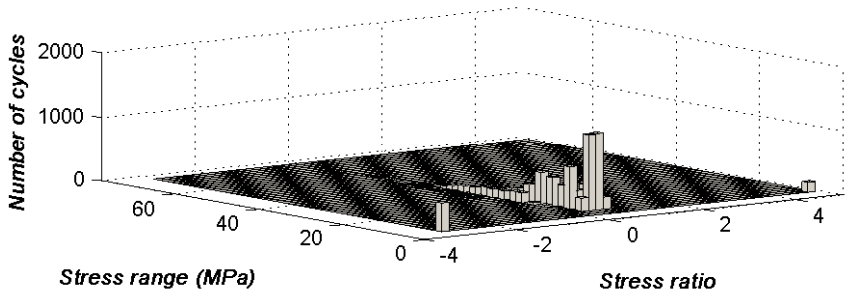

Figure 3.5: Rain-flow count of FALSTAFF load spectrum with maximum stress

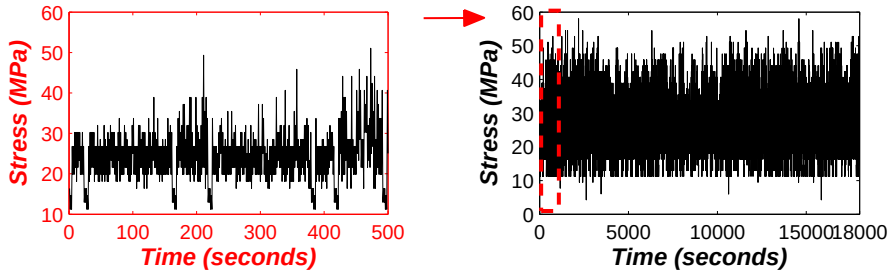

Figure 3.6: Formatted FALSTAFF load spectrum with maximum of 58 MPa and minimum stress of 4.2 MPa

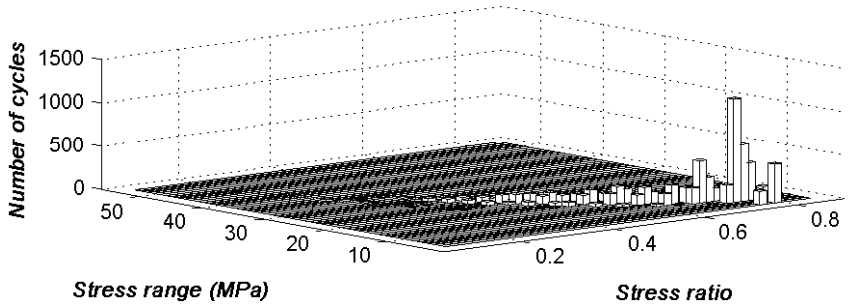

Figure 3.7: Rain-flow count of formatted FALSTAFF load spectrum

3.3.1 Acoustic Emission system

A 6-channel Physical Acoustics AE system was used throughout the experiments for data acquisition and control. This consisted of three 18 bit A/D Peripheral Component Interconnect (PCI) cards with two channels each and having total sampling rates up to 10 MS/s. The system also has eight $\pm 10V$ analogue input channels which enables monitoring of external parameters such as strain, temperature and load alongside normal AE data recording. A block schematic of the AE system setup is illustrated in Figure 3.8.

Broadband piezoelectric sensors with operating frequency between 100 – 1000 kHz and resonant at 125 kHz were used to record AE data which was conditioned, filtered and amplified using a 2/4/6 preamplifier which has selectable gains of 20, 40 and 60 dB. The preamplifier is powered via an output signal from the PC connected via RG-58 50 Ohm coaxial cables. The sensors and preamplifiers are terminated with BNC connectors. Voltage measurements by sensors are represented in decibels given by the expression in Equation 3-1.

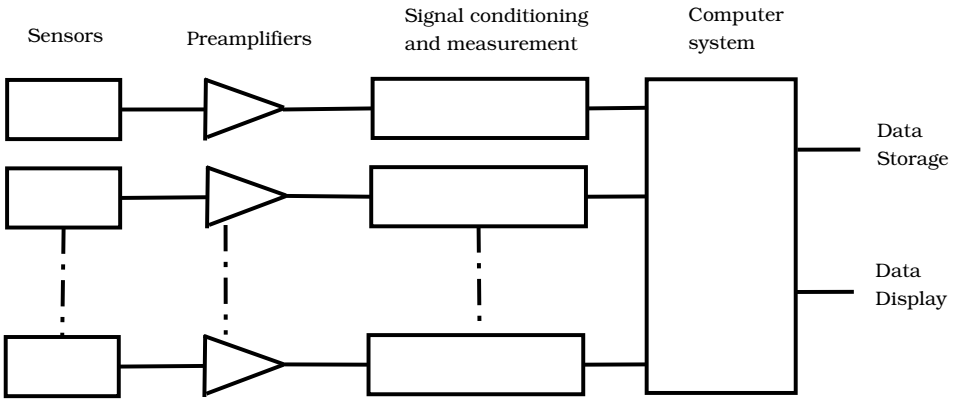

Figure 3.8: Block schematic of the AE system

$$dB_{AE} = 20log(\frac{V_{max}}{1\mu v}) - PA_{gain} \tag{3.1}$$

Where,

PA - *Preamplifier gain*

The AE system is equipped with a built-in sensor test function called the Automatic Sensor Test (AST). This allows the sensors interrogate each other using acousto-ultrasonic pulses, as a means of verifying the integrity of sensor coupling as well as obtaining the arrival time delay between surrounding sensors.

The AE system has accompanying software called AEwin for PCI-2 which was used to control data acquisition as well as performing real-time signal and data processing functions. A number of features are extracted from each AE signal which can be represented in a variety of plots. A total of 14 features were derived from the AE signals and their details are outlined in Table 3 5. Also, 1D and 2D location estimates of AE events can be determined and readily displayed as well as measurements of the AE signals. Data reports of these measurements and location estimates can be generated in text file format by the system.

All the derived features of the AE signals are based on detection of the start, peak and end of the signals. The AE system detects the start of the signals by means of *First Threshold Crossing* (FTC), which is where the signal amplitude first crosses a specified threshold. The peak of the signal is determined by assigning a time window immediately after the FTC, referred to as

Table 3.5: Table 3 5: Derived features from AE signals

Feature	Description	Unit	Resolution
Amplitude	Maximum (negative or positive) signal excursion during an AE Hit	dB	1dB
Risetime	Time between the start and the peak of the AE Hit	dB	$1\mu s$
Duration	Time between the start and the end of the AE Hit	dB	$1\mu s$
Counts	Number of excursions over the detection threshold between the start and end of the AE Hit	dB	1 count
Counts to peak	Numner of excursions over the detection threshold between the start and peak of the AE Hit	dB	1 count
Centroid frequency	Real-time FFT calculations across several segments of the AE signals	dB	1Hz
Peak frequency	Peak magnitude in the power spectrum of an AE Hit	dB	1Hz
Initiation frequency	(Counts to peak / Rise time	dB	1Hz
Reverberation frequency	(Counts - Counts to peak) / (Duration - Rise time)	dB	1Hz
Average frequency	(Counts / Duration)	dB	1Hz
Energy	Integral of the squared signal voltage divided by a reference resistance of the signal duration	dB	9.3 e-4 aJ
Root mean square	Rectified time averaged measurement of AE signals	dB	0.2 mV
Average signal level	Averaged amplitude of the signal	dB	1dB
Signal strength	Integral of the AE signals rectified voltage over its duration	dB	3.05 pVs
PAC energy	(Signal strength / Counts)	dB	1 μVs/count

Peak Detection Time (PDT), where the maximum amplitude of the signal in this period is noted as the peak of the entire signal. However further increments of the same time window are also checked for larger signal amplitudes and where there is no exceeding value in a subsequent time period, the last known peak is considered as the signal peak.

The same approach is used to determine the end of the AE signals where another time window referred to as *Hit Definition Time* (HDT) is assigned immediately after signal peak detection. In this case the *Last Threshold Crossing* (LTC) is noted in the various increments of the time period and is considered the end of the signal when there is no threshold crossing in a subsequent time period. To limit the system from recording AE signal reflections, another time window referred to *Hit Lock-out Time* (HLT) is specified just after the LTC where the system suspends measurements.

3.3.2 Acoustic Emission set-up

The AE system was set-up to monitor AE signals generated from fatigue crack emanating from the root of the crack-initiating notches. The sensors were mounted on the samples using Dow Corning RTV 3140 silicone rubber as the coupling interface. The sensors were lightly compressed against dollops of the gel applied to the samples, squeezing out the excess, and then left to cure for a period of at least 16 hours.

Afterwards, the cables between the sensors, preamplifiers and computer were connected and the set-up was tested using AST function of the AE system where acousto-ultrasonic signals were sent between the sensors and the time delays and amplitudes observed. Also Pencil Lead Breaks (PLBs) were performed within the sensor arrays on the test samples and the estimated AE event location compared with the actual physical location of the PLB as a means to verify the sensors were connected to specific channels. The basic AE system settings used in all the tests are given in Table 3 6.

The system required a user defined input of wave propagation velocity in the test material. This value was determined by performing several PLBs at a specific location just outside an array of two sensors and in-line with both sensors. The average maximum time delay between the sensors, which is also referred to as Event Definition Time (EDT), for all the trials was calculated and given the distance between the sensors the average wave velocity was

determined to be approximately 5.5 km/s. Default values for PDT, HDT and HLT[44] were also used.

Table 3.6: Basic AE system configuration

Sampling rate	2MS/s
Detection threshold	45dB
Pre-amplfication	40dB
Wave velocity	5.5km/s
Frequency range	100 - 1000kHz
PDT	$200\mu s$
HDT	$800\mu s$
HLT	$100\mu s$
Max. duration	100ms

The load output of the test machine was monitored by the AE system via a $\pm 10V$ analog input. The multiplier for converting the measured voltage to applied load was determined using the expression in Equation 3-2. Two levels of loads were applied; L_1=2kN, L_2=20kN and their corresponding voltage outputs were measured; V_1=0.67V, V_2=6.70V. The multiplier was obtained as 2.99V. The threshold for cycle counting is dependent on the mean applied load and this was set accordingly in the various tests using the derived multiplier.

$$Multiplier = \frac{L_2 - L_1}{V_2 - V_1} \tag{3.2}$$

With the test samples gripped at the top and bottom ends, spurious AE signals can be expected to be generated from these regions which could be mistaken for the AE signals of interest being generated from the fatigue crack.

Although the expected maximum time delay of an AE signal between a pair of sensors can be used as a basis for rejecting AE signals originating from outside the sensor array, there is also a possibility for some of these spurious AE events to be located within the sensor array depending on where the sensor array is positioned with respect to the spurious AE sources. This is because for every value of time difference of arrival between a pair of sensors there is an ambiguous region where the AE event might have taken place. For example, considering an AE event occurring exactly midpoint between two sensors, the time difference of arrival would be zero and the possible origin

could be anywhere along a straight line through the midpoint of the array as illustrated in Figure 3 9. For increasing values of TDOA this would take an increasingly curved parabolic shape [61] which could be receptive to the unwanted signals from the test machine grips even with the sensors positioned on a single horizontal axis. The optimal location of the sensor array with respect to the anticipated crack path trajectory and the location of the test machine grips was therefore required.

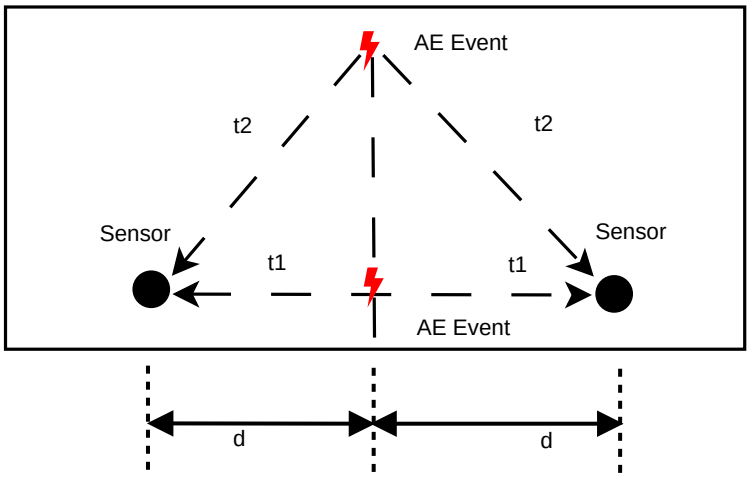

Figure 3.9: Equal TDOA values for AE events occurring at different locations

$$t_1 = v^{-2}\left[(x_i - X_1)^2 + (y_j - Y_1)^2\right] \tag{3.3}$$

$$t_2 = v^{-2}\left[(x_i - X_2)^2 + (y_j - Y_2)^2\right] \tag{3.4}$$

$$\Delta t(1,2)_{i,j} = t_2 - t_1 \tag{3.5}$$

Where,

v - *Wave velocity*
X,Y - *Sensor locations*
x,y - *AE event locations*

The TDOA for an AE event occurring at a particular location can be determined by solving the expressions in Equations 3.3, 3.4 and 3.5 [60]. A MATLAB routine was written to determine the TDOA profile for various sensor configurations. This was done by creating a grid of the test sample area and

the TDOA computed for each point. Contour plots were used to represent the distribution of the resulting TDOA values and optimal sensor locations derived for different configurations.

Two configurations of the AE system were adopted to enable separation between genuine and spurious AE data; the Delta T and Guard Sensor configurations.

Delta T configuration

This set-up consisted of a pair of sensors mounted on the test samples with one sensor on either side of the anticipated crack path which was across the width of the sample and midway of its length. The sensor mounted in the top half of the sample was positioned closer to the anticipated crack plane than the other sensor as means to further verify the AE event location results because AE signals generated along the anticipated crack path would be expected to arrive at the closest sensor first. The registered AE events were located in a 1D plane along the longitudinal axis of the test samples.

For the SEN samples, a pair of sensors 200 mm apart and positioned on a single horizontal axis was used. A timing filter was set where AE events with TDOA values greater or less than a specified range were rejected. The optimal location of the sensors with respect to the test machine grips, which also allowed the largest timing filter window, was observed midway of the samples width. The TDOA profile is shown in Figure 3 10. Although both positive and negative values of TDOA shown do not appear to extend to the top and bottom ends of the test sample, extreme values of TDOA would tend even more towards the corners of the grips and hence a propensity for AE events occurring in the region to be registered within the sensor array. The sensor array is most susceptible to AE signals generated from the bottom grips because the sensor in the bottom half of the sample is closest to either of the grips. The timing filter was set between 28 μs and -23 μs, thereby creating an active sensing region between 172 mm and 320 mm on the horizontal axis.

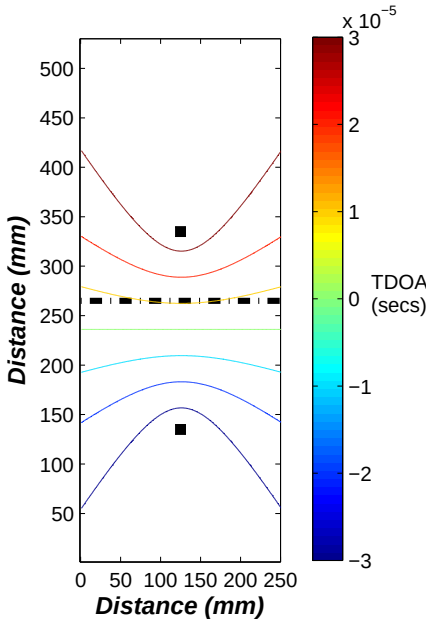

Figure 3.10: TDOA profile for Delta T setup on SEN samples

For the M(T) samples, three pairs of sensors positioned on three horizontal axes were used to monitor the fatigue crack. The pair of sensors on the right hand side, middle and left hand side is referred to as Location Group 1, 2 and 3 respectively and the sensors in each array were spaced 200 mm apart.

The TDOA profiles for the three sensor arrays are shown in Figure 3 11. It can be seen that that of Location Group 2 is exactly like the profile observed in sensor layout for the SEN sample and thus the settings were used to configure this group of sensors. For both Location Groups 1 and 3 it can be seen that some values of TDOA extend into regions of the test sample where the test machine grips were located, implying that AE signals generated from the right hand side of the grips would be registered in Location Group 3 and vice versa for Location Group 1. To avoid this occurrence an adequate range of acceptable TDOA values which would filter out the spurious AE signals was chosen, however this implied that the sensing region between the sensors was effectively reduced. The timing filters for both Location Group 1 and 3 were set between 25 μs and -23 μs, creating an active sensing region between 172 mm and 303 mm on the horizontal axis.

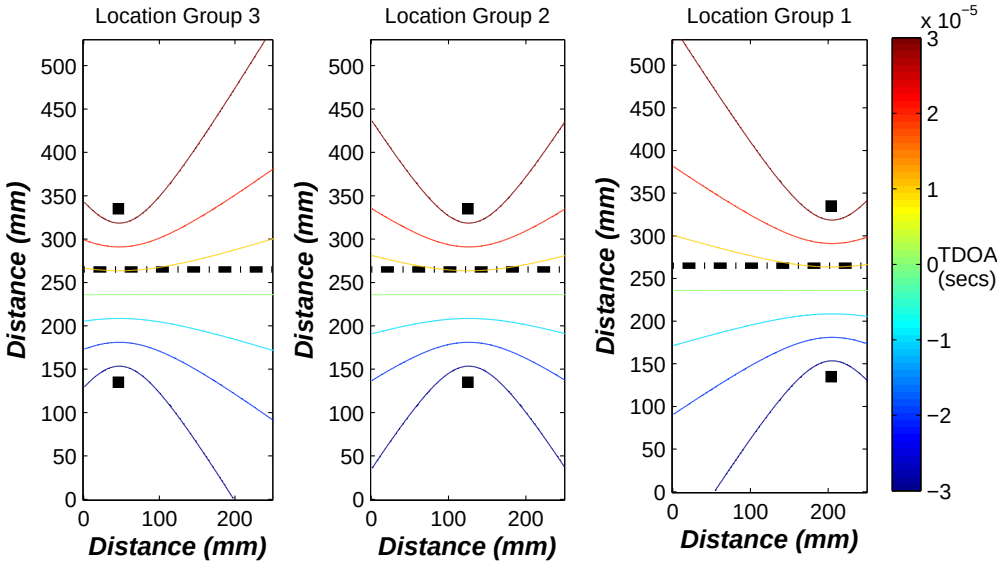

Figure 3.11: TDOA profile for Delta T setup on M(T) samples

Several PLBs were performed outside the sensor array and in the vicinity of the test machines grips to simulate spurious AE events and none of them were registered as valid AE events within the sensor array. A number of PLBs were also performed within the sensing region and were successfully detected and located.

Guard sensor configuration

This configuration utilised a pair of guard sensors to filter out spurious AE signals generated from the test machine grips. One guard sensor was positioned in the vicinity of either test machine grip. The concept is that once an AE signal generated from the machine grips was detected by the guard sensor a system lockout is triggered for a specified amount of time where the crack monitoring sensors do not acquire any AE signals.

For the SEN test samples, four additional sensors were used to monitor AE signals generated from the crack. One pair was in the same locations as in the Delta T configuration and the other was located closer to the edge of the sample where the crack was expected to initiate as illustrated in Figure 3 12. One of the reasons for this configuration was to perform 2D location estimation of AE events during crack propagation. Furthermore, the data recorded by the sensors could be treated as two independent 1D arrays where observations on the influence of the sensor locations with reference to crack length in terms of

detection sensitivity can be made. The pair of sensors closer to the edge of the sample is referred to Location Group 1 and the other pair referred to as Location Group 2.

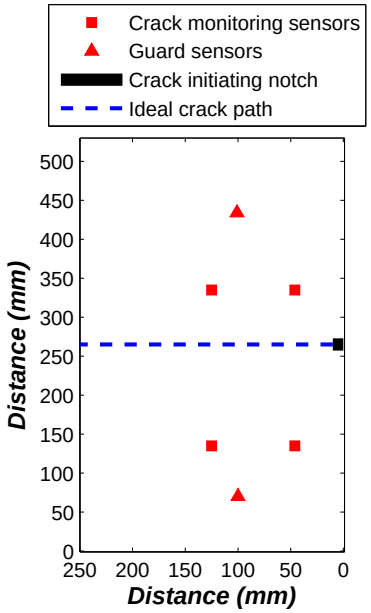

Figure 3.12: Layout for guard sensor configuration on SEN samples

For this setup to function properly it was absolutely essential to ensure that the spurious AE signals from the machine grips always arrived first at either guard sensor before any of the other sensors in the network. The TDOA profiles for the guard sensors paired up with the next closest sensors are shown in Figure 3 13. The positive values of TDOA indicate first arrival at the guard sensors and negative values of TDOA indicate first arrival at the other sensors in the pairs considered. It can be seen in both illustrations that the negative bias of TDOA covered the entire width of the test samples which suggested that the chosen guard sensor locations satisfied the requirement for filtering out spurious AE signals from the test machine grips.

A similar approach was used in the case of the M(T) samples. A pair of sensors was used to monitor each fatigue crack and guard sensors were also used as a means of filtering out spurious AE signals from the test machine grips as illustrated in Figure 3 14. Again, the crack monitoring sensors mounted in the top half of the sample is positioned closer to the anticipated crack plane than the other sensor as means to further verify the AE event location results because AE signals generated from the crack would be expected to arrive at the closest sensors first. The crack monitoring sensor locations were identical

to those in the Delta T configuration.

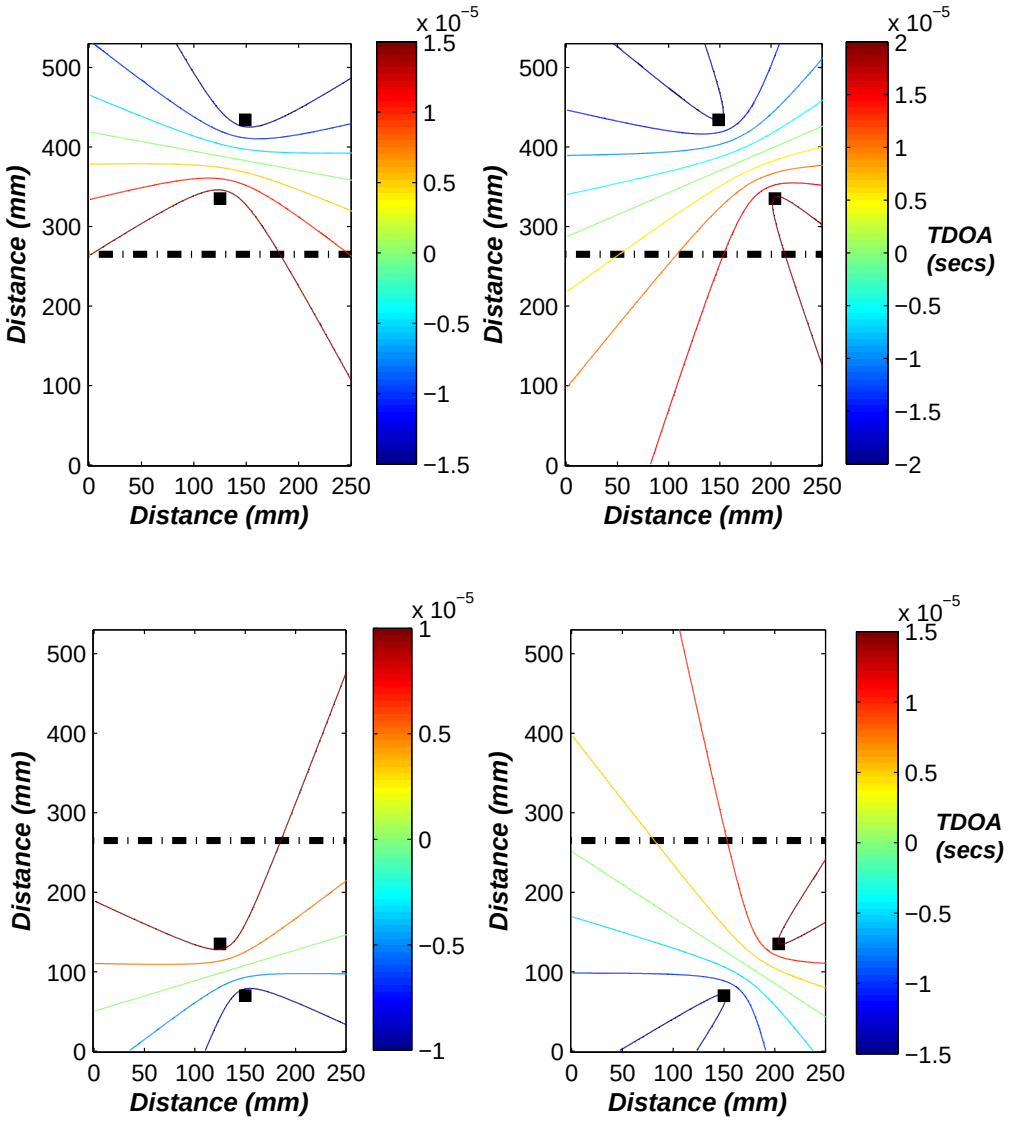

Figure 3.13: TDOA profile for guard sensor configuration on SEN samples

The optimal locations of the guard sensors with respect to the test machine grips were determined using the procedure previously described. The TDOA profiles for the guard sensors paired up with the next closest sensors are shown in Figure 3 15. Again, negative TDOA values indicate the region where the occurrence of an AE event would result the AE signal first arriving at the guard sensors. In both figures it can be seen that this region occupies the entire width of the test where the test machines grips would be located.

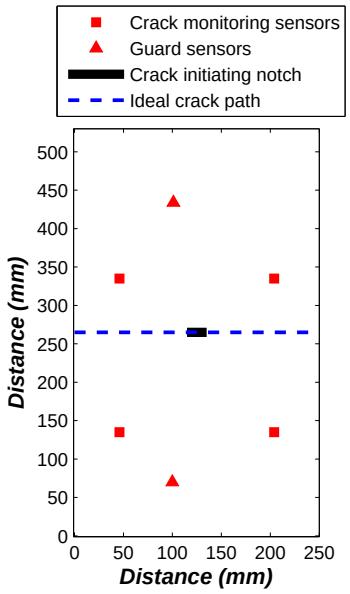

Figure 3.14: Layout for guard sensor configuration on M(T) samples

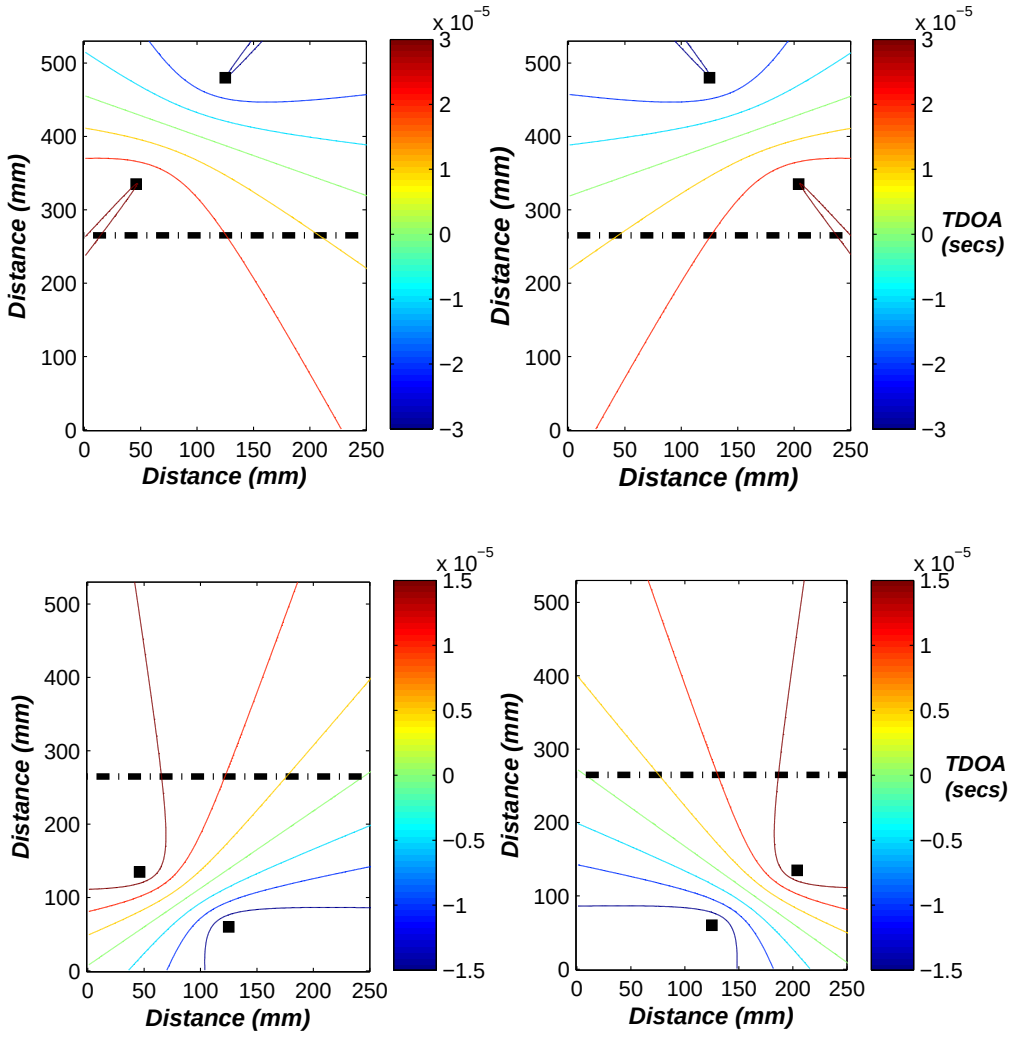

Figure 3.15: TDOA profile for guard sensor configuration on M(T) samples

3.4 Wing-box Test Structure

3.4.1 Fatigue test machine and setup

The test rig consisted of a central pedestal to which two wing-box test structures were bolted on a horizontal plane. The rig was designed such that either wing-box could be easily removed and replaced. A CAD model of Platform 2 and the internal structure of the spars and ribs are shown in Figure 3 16 and Figure 3 17 respectively. The wing-box utilised in this setup consisted of a network of metallic ribs and spars made from AA7075-T651 material, with Carbon Fibre Reinforced Polymer (CFRP) composite skins bolted to the top and bottom of the wing-box, in a similar configuration to that found on CF-18 aircraft. A layer of aerospace grade sealant was applied between the metallic structure of the wing-box and the skins before they were fastened together. Two 25 kN loading actuators, equipped with 22 kN load cells, were attached to the tip of the wing-boxes.

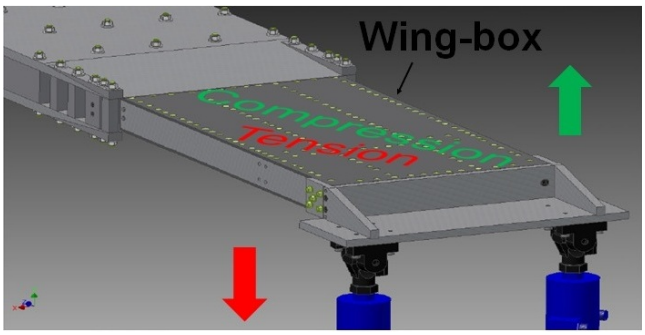

Figure 3.16: Test setup of wing-box assembly (Platform 2) showing loading directions and consequent induced force in the top skin where the flange of the spar with the crack was attached

Figure 3.17: Network of spars and ribs in wing-box

The actuator loaded the wing in cyclic bending. Cyclic bending loads were applied so that the following stress states could be produced on the upper and lower skins

1. Cyclic tension on the top surface with cyclic compression on the bottom surface, with top surface R ratio of 0.1 (tension-tension).
2. Reversed loading on both top and bottom surfaces with top surface R ratio of -0.25 (tension-compression).

The complete test rig consisted of two such wing-box structures. All experiments in this study were performed in the southward facing wing-box which was designed to accommodate an additional internal C channel spar manufactured with a 'hidden' crack emanating from a fastener hole, not visible to the naked eye. Details of the crack seeding process can be found in Yanishevsky et al.[93]. There were a total of 15 fastener holes in both the top and bottom flanges of the test spar with a pitch distance of 25.4 mm. The test sample also contained a fuel weep-hole machined into the web which is representative of a realistic aircraft design feature. The test sample is shown in Figure 3 18.

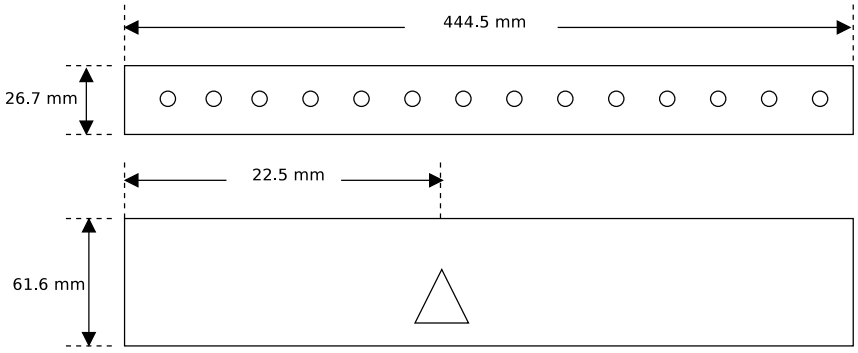

Figure 3.18: Schematic plan and side view of test sample with fuel hole cut-out

Prior to performing tests on this platform, the spar test sample was fatigued by NRC to initiate a crack at one of the fastener holes. The location of the crack remained undisclosed until after completion of all tests. Although only one fatigue crack was introduced in the sample, with the local stress of 59 MPa (10 ksi) in the crack vicinity, there was also the possibility of another crack initiating during fatigue loading.

The tests conducted with this setup were as follows:

1. Constant amplitude sinusoidal loading in tension-tension with a frequency of 0.667 Hz and loading range between 0.56 kN and 5.6 kN.

2. Constant amplitude loading in tension-compression with a frequency of 0.5 Hz and loading range between -1.4 kN and 5.6 kN.

3.4.2 Acoustic Emission setup

A 1D (2 sensor) AE event location setup was used to monitor the test sample with the sensors attached to the spar web. There were a total of 15 fastener holes on each flange of the test sample. The choice of sensor location was constrained by the fact that the pitch distance of the various fastener holes including their respective nut-plates was less than 25.4 mm and the sensor diameter was 20 mm. In other words, there was no other feasible location for the sensor apart from along the web.

Another 1D AE sensor array was attached to one of the adjacent spars at similar locations to that on the test sample. The pair of sensors on the test sample in this report is also referred to as Location Group 1, which consisted of Sensors 5 and 6. Similarly, the pair on the adjacent spar is referred to as Location Group 2 and consisted of Sensors 3 and 4. A schematic of the wing-box layout and the AE sensor arrays are illustrated in Figure 3 19.

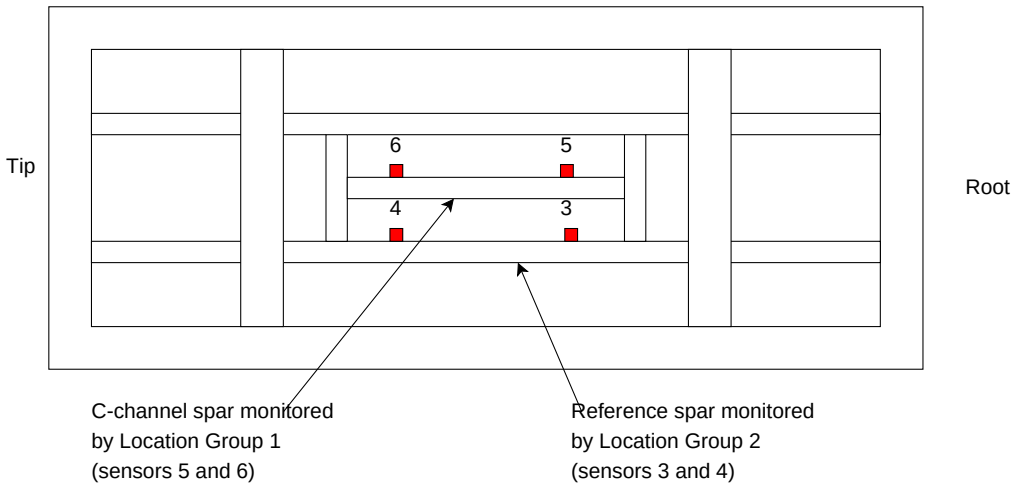

Figure 3.19: Schematic plan view of AE sensor setup in the wing-box

The sensors were positioned as far as physically possible away from each other to maximise their sensing coverage area and bonded to the structure using Dow Corning RTV silicone rubber. This was achieved by coupling the sensors in an upright position to allow for even distribution of the couplant and also to prevent them from slipping out of position during the curing period. This process may not be feasible where the structure being monitored cannot be

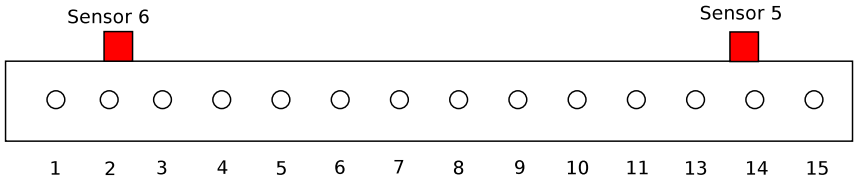

Figure 3.20: Schematic plan view of AE sensor setup on test sample (Location Group 1)

oriented to allow the sensors cure in an upright position. Alternative methods of sensor coupling will be required in such cases.

The AE sensors were connected to the pre-amplifiers via 1 m long cables and to the data acquisition system via 20 m long cables. The pre-amplifiers were situated outside of the wing-box assembly and the cable routed through holes drilled in the neutral axis of the spars. Precaution was taken to ensure that the cables were securely fastened to prevent spurious AE generation as a result of cable movement during fatigue loading. This was done using sticky-tape and cushion foam to line the circumference of holes the cables were routed through.

The position of the sensors and fastener holes on the longitudinal axis of the test spar and the wing-box structure are giving in Table 3 7. Although each pair of sensors was spaced as far apart as possible this could only extend between hole numbers 3 to 13 inclusively, which limited the region of feasible AE events location estimates

Table 3.7: Locations of the sensors and fastener holes on the longitudinal axis of the test sample and wing-box

Hole/ Sensor	Position along the spar (mm)	Position along the wingbox (mm)		Position along the spar (mm)	Position along the wingbox (mm)
Hole 3	70.8	417.8	Hole 9	223.2	570.2
Hole 4	96.2	443.2	Hole 10	248.6	595.6
Hole 5	121.6	468.6	Hole 11	274.0	621
Hole 6	147.0	494.0	Hole 12	299.4	646.4
Hole 7	172.4	519.4	Hole 13	324.8	671.8
Hole 8	197.8	544.8	Sensor 5	60.0	407
Sensor 3	60.0	407.0	Sensor 6	347.0	694
Sensor 4	347.0	694.0			

3.5 Concluding Remarks

The experiments outlined for the coupon samples were designed to exclusively monitor AE signals generated from fatigue crack, which will enable quantitative characterisation in terms of AE event detection, location and classification. This will form the basis for verifying the performance of the AE techniques in monitoring a structural component, as well as validating its capability in detecting and locating fatigue crack in a realistic wing-box structure.

Chapter 4

Quantitative Characterisation of AE Generation From Fatigue Crack

4.1 Introduction

Fatigue tests were performed on both Single Edge Notch (SEN) and (MT) coupon samples, described in Chapter 3, under constant and variable amplitude loading conditions with the objective of characterising Acoustic Emission (AE) generated during fatigue crack propagation. The results from these tests are presented in this chapter where performance metrics were developed and used to process the data recorded.

4.2 Measurement of wave velocity and AE system performance

The AE system requires estimation of AE wave velocity in the propagating medium as input for estimating AE event location. The AE system was used in measuring the time difference of arrival of AE signals traversing the test sample between a pair of sensors separated by fixed distances and the wave velocity determined using the expression in Equation 4.1.

$$Velocity(km/s) = \frac{Distance}{Time} \tag{4.1}$$

Measurements of time difference of arrival (TDOA) were obtained using the setup shown in Figure 1. The sensors were positioned 350 mm apart on a 2mm thick 2014 T6 aluminium sample and five Pencil Lead Breaks (PLBs) were performed just outside of the sensing region. The signals were detected by the sensors by means of First Threshold Crossing (FTC), where the signal amplitude first exceeds a detection threshold which was set at 45 dB, and time stamps were appended to each of these signals. Values of TDOA were simply

obtained by determining the delays in the recorded times.

Figure 4.1: Setup for determining propagation velocity of AE signals in 2mm thick 2014 T6 aluminium plates

The results from five test trials are given in Table 4-1, showing the measured time difference of AE signals arriving at the sensors and their respectively calculated wave velocities. The average wave velocity was determined as 5.59 km/s ±0.1. It can also be seen that the timing measurements varied by 1 μs, which was also the expected timing resolution of the AE system [44].

Table 4.1: Results from test trials to determine AE wave velocity in 2 mm thick 2014 T6 aluminium plates

Trial	Distance(mm)	Time Difference of arrival(μs)	Velocity(km/s)
1	350	63	5.55
2	350	62	5.65
3	350	62	5.65
4	350	63	5.55
5	350	63	5.55
			Mean = 5.59

Assuming wave velocity of 5.59 km/s and given the time measurement precision of 1 μs, an error margin of ±5.59mm can be expected from the AE system as a result of this timing measurement error.

The AE signal wave velocity in the test samples were verified through simulations using the PACshare software to generate dispersion curves which shows the relationship between the group and phase velocities to the frequencies of AE signals, as described in Section 2.3.1. This can be achieved by solving the governing wave propagation equation given the boundary conditions [7]. The required inputs were the thickness of the test sample as well as material properties which include Poisson's ratio, shear modulus and density. The results of the group and phase velocities for both the extensional and flexural wave

modes are shown in Figure 4-2. The wave velocity for the extensional wave mode (S_0 is observed to be greater than the flexural wave mode A_0 for frequencies up to 1 MHz where they converge. It can be assumed that the frequencies components at the leading edge of the signal in this range would correspond to the frequency of the extensional wave mode as they are generally of a higher velocity and therefore expected to arrive at a sensor before the flexural mode.

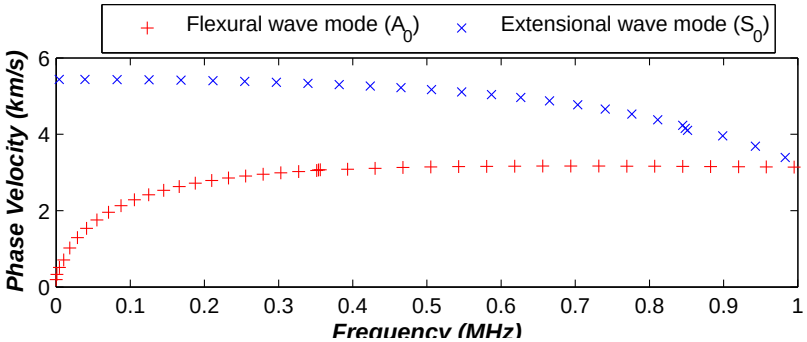

Figure 4.2: Simulated dispersion curves for extensional and flexural wave modes in 2 mm thick aluminium plates

The time domain plot of an AE signal generated from a PLB AE event is illustrated in Figure 4-3 alongside its time-frequency spectrum obtained using the Gabor wavelet transform [94]. It can be observed that at the onset of signal detection there were frequency components at 250 kHz and 500 kHz with the highest amplitude at 250 kHz. Correlating these frequencies with the simulated phase velocities of the extensional wave mode in Figure 4-2, it can be seen that they correspond to velocities of 5.4 km/s and 5.3 km/s respectively, which is comparable to the value determined experimentally. The difference can be attributed to approximations made in simulations as well as errors made in measurement.

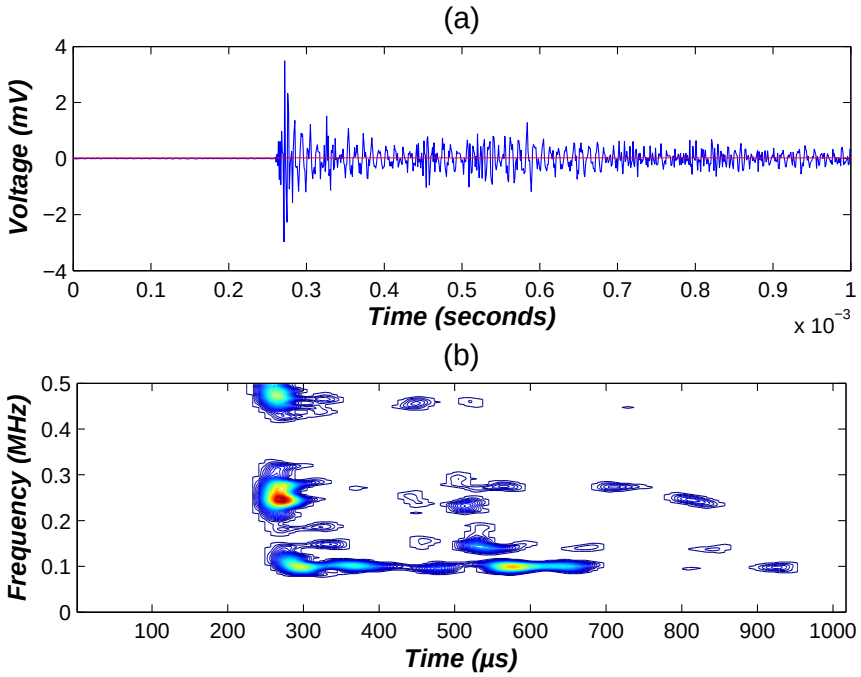

Figure 4.3: Typical AE signal generated from PLB tests (a) in the time domain and (b) in the time-frequency domain

The performance of the AE system was measured in terms of accuracy in locating simulated AE events in simplified configurations using the measured value for propagating wave velocity. This was conducted by performing PLBs across the area of a 450 x 550 mm test sample using a 3-sensor and 4-sensor array as well as a 3-sensor array on a 1 x 2 m test sample and the results are illustrated in Figure 4-4, Figure 4-5 and Figure 4-6 respectively which shows the estimated PLB location and the actual PLB location with adjoining error vectors. It is observed in all samples that the minimum errors were in the middle of the test sample and the largest errors were mostly towards the edge. This type of location error distribution is referred to as Geometric Dilution of Precision (GDOP) [95] where greater location errors are obtained as a function of measurement errors as well as position of the sensors with reference to the AE events, which is generally considered as regions farther away from the middle of sensor pairs used in triangulation.

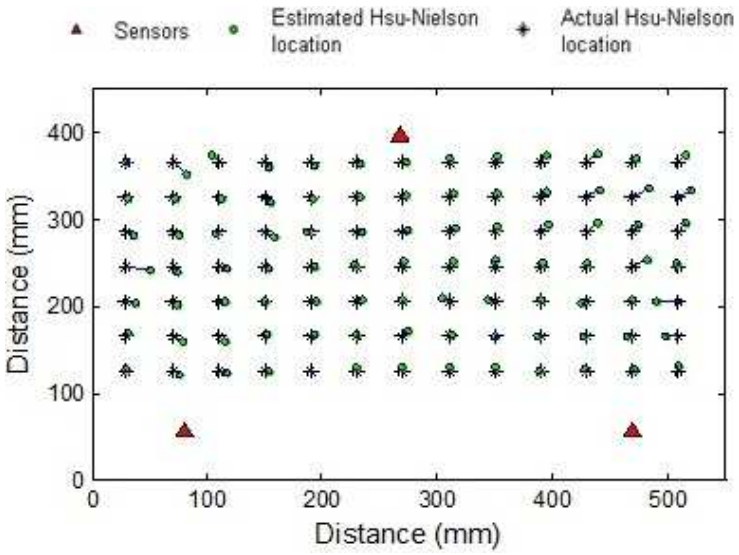

Figure 4.4: Pencil Lead Break AE source location on a 450 x 550 mm aluminium sheet using the AE system with a 3-sensor setup

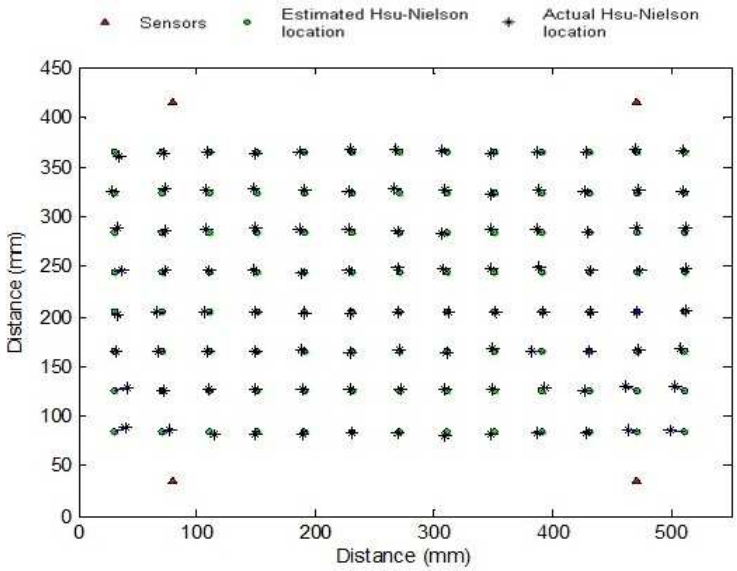

Figure 4.5: Pencil Lead Break AE source location on a 450 x 550 mm aluminium sheet using the AE system with a 4-sensor setup

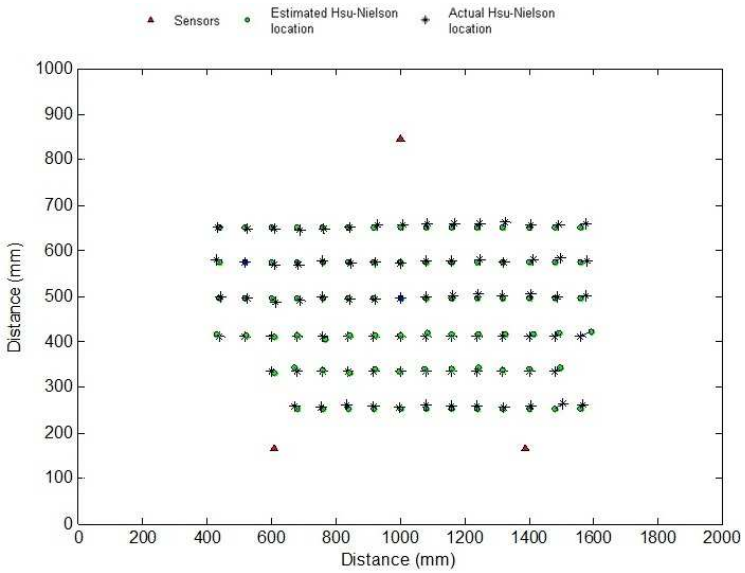

Figure 4.6: Pencil Lead Break AE source location on a 1 x 2 m aluminium sheet using the AE system with a 3-sensor setup

Location error characterisation was performed using the Probability of Location (POL) metric given in Equation 4.2. The error vectors at each AE event location were determined, after which they were ranked and the cumulative frequencies of the various error margins computed.

$$P(x_j) = \frac{number of observations \leq x_j}{n+1}, x_1 \leq x_2 \leq ... \leq x_n \qquad (4.2)$$

The results obtained are illustrated in Figure 4-7 where at 90% cumulative frequency the error margins for the 4 and 3-sensor setups on the 450 x 550 mm sample and the 3-sensor setup on the 1 x 2 m sample were 5.4 mm, 11.2 mm and 16.3 mm respectively. Better location accuracy is obtained with the 4-sensor setup than with the 3-sensor setup because, although only 3 sensors are essentially needed for the 2D location estimation, the redundant TDOA information from the fourth sensor can form four combinations with those from the other sensors which can result in four different location estimates. Averaging these location estimates can result in reduction of error margins.

Larger error margins at 90% cumulative frequency was observed for the 1 x 2 m test sample than for the 450 x 550 mm test sample despite having the same

number of sensors. This can be attributed to the attenuation due to the longer propagation distance in the larger sample.

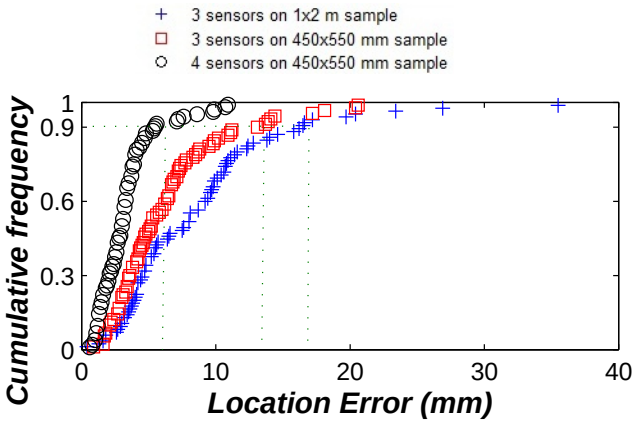

Figure 4.7: Cumulative frequency of error margins with various experimental configurations using Pencil Lead Breaks as AE source

The amplitude response of the AE system was measured by sequentially generating 100 acousto-ultrasonic pulses from a sensor using the AST function of the AE system as described in Section 3.2.3, with each pulse $5\mu s$ long and at 100ms intervals. A total of 17 trials were performed and the average amplitude response of these AE events in each trial was recorded by another sensor 540 mm away from the sending sensor. Figure 4-8 shows the histogram plot of the average signal amplitudes measured at the sensors. It is observed that there is a 1 dB variation which is also the expected resolution specified by the equipment manufacturer [44].

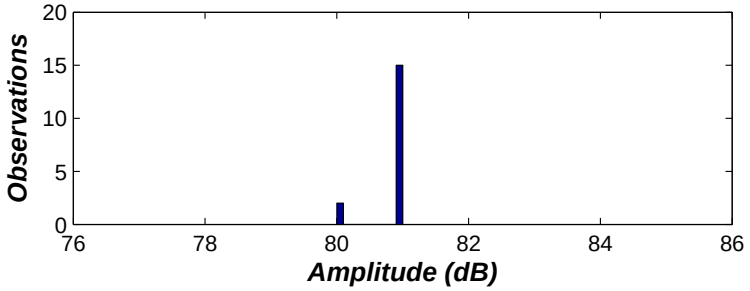

Figure 4.8: Amplitude distribution for AST generated AE events 545 mm away from the receiving sensor

4.3 Fatigue Crack Growth Tests

A total of 16 tests were conducted under constant amplitude sinusoidal loading with 12 of these tests performed on SEN samples and 4 on MT samples as outlined in Table 4-2. Two additional tests were performed on SEN samples under variable amplitude loading using the spectrum described in Section 3.2.2. The fatigue crack initiated at the notch root and propagated perpendicularly to the applied load across the sample width. The fatigue crack initiated easily for the tests with stress range of 52.2 MPa and R ratio of 0.1, however it was not the case for the tests with stress range of 27 MPa and R ratio of 0.1. This was because the reduction in stress range resulted in a reduction in the stress concentration around the notch which was required for crack initiation, as described in Section 2.5.

Crack initiation in the tests with stress range of 27 MPa and R ratio of 0.1 required fatigue loading at greater stress ranges and consequently higher stress concentration at the notch to initiate the crack. Further fatigue loading, at greater stress ranges and consequently higher crack tip stress intensity, was also required to grow the crack to a length which would have sufficiently high enough stress intensity when reverted back to loading with stress range of 27 MPa. This process needs to be performed in stages of gradually reduced stress range to avoid crack blunting when there is a large decrease in stress range [96]. This was achieved by fatigue loading with an initial stress range of 52.2 MPa, afterwards the crack was grown in stages with stress range values of 45 MPa, 38.7MPa and 31.5 MPa respectively up to a crack length of 12mm. The crack tip stress intensity factor at this crack length was determined to be 6.3 MPa$\sqrt{m}$ using the expression in Equation 4.3 and was found to be sufficient to propagate the crack under fatigue loading with a stress range of 27 MPa.

$$\Delta K = \beta \Delta\sigma \sqrt{\pi a} \tag{4.3}$$

Where,

a - *Crack length*
$\Delta\sigma$ - *Stress range*

Table 4.2: Constant amplitude fatigue tests on coupon samples

Test	Notch	Max Stress (MPa)	Stress range (MPa)	Failure crack length (mm)	Total fatigue life (cycles)	AE Setup
1	SEN	58	52.2	118	77294	Delta T
2	SEN	58	52.2	121	114865	Delta T
3	SEN	58	52.2	115	96523	Delta T
4	SEN	58	52.2	120	73821	Delta T
5	SEN	58	52.2	115	74844	Delta T
6	SEN	58	52.2	112	71510	Delta T
7	SEN	58	52.2	121	86865	Delta T
8	M(T)	58	52.2	110	114890	Delta T
9	M(T)	58	52.2	104	112617	Delta T
10	M(T)	58	52.2	100	114890	Guard Sensors
11	SEN	30	27	-	552323	Delta T
12	SEN	30	27	153	782149	Guard Sensors
13	SEN	30	27	150	530965	Guard Sensors
14	SEN	30	27	143	668507	Guard Sensors
15	M(T)	30	27	90	433134	Guard Sensors
16	SEN	58	27	87	258032	Delta T
17	SEN	Decreasing	Decreasing	2	0.1	Guard Sensors

Table 4.3: Results from test trials to determine AE wave velocity in 2 mm thick 2014 T6 aluminium plates

Test	Notch	Max Stress (MPa)	Frequency range	Failure crack (Hz)	Total length (mm)	AE Setup
18	SEN	58	2	2		Guard Sensors

Crack length measurements were obtained from digital images taken during the tests, as described in Chapter 3, and then correlated with cycle counts. Crack length and elapsed cycles data for all the tests are provided in Appendix B. A selection of crack length against number of cycles plots are shown in Figure 4-9 for Tests 1, 11 and 14.

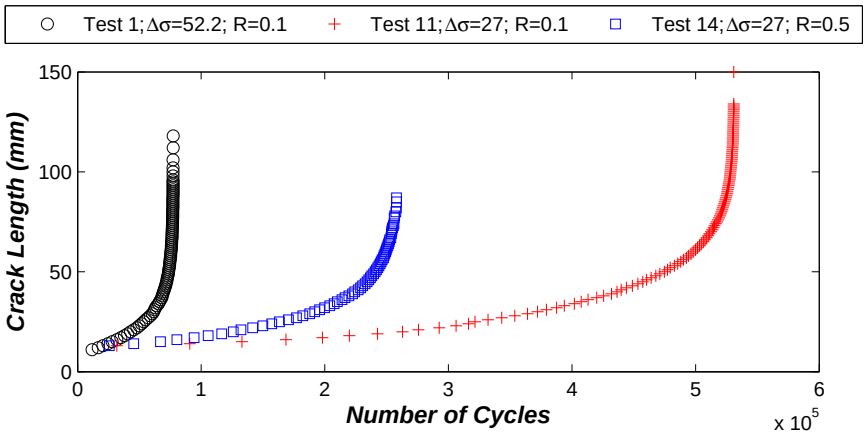

Figure 4.9: Crack length versus number of cycles plot for Tests 1 ($\Delta\sigma$=52.2; R=0.1), Test 12 ($\Delta\sigma$=27; R=0.1) and Test 16 ($\Delta\sigma$=27; R=0.5)

It is observed that Test 1 had the least number of elapsed cycles before sample failure, which occurred at 118 mm, because it had the highest stress range and consequently crack tip stress intensity range which is regarded as the mechanical driving force of crack propagation [97]. Also, although Tests 12 and 16 had the same stress range value, Test 16 required much fewer number of cycles to reach failure because of its higher stress ratio [73].

Crack rotation as described in Section 2.5 was observed in all the tests conducted. On visual inspection, it was typically seen to start at the onset of crack growth and approximately attained the 45 degree angle of rotation at a

total crack length of about 40 mm.

Figure 4-10 illustrates a plot of crack growth rates versus stress intensity range for a selection of tests with stress ratios of 0.1 and one with stress ratio of 0.5. This was performed using the secant method as prescribed in the ASTM standard for measurement of crack growth rates [98]. It can be observed that the crack growth rates are predominantly in the Paris regime (Region II), as described in Section 2.5, because they follow an approximately linear trend. Also, as expected, for all values of ΔK higher crack growth rates were observed in the tests with stress ratio of 0.5 than the other tests with stress ratio of 0.1 [73; 74]. The values of crack growth rates for both stress ratios were compared with similar data from the Engineering Science Data Unit (ESDU) and excellent agreement between them was observed [99].

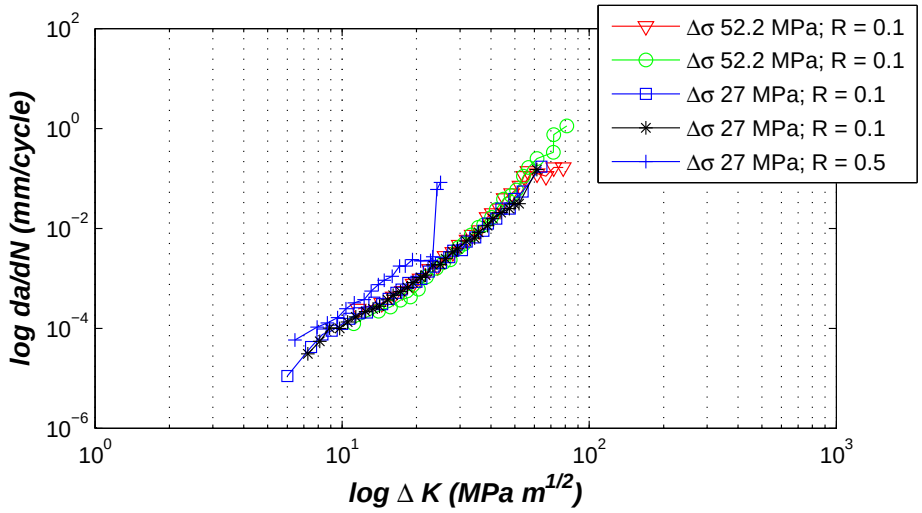

Figure 4.10: Fatigue crack growth rates versus crack tip stress intensity range for tests 1, 9 and 12 with various loading configurations

Inspection of fracture surfaces was performed with a Scanning Electron Microscope (SEM) where evidence of fractured inclusions was found at various lengths of crack growth. Examples are shown in Figure 4-11. Also, evidence of debris collection at various crack lengths was uncovered. Micrograph taken at total crack lengths of 17 mm, 55 mm and 90 mm as shown in Figure 4-12. Both of Figure 4-11Figure 4-12 indicate potential sources of AE signals generation [3; 100]. However it was not possible to validate this or verify their level of intensity using this visual inspection process.

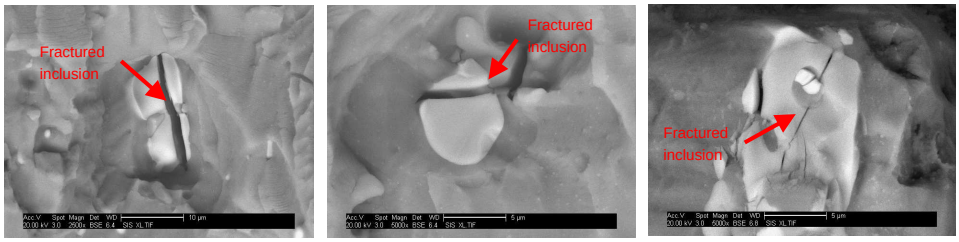

Figure 4.11: Fractured inclusion on crack surface

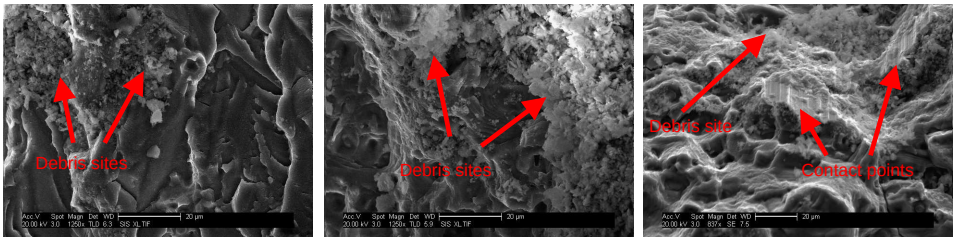

Figure 4.12: Debris collection possibly from crack closure at total crack lengths of 17 mm (left), 55 mm (middle) and 90 (mm)

4.4 Monitoring AE Signals from Fatigue Crack

AE signals were recorded during each of the fatigue tests using both the Delta T and Guard Sensor configurations, as described in Sections 3.2.4.1 and 3.2.4.2 respectively. The main difference between these two approaches is that in the case of the Delta T setup only AE signals associated with particular AE events were recorded i.e. AE signals arriving at the sensors in an array within a specified time window and forming a valid location estimate between the sensors. In the case of the Guard Sensor setup AE signals not associated with particular AE events along with those belonging valid location estimates were recorded, provided they satisfied the necessary conditions of the Guard Sensor setup described in Section 3.2.4.2. The implication of this difference in monitoring schemes is that the Guard Sensor setup may record more AE signals than with the Delta T setup for any given test.

The features derived from each of these signals were described in Chapter 3. After completing each of the tests, data reports containing instantaneous values of these features alongside measured load and fatigue cycle counts were generated by the AE system in text files. This file format was not readily accessible for further processing and a MATLAB routine was developed to extract the measurements recorded in the following steps:

1. Delimit the document column-wise by the spaces between strings of characters.
2. Identify the data variable columns (AE signal measurements and fatigue test data) of interest.
3. Set markers for rows containing observations of the variables identified in 1.
4. Parse through every line of the report delete all rows and columns in the data not corresponding with 2 and 3.

The output of this process were tables of the instantaneous values of the derived AE signal features alongside measured load and fatigue cycle counts.

Correlation of AE data with progressive crack growth is required to understand AE generation during the fatigue process, which underpins the viability of the AE technique in any application. These analyses are typically represented in terms of cumulative numbers of AE signals recorded (Hits) or cumulative sums of derived features such as Counts and Energy, described in Table 3-5, over elapsed cycles or lengths of crack growth [33; 52; 87]. Also, AE data are analysed in terms of rates of change of derived AE signal features like Counts and Energy with elapsed cycles [30; 33; 52; 55].

Although the derived AE signal features can also be correlated with progressive fatigue crack growth, this does not necessarily translate to information on how many recorded AE signals resulted in certain values of these AE signal features because different ranges of values can be expected for AE signals generated at different crack lengths. In other words, a large increase in AE Energy for example may be as a result of just a few discrete high-energy AE events or many low-energy AE events and this may not be intuitively understood from analysis of the derived AE signal features. This has direct implications on the possibility of locating the AE source, which is often needed to verify genuine AE signals [101; 102]. Information on the number of AE Hits recorded with progressive fatigue crack growth is essential to characterise AE generation in the fatigue process.

Preliminary analysis of the data was in terms of cumulative number of AE Hits versus fatigue cycles as illustrated in Figure 4-13. It was observed that there were periods during the test with large increases in AE Hits and other periods with minimal AE Hits. The rates of change associated with the different slopes observed are however not easily discernible and therefore the level of AE

generation at certain points may not be accurately estimated. Also, Tests 1 to 7 which were performed under identical load conditions, as outlined in Table 4-2, had coefficients of variance for failure crack lengths and total fatigue cycle counts of 0.03 and 0.19 respectively. This suggests that there is more variability in the number of loading cycles required for crack propagation and that correlation of recorded AE with crack length would be more meaningful in associating AE signals with the fatigue process.

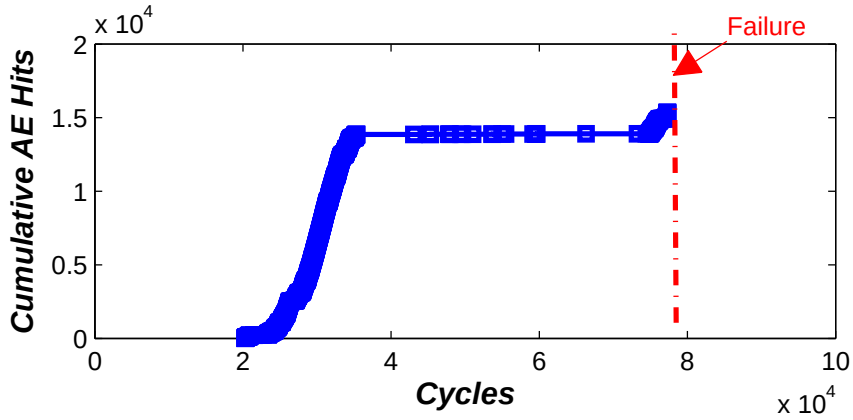

Figure 4.13: Plot of cumulative AE Hits versus fatigue cycles for Test 1 with Stress range of 52.2 MPa and R ratio of 0.1

An understanding of the mechanisms responsible for AE generation at various crack lengths during the fatigue process would give insight to the conditions under which AE generation is promoted or diminished. Metallographic analyses of fracture surfaces have been conducted to identify the mechanisms of AE generation during the fatigue process [83]. This approach however has its shortcomings of ambiguous interpretation when there are several fatigue mechanisms occurring in a particular inspection site as well as also being very challenging to interpret quantitatively.

Monitoring the loads at which AE signals generated from fatigue crack occur would give information on the prevailing conditions which could then be associated with mechanisms during the fatigue process. This approach has not been widely applied in experimental studies using the AE technique with instances of its application seen in Roberts et al. (2003) [31] Carlyle et al. (1976) [103] and Daniel et al. (2007) [87].

Three metrics were developed to interpret the data in terms of the performance of the AE technique in detecting fatigue crack, as well as characterising AE generation from fatigue crack. Computations of these metrics were also

performed in MATLAB.

4.4.1 Metric 1 – AE Hits per mm of crack growth

This is the summation of detected AE signals generated from a particular fatigue crack length over several observations from different test samples with sensors at a fixed location. This gives an indication of the number of AE signals generated at various crack lengths. Values of this metric were determined using the expression in Equation 4.4. Conversions to the Logarithmic scale in base 10 were also made to emphasis subtle trends in the data sets.

$$HitRate_{AE}(i) = log_{10}\frac{1}{n}\left[\sum_{n}^{x=1} H(x)_i\right] \tag{4.4}$$

Where,

h - *Number of hits*
n - *Number of samples*
a - *Crack length*

A total of 18 tests were perform controlled tests and measure the resulting AE signals generated from the crack as a function of varied fatigue loading parameters. All other test variables were held constant as much as possible. In tests 1 to 7 all fatigue loading configurations were set identical to each other and the effect of the differences in the various material batches used in making the test samples on AE signal generation were observed and distinctive trends in AE Hit rates were characterised. In subsequent tests the influence of loading frequency, reduced stress range, increased mean stress and variable amplitude loading were investigated.

Effect of variation in material batch

The test samples were manufactured from three different batches of 2014 T6 aluminium, as outlined in Table 4-2, and the effect of this variation was investigated. The Delta T AE configuration, as described in Section 3.2.4.1, was used in all of these tests and all test samples were tested until complete failure.

Batch 1 material

The results of AE hit rates versus crack length for Tests 1, 2 and 3 are shown in Figures Figure 4-14, Figure 4-15 and Figure 4-16 respectively. Fatigue cracks developed from the notch root after an average of 11134 cycles and the first AE signals were observed at an average total crack length of 11.3 mm in these tests. In Figure 4-14(a), it can be observed that after about 2mm of crack growth there were increasing values of AE Hit rates with a peak of 6300 AE Hits/mm at a total crack length of 17 mm. However, this rapidly declined at a total crack length of 19 mm and after which the AE hit rates observed until sample failure were small in comparison. Plotting the AE Hit rate data on the log scale, as shown in Figure 4-14(b), it can be seen that after the initial burst in AE hit rates between crack lengths of 12 mm and 19 mm, there was a period up to 55 mm crack length where there were less than 100 AE Hits/mm recorded. Afterwards another increase by a factor of 2 between 55 mm and 70 mm was observed, which declined slightly and then increased again in the period leading to sample failure. Figure 4-14(b), it can be seen that after the initial burst in AE hit rates between crack lengths of 12 mm and 19 mm, there was a period up to 55 mm crack length where there were less than 100 AE Hits/mm recorded. Afterwards another increase by a factor of 2 between 55 mm and 70 mm was observed, which declined slightly and then increased again in the period leading to sample failure.

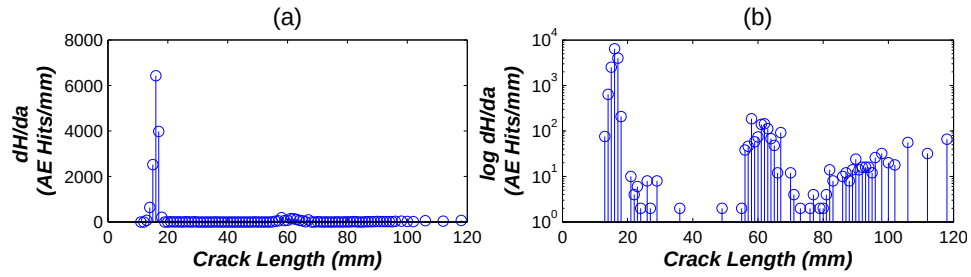

Figure 4.14: AE Hit rate versus crack length from Test 1 with Stress range of 52.2 MPa, stress ratio of 0.1, loading frequency of 2 Hz and Δ K values of 10.2 – 81.7 MPa $\sqrt{m}$

Similar trends in the AE hit rates were observed in Tests 2 and 3, as illustrated in Figure 4-15 and Figure 4-16 from the same material batch as the sample in Test 1. The main differences are that the maximum hit rate at crack lengths less than 20 mm for Test 2 is greater than those observed for Tests 1 and 3 by factors of 2 and 50 respectively. Also, the hit rates for crack lengths between 20 mm and 55 mm for both Tests 2 and 3 are greater than those observed in

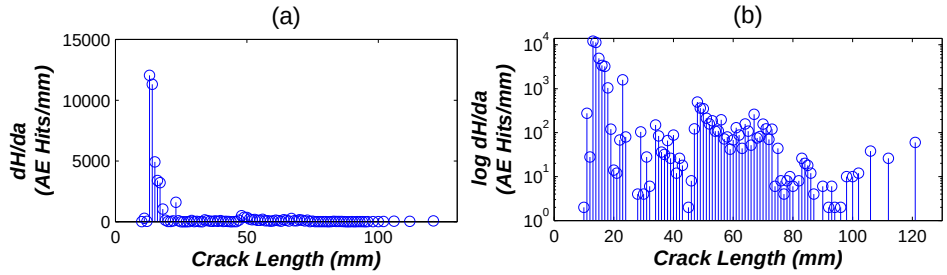

Figure 4.15: AE Hit rate versus crack length from Test 2 with Stress range of 52.2 MPa, stress ratio of 0.1, loading frequency of 2 Hz and Δ K values of 10.2 – 85.3 MPa $\sqrt{m}$

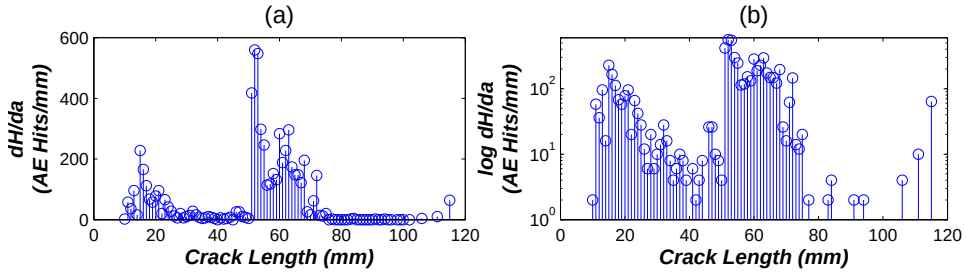

Figure 4.16: AE Hit rate versus crack length from Test 3 with Stress range of 52.2 MPa, stress ratio of 0.1, loading frequency of 2 Hz and Δ K values of 10.2 – 81.1 MPa $\sqrt{m}$

Test 1 although the same trend of rapid decline after an initial peak at crack lengths under 20 mm is observed.

Batch 2 material

The results of AE Hit rates at various crack lengths for Tests 4 and 5 from Batch 2 material were quite similar to each other but significantly different from those obtained from Batch 1. The result for Tests 4 and 5 are illustrated in Figure 4-17 and Figure 4-18 respectively. They were both characterised by AE Hit rates less than 5 AE Hits/mm for crack growth up to a crack length of 60 mm, although noticeably no AE Hits were recorded in this period for Test 5. The first AE signal was detected at a crack length of 63 mm in Test 5 whereas this occurred at a crack length of 11 mm for Test 4. The main similarity to the tests performed on samples from Batch 1 material was the increase in AE Hit rates 120 observed in the period just before sample failure. The peak AE Hit rates just before final failure were comparable to those of Batch 1 material as they were observed between 70 Hits/mm and 90 Hits/mm, while in Tests 4 and 5 they were observed to be 150 Hits/mm and 90 Hits/mm respectively.

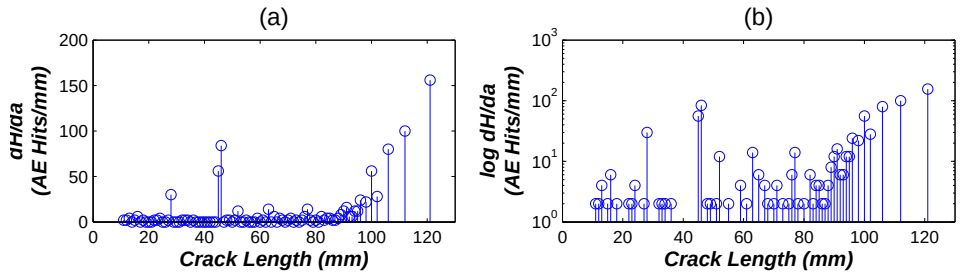

Figure 4.17: AE Hit rate versus crack length from Test 4 with Stress range of 52.2 MPa, stress ratio of 0.1, loading frequency of 2 Hz and Δ K values of 10.2 – 85 MPa $\sqrt{m}$

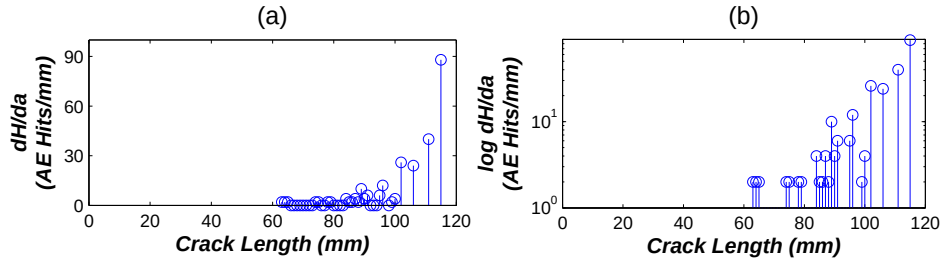

Figure 4.18: AE Hit rate versus crack length from Test 5 with Stress range of 52.2 MPa, stress ratio of 0.1, loading frequency of 2 Hz and Δ K values of 10.2 – 81.1 MPa $\sqrt{m}$

Batch 3 material

In the case of Tests 6 and 7 which had samples made from Batch 3 material, the results obtained were very similar to each other. Figure 4-19 and Figure 4-20 illustrate the results of AE Hit rates at various crack lengths for Tests 6 and 7 respectively. They were characterised by AE Hit rates less than 12 Hits/mm up to a crack length of 50 mm in Test 6 and 45 mm in Test 7. There was a period of increase and decline in AE Hit rates for crack lengths between 50 mm and 70 mm, with peak rates of 100 Hits/mm in Test 6 and 500 Hits/mm in Test 7 which occurred at 60 mm in each of the tests. Also there was a steady increase in AE Hit rates in the period leading to sample failure with maximum peaks between 90 – 100 Hits/mm.

It was observed that both tests also bore some similarities with those obtained from the tests on Batch 1 samples in terms of the peak and then decline in AE Hits rates for crack lengths between 55 mm and 70 mm. The peak AE Hit rates in this period were also comparable as they were observed between 100 – 160 Hits/mm in Batch 1 and 110 – 140 Hits/mm in Batch 3. Also the increase in AE Hit rates in the period leading to sample failure as previously described

was again observed. However the initial peak in AE Hit rate at crack lengths less than 20 mm observed in tests with samples from Batch 1 material was not apparent in these tests on samples from Batch 3 material.

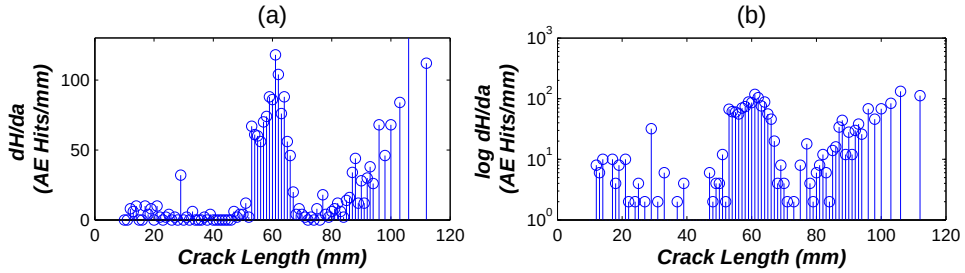

Figure 4.19: AE Hit rate versus crack length from Test 6 with Stress range of 52.2 MPa, stress ratio of 0.1, loading frequency of 2 Hz and Δ K values of 10.2 – 79.6 MPa $\sqrt{m}$

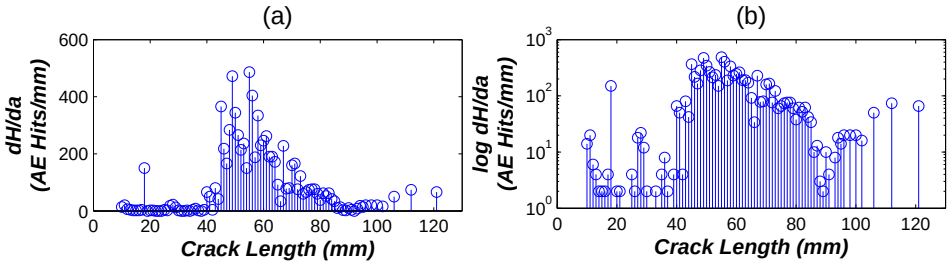

Figure 4.20: AE Hit rate versus crack length from Test 7 with Stress range of 52.2 MPa, stress ratio of 0.1, loading frequency of 2 Hz and Δ K values of 10.2 – 85.3 MPa $\sqrt{m}$

It was observed across Tests 1 to 7 that samples from each batch of material exhibited similar behaviour in terms of AE Hit rates at various crack lengths. The test samples from Batch 1 exhibited the highest AE Hit rates, particularly at crack lengths less than 20 mm which were at least between 2 – 130 times greater, although the Hit rates at other periods of crack growth were comparable by factors less than 5.

Average AE Hit rates for Tests 1 to 7

The average AE hit rates at various crack lengths for all 7 tests on SEN samples under constant amplitude loading was calculated using the expression in Equation 4.4 and the results are shown in Figure 4-21 where four stages can be identified as follows:

1. **Stage 1:** A rapid increase and then decrease in AE Hit rates for crack growth up to a length of about 20 mm with peak at 17 mm.

2. **Stage 2:** Minimal AE Hit rates less than 30 Hits/mm for crack lengths between 20 mm and 55 mm.

3. **Stage 3:** An increase and then decrease in AE Hit rates at crack lengths of 55 mm and 70 mm respectively with peak AE Hit rate of 110 Hits/mm.

4. **Stage 4:** An increase in AE Hit rates in the period leading to samples failure.

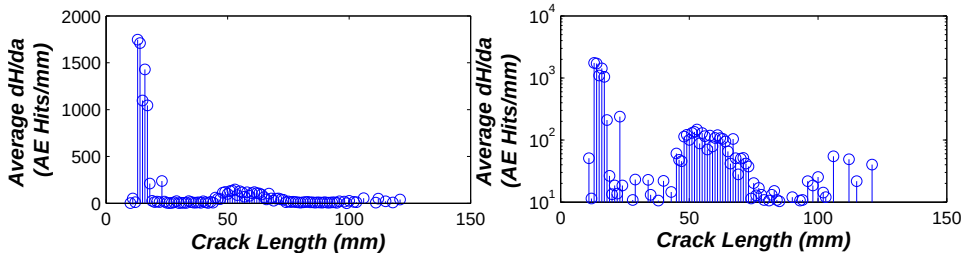

Figure 4.21: Average AE Hit rate versus crack length for Tests 1 to 7 with Stress range of 52.2 MPa, stress ratio of 0.1 and loading frequency of 2 Hz

It was observed that the maximum average AE Hit rate in Stage 1 was at least 15 times more than the average AE Hit rates observed at other periods during the tests. Comparing this trend to the fatigue cycles data, provided in Appendix C, it was found that on average Stage 1 occurred for about 53% of the samples fatigue life, Stage 2 for about 32% and the Stages 3 and 4 for the final 5% before failure, as shown in Figure 4-22.

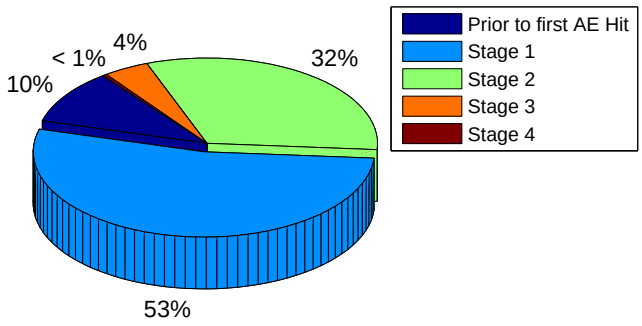

Figure 4.22: Proportion of averaged fatigue life where the stages in AE generation for Tests 1 to 7 occurred

Despite the limited number of tests, the standard deviation of the distribution of AE Hit rate at various crack lengths was also calculated and the results are illustrated in Figure 4-23. It can be observed that there was a great amount of variability in data, most particularly at crack lengths less than 20 mm.

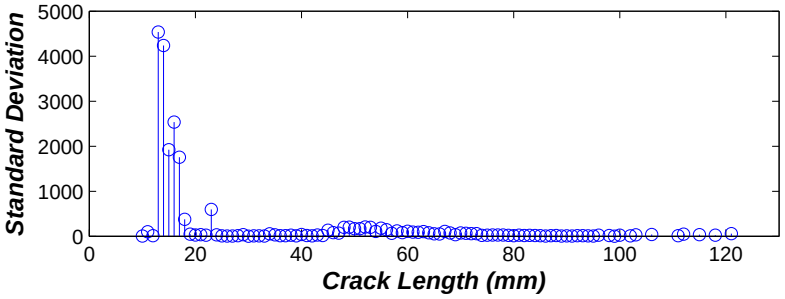

Figure 4.23: Standard deviation of the distribution of AE Hit rate at various crack lengths for Tests 1 to 7 with Stress range of 52.2 MPa, stress ratio of 0.1 and loading frequency of 2 Hz

Effect of sample geometry

Tests 8 and 9 were performed on MT samples where fatigue cracks emanated from either end of the notch and the Delta T AE setup was used to monitor the resulting AE signals, with Location Groups 1 and 3 positioned towards the right and left edge of the sample respectively and Location Group 2 in the middle as described in Section 3.2.4.1. Fatigue loading was performed with stress range of 52.2 MPa, stress ratio of 0.1 and loading frequency of 2 Hz, which was identical to the load configuration used in Tests 1 to 7 as outlined in Table 4-2. The effect of change in sample geometry was observed from the results of AE Hit rates at various crack lengths for the three pairs of sensors in both Tests 8 and 9. Figure 4-24, Figure 4-25 and Figure 4-26 illustrate the results obtained for Location Groups 1, 2 and 3 respectively in Test 8 and Figure 4-27, Figure 4-28 and Figure 4-29 illustrate the results obtained for Location Groups 1, 2 and 3 respectively in Test 9.

The results for Test 8 were characterised by an initial peak in AE Hit rates between 1700 – 2400 Hits/mm for fatigue crack growth to lengths up to 30 mm with other intermittent peaks between 500 – 700 Hits/mm at crack lengths between 40 mm – 60 mm in Location Groups 1 and 3.Another peak was observed in the period just before sample failure. This loosely followed the trend in average AE Hit rates shown in Figure 4-21 for SEN samples. It was however also noted that the AE Hit rates in Test 8 were sparsely distributed, with even more noticeable periods of crack where AE was absent.

The results for Test 9 exhibited some similarities with Test 8 in that there were initial peaks in AE Hit rates at some crack lengths less than 30 mm, some intermittent peaks between 40 mm – 50 mm and then increasing AE Hit

rates with crack growth as the sample approached failure. However there were significantly less AE signals recorded for crack lengths less than 30 mm in Test 9 compared to Test 8 by at least a factor of 15.

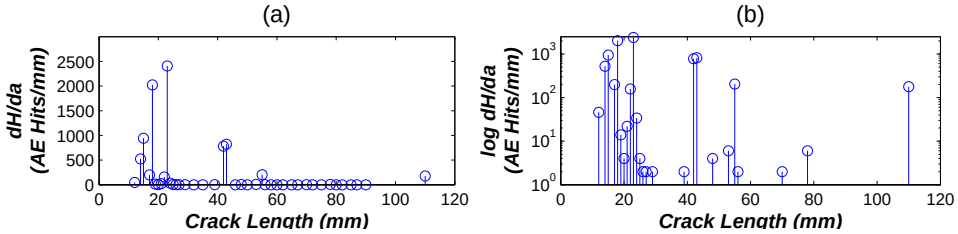

Figure 4.24: AE Hit rate versus crack length for sensors 1 and 2 (Location Group 1) from Test 8 with Stress range of 52.2 MPa and R ratio of 0.1

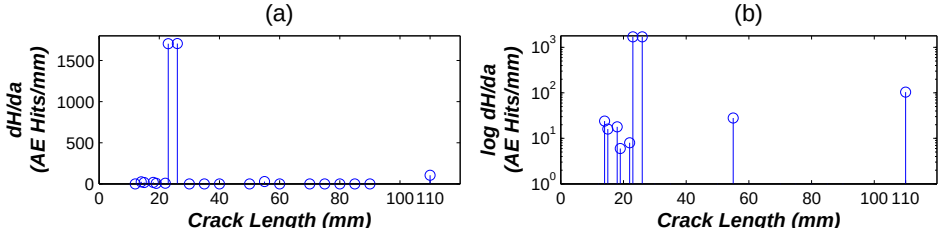

Figure 4.25: AE Hit rate versus crack length for sensors 3 and 4 (Location Group 1) from Test 8 with Stress range of 52.2 MPa and R ratio of 0.1

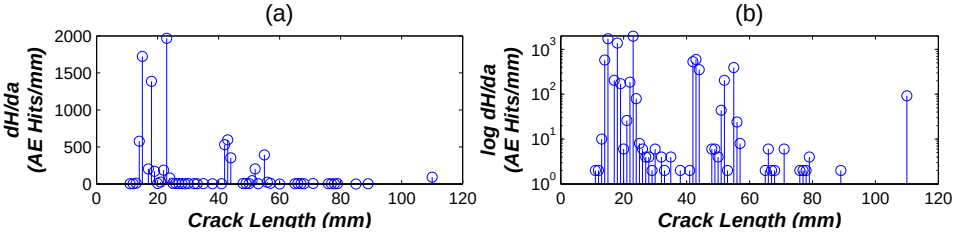

Figure 4.26: AE Hit rate versus crack length for sensors 5 and 6 (Location Group 1) from Test 8 with Stress range of 52.2 MPa and R ratio of 0.1

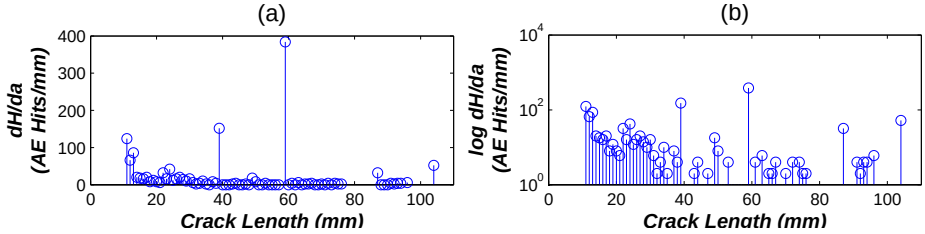

Figure 4.27: AE Hit rate versus crack length for sensors 1 and 2 (Location Group 2) from Test 9 with Stress range of 52.2 MPa and R ratio of 0.1

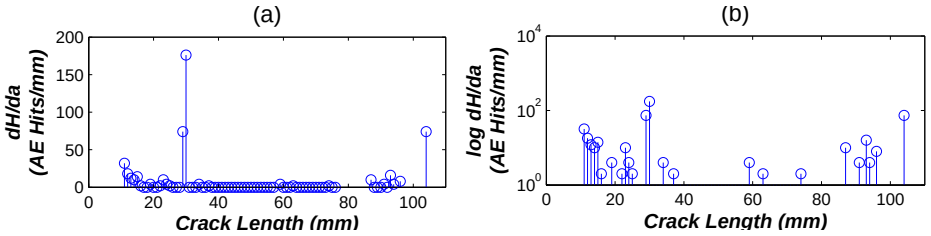

Figure 4.28: AE Hit rate versus crack length for sensors 3 and 4 (Location Group 2) from Test 9 with Stress range of 52.2 MPa and R ratio of 0.1

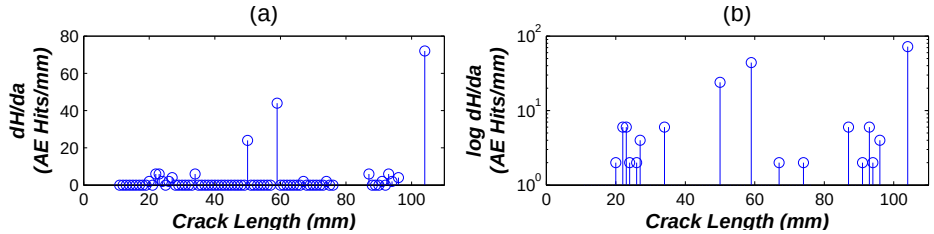

Figure 4.29: AE Hit rate versus crack length for sensors 5 and 6 (Location Group 2) from Test 9 with Stress range of 52.2 MPa and R ratio of 0.1

Effect of increased loading frequency

MT Samples

Test 10 was conducted on an MT sample with an increased loading frequency of 4 Hz. The other test parameters were identical to those used in the Tests 8 and 9. The guard sensor setup for MT samples was used to record AE data with two pairs of sensors as described in Section 3.2.4.2. The results for AE Hit rates at various crack lengths are illustrated in Figure 4-30 and Figure 4-31 for Location Groups 1 and 2 respectively.

It was observed that the trend and values of AE Hit rates were almost identical for both sensor arrays. They were basically characterised by varying peaks of AE Hit rates at crack lengths between 20 mm – 45 mm as well as between 50 mm – 70 mm. In comparison with the results obtained from the Tests 8 and 9, this trend does not appear to bear a direct correlation. Although the maximum peaks in tests were comparable, the AE Hit rates recorded in Test 10 were much more rampant for longer periods of crack growth.

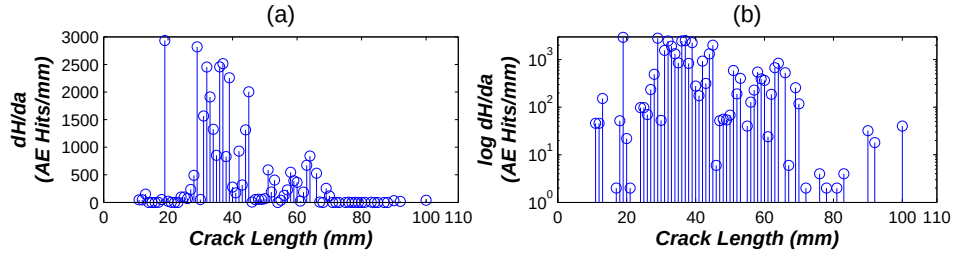

Figure 4.30: AE Hit rate versus crack length for sensors 1 and 2 (Location Group 1) from Test 10 with Stress range of 52.2 MPa, R ratio of 0.1 and frequency of 4 Hz

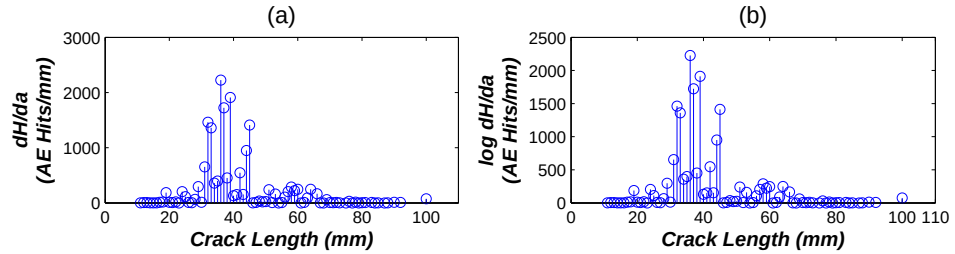

Figure 4.31: AE Hit rate versus crack length for sensors 5 and 6 (Location Group 2) from Test 10 with Stress range of 52.2 MPa, R ratio of 0.1 and frequency of 4 Hz

Effect of reduced stress range

SEN Samples

Test 11 was performed with stress range reduced to 27 MPa, stress ratio of 0.1 and loading frequency of 2 Hz. The Delta T AE sensor setup was used as previously described in Section 3.2.4.1. The test was prematurely ended with crack length at 68 mm. The results for AE Hit rates at various crack lengths are shown in Figure 4-32.

It was observed that there were no AE Hits recorded until a crack length of 14 mm where a transient increase was observed up to 1390 Hits/mm for just 1 mm of crack growth and almost no AE Hits were recorded afterwards until crack lengths between 40 mm and 65 mm where AE Hit rates in excess of 100 Hits/mm were observed. The initial peak was at least 7 times greater than the AE Hit rates observed in other periods of the test.

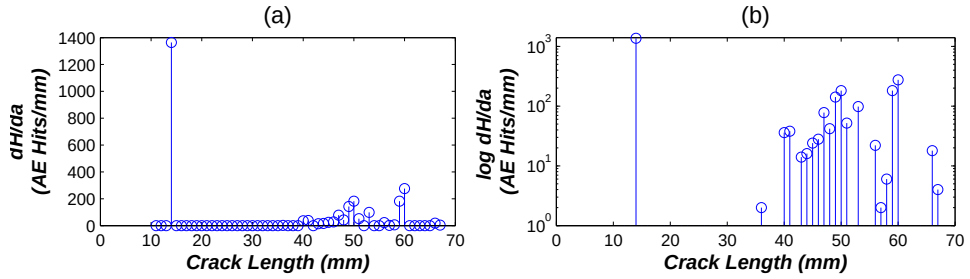

Figure 4.32: AE Hit rate versus crack length from Test 11 with Stress range of 27 MPa, frequency of 2Hz, stress ratio of 0.1 and ΔK values of 5.5 – 19.2 MPa $\sqrt{m}$

Tests 12, 13 and 14 were also performed on SEN samples with a stress range of 27 MPa and stress ratio of 0.1 but with loading frequency of 4 Hz as outlined in Table 4-2. All the samples were tested until failure which occurred at crack lengths of about 150 mm. Plots of crack length against elapsed cycles are shown in Appendix A. The guard sensor AE sensor setup for SEN samples was used in all of these tests as described in Section 3.2.4.2.

The results of AE Hit rates at various crack lengths for Test 12 are shown in Figure 4-33 for Location Group 1, which were the pair of sensors close to the edge of the test sample and Figure 4-34 for Location Group 2 which was located in the middle of the test sample. Correlating the results for Location Group 1 to that obtained for the average AE Hits rates observed in Tests 1 to 7, illustrated in Figure 4-21, some similarities particular to Stages 1, 3 and 4 can be seen. Stage 1 corresponds to the rise to peak and decline of AE Hit rates observed for crack growth up to a crack length of 30 mm, while Stage 3 corresponds to the second rise to peak and decline between crack lengths of 30 mm and 90 mm. Stage 4 corresponds to the steady increase in AE Hit rates with increased crack growth as the sample approached failure. Although there was also a decline in AE Hit rates after an initial peak like the Stage 2 shown in Figure 4-21, this did not appear to reach minimal values in the case of Test 12 and did not occur for prolong periods as previously observed.

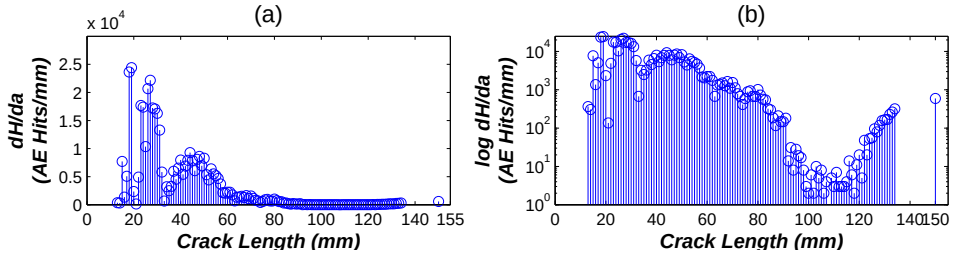

Figure 4.33: AE Hit rate versus crack length from Test 12 (sensors 1 and 2 – Location Group 1) with Stress range of 27 MPa, frequency of 4Hz, stress ratio of 0.1 and ΔK values of 5.5 – 76.8 MPa $\sqrt{m}$

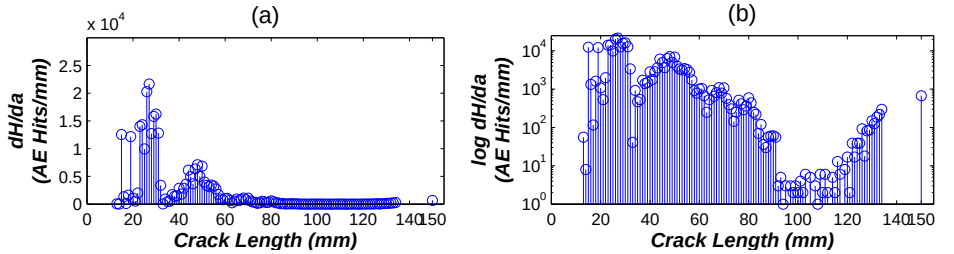

Figure 4.34: AE Hit rate versus crack length from Test 12 (sensors 5 and 6 – Location Group 2) with Stress range of 27 MPa, frequency of 4Hz, stress ratio of 0.1 and ΔK values of 5.5 – 76.8 MPa $\sqrt{m}$

For Location Group 2, the trend AE Hit rates at all crack lengths were almost identical to those observed in Location Group 1, although the values of AE Hits rates at crack lengths between 35 mm and 60 mm were marginally less by a factor of 1.8. In comparison to the average AE Hit rates of Tests 1 to 7 significantly more AE Hit rates were observed at all crack lengths for both Location Groups 1 and 2, particularly at the peak in Stage 1 where they were at least 12 times greater.

The AE Hit rates results for Tests 13 and 14 are illustrated in Figures Figure 4-35, Figure 4-36, Figure 4-37 and Figure 4-38 for each pair of the sensor arrays. In these tests both Location Groups 1 and 2 showed trends similar to each other with the largest variation seen at crack lengths less than 20 mm where Hit rates varied at most by a factor of 2.9. These were also similar to Stages 1, 3 and 4 of the average AE Hit rates obtained for Tests 1 to 7 as described earlier.

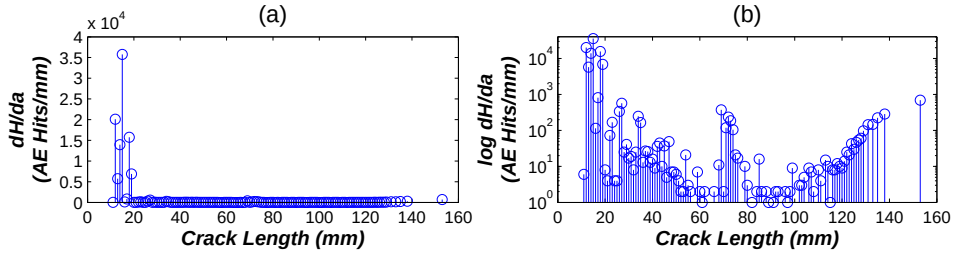

Figure 4.35: AE Hit rate versus crack length from Test 13 (sensors 1 and 2 – Location Group 1) with Stress range of 27 MPa, frequency of 4Hz, stress ratio of 0.1 and ΔK values of 5.5 – 74.1 MPa $\sqrt{m}$

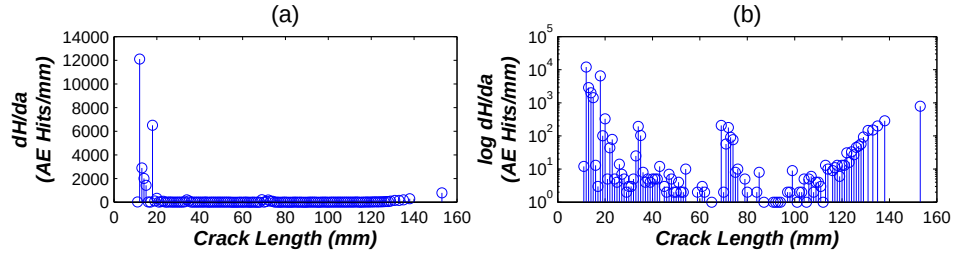

Figure 4.36: AE Hit rate versus crack length from Test 13 (sensors 1 and 2 – Location Group 2) with Stress range of 27 MPa, frequency of 4Hz, stress ratio of 0.1 and ΔK values of 5.5 – 74.1 MPa $\sqrt{m}$

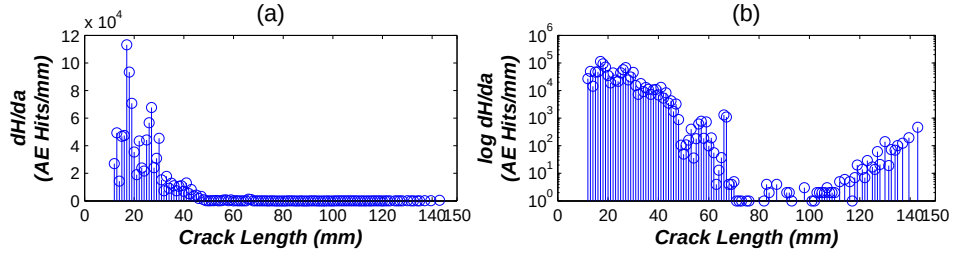

Figure 4.37: AE Hit rate versus crack length from Test 14 (sensors 1 and 2 – Location Group 1) with Stress range of 27 MPa, frequency of 4Hz, stress ratio of 0.1 and ΔK values of 5.5 – 70 MPa $\sqrt{m}$

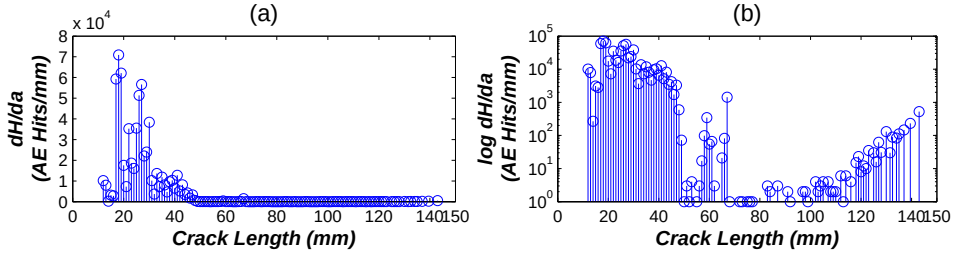

Figure 4.38: AE Hit rate versus crack length from Test 14 (sensors 5 and 6 – Location Group 2) with Stress range of 27 MPa, frequency of 4Hz, stress ratio of 0.1 and ΔK values of 5.5 – 70 MPa $\sqrt{m}$

MT Samples

Test 15 was conducted on an MT test sample also with a reduced stress range of 27 MPa, stress ratio of 0.1 and loading frequency of 4 Hz. The guard sensor setup was also used to record AE data and the results for AE Hit rates at various crack lengths are illustrated in Figure 4-39 and Figure 4-40 for Location Groups 1 and 2 respectively. It is observed that both sets of results are almost identical with the largest variation seen at crack lengths less than 20 mm where Hit rates varied at most by a factor of 1.3. The results were characterised by very high AE Hit rates up to 14000 Hits/mm for crack growth up to 20 mm and then minimal Hit rates around 50 Hits/mm for subsequent crack growth until the period approaching failure where an increase up to 3800 Hits/mm was observed.

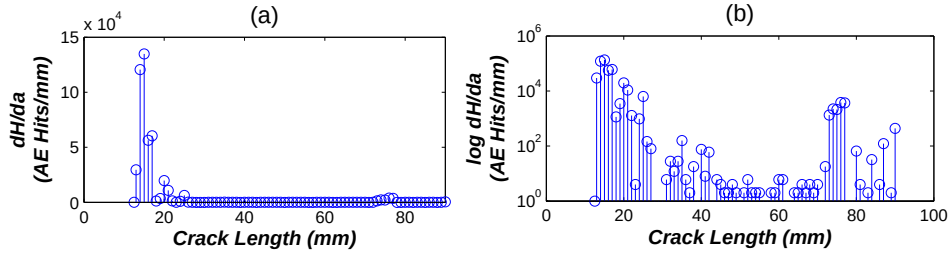

Figure 4.39: AE Hit rate versus crack length for sensors 1 and 2 from Test 15 with Stress range of 27 MPa, R ratio of 0.1 and frequency of 4 Hz

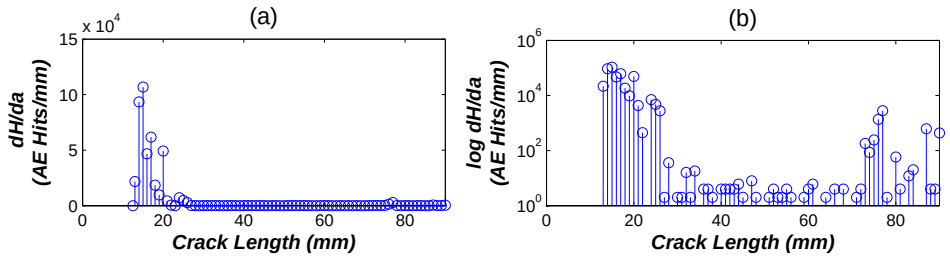

Figure 4.40: AE Hit rate versus crack length for sensors 5 and 6 from Test 15 with Stress range of 27 MPa, R ratio of 0.1 and frequency of 4 Hz

The peak Hit rate in this test was observed at crack lengths less than 30 mm like in most of the previous tests reported. However, in comparison, it was about 5 times greater than maximum AE Hit rate in the tests on SEN samples with identical loading conditions.

Effect of increased mean stress

SEN Samples

Test 16 was performed on an SEN test sample with stress range of 52.2 MPa and stress ratio increased to 0.5. The loading frequency was 2 Hz and the sample was fatigue tested until failure which occurred at a crack length of about 87 mm. The Guard Sensor setup was to monitor AE signals generated from the fatigue crack, as described in Section 3.2.4.2, and the results for the AE Hit rates per mm are given in Figure 4-41 and Figure 4-42 for Location Groups 1 and 2 respectively. It is observed that the Hit rates for Location Group 1 showed similarities to Stages 1 and 4 of the average AE Hit rates in Tests 1 to 7 as previously described. This was not obvious on the linear scale, particularly for Stage 1, as the peak values of Hit rates were around 10 Hits/mm, over 200 times smaller than the average Hit rates for Tests 1 to 7 at similar crack lengths as shown in Figure 4-21. Minimal AE Hit rates were observed between crack lengths of about 25 mm and 70 mm, although a very short-lived spike of about 100 Hits/mm was observed at crack lengths around 40 mm.

An almost identical trend was observed for Location Group 2 with the exception of a rise to peak of about 1000 Hits/mm and then a decline down to about 10 Hits/mm observed between 38 mm to 50 mm which akin to Stage 3 in the average AE Hits/mm of Tests 1 to 7 as previously described.

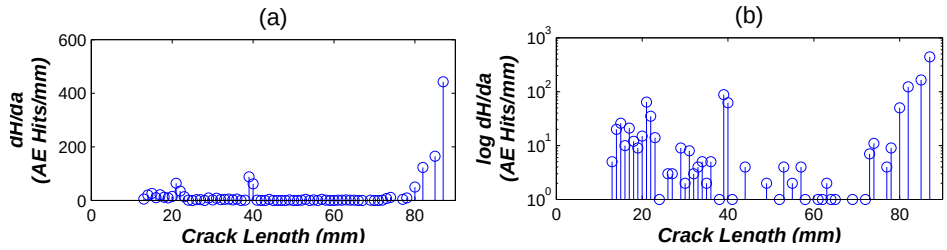

Figure 4.41: AE Hit rate versus crack length for sensors 1 and 2 (Location Group 1) from Test 16 with Stress range of 27 MPa and R ratio of 0.5 ΔK values of 6.0 – 26.1 MPa $\sqrt{m}$

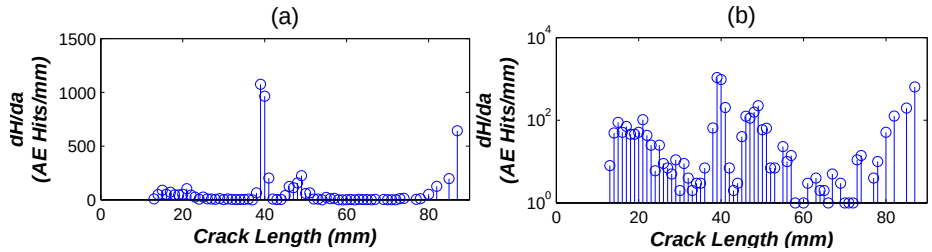

Figure 4.42: AE Hit rate versus crack length for sensors 5 and 6 (Location Group 2) from Test 16 with Stress range of 27 MPa and R ratio of 0.5 ΔK values of 6.0 – 26.1 MPa $\sqrt{m}$

Effect of stress intensity range

Test 17 was performed on an SEN sample using quasi-constant stress intensity range of 12.1 MPa $\sqrt{m}$ at every length of crack growth as Test 17 was performed on an SEN sample using a quasi-constant stress described in Section 3.2.2. The Delta T setup as described in Section 3.2 was used in recording the AE signals generated during the test. The results in terms of AE Hit rates at various crack lengths are shown in Figure 4-43. They are characterised by AE Hit rates less than 100 Hits/mm for growth up to a crack length of 42 mm where a rapid increase with a peak of 18,000 Hits/mm. A rapid decline was also observed at a crack length of 46 mm. Intermittent peaks were seen around 52 mm and 62 mm with minimal rates at other crack lengths.

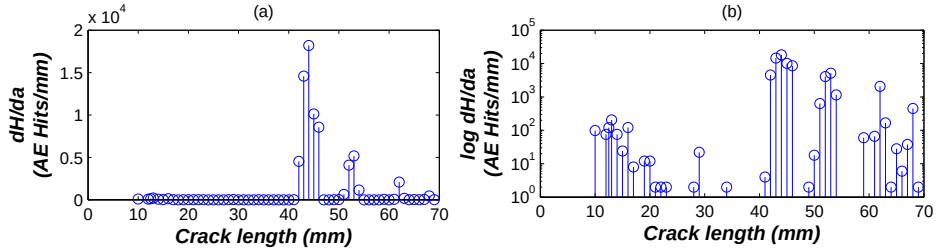

Figure 4.43: AE Hit rate versus crack length for Test 15 performed with quasi-constant ΔK

Effect of variable amplitude loading

Test 18 was performed on an SEN sample using the variable amplitude loading spectrum as described in Section 3.2.2. A total of 323 sequences were run over 21 days and failure occurred at crack lengths of about 120 mm. The Guard Sensor setup was used to monitor the AE signals generated from the

fatigue crack and the results of AE Hit rates at various crack lengths are shown in Figure 4-44 and Figure 4-45 for Location Groups 1 and 2 respectively. Both results are almost identical and are characterised by low quasi-constant rates of AE for the majority of crack growth and an increase at crack lengths approaching sample failure.

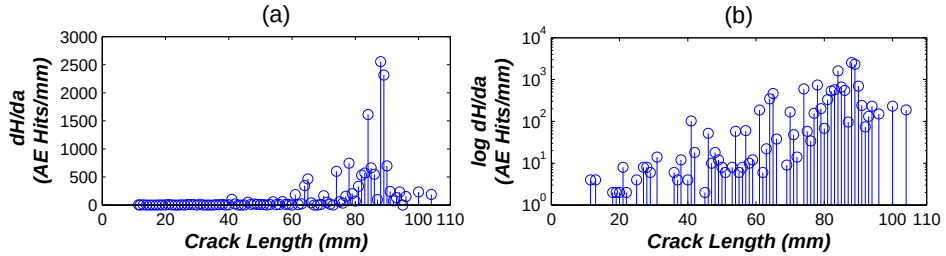

Figure 4.44: AE Hit rate versus crack length for sensors 1 and 2 (Location Group 1) from Test 18 with sample under variable amplitude loading

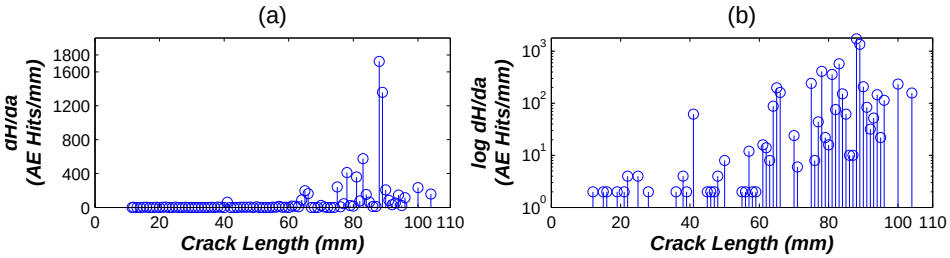

Figure 4.45: AE Hit rate versus crack length for sensors 5 and 6 (Location Group 2) from Test 18 with sample under variable amplitude loading

4.4.2 Metric 2 – AE distribution with applied load cycles

The values of load applied to the test samples were monitored by the AE system as described in Section 3.2.4. The AE signals recorded were correlated with their corresponding values of applied cyclic load and these were plotted for the various crack lengths recorded. The distribution of these load values at various crack lengths was represented using the Kernel Density Estimation (KDE) method [65] as described in Section 2.4.3.3. This gives a visual illustration of the trend of AE generation from fatigue crack at various stages of growth.

Effect of variation in material batch

Batch 1 material

The results of AE distribution with the applied load cycles at various crack lengths for Tests 1 to 3 on Batch 1 material are illustrated in Figure 4-46, Figure 4-47 and Figure 4-48 respectively. It is observed that the initial peak in AE hit rates seen in Figure 4-14, Figure 4-15 and Figure 4-16 occurred in the middle to lower portion of the loading cycles and the resurgence of AE signals at crack lengths between 55 mm and 70 mm occurred close to the minimum of the loading cycles. Furthermore, the AE signals recorded as the sample approached failure occurred mainly around the mean stress as well as close to the maximum of the loading and just before final failure appeared to occur across most regions of the loading range.

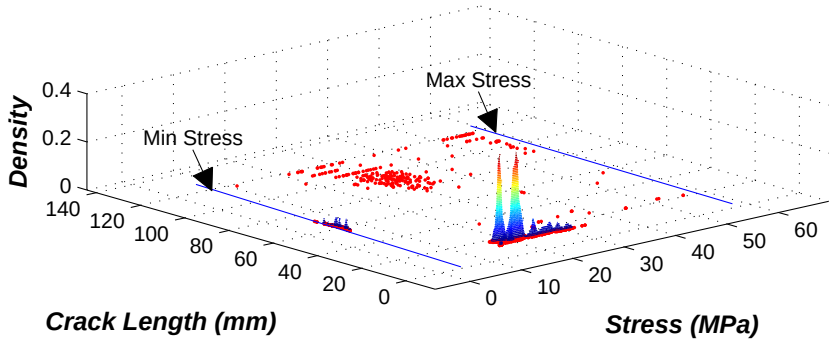

Figure 4.46: AE Hit distribution with applied load at various crack lengths for Test 1 with Stress range of 52.2 MPa and R ratio of 0.1

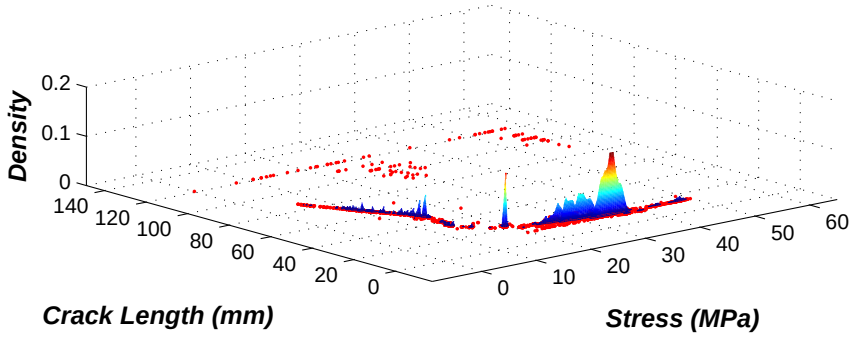

Figure 4.47: AE Hit distribution with applied load at various crack lengths for Test 2 with Stress range of 52.2 MPa and R ratio of 0.1

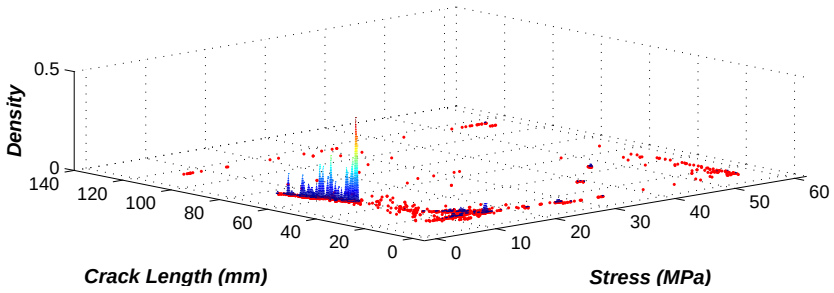

Figure 4.48: AE Hit distribution with applied load at various crack lengths for Test 3 with Stress range of 52.2 MPa and R ratio of 0.1

Batch 2 material

Despite the differences in the AE Hit rates for Tests 4 and 5, shown in Figure 4-17 and Figure 4-18 in terms of AE Hit rates, from Batch 2 material compared with those from the Batch 1 material, there were some similarities in terms of the recorded AE signal distribution with the applied load cycles at various crack lengths. The results for Tests 4 and 5 are illustrated in Figure 4-49 and Figure 4-50 respectively. It was observed that AE signals occurred around the mean stress as well as close to the maximum of the loading cycles and just before final failure they appeared to occur across most regions of the loading range just as observed in Tests 1 to 3.

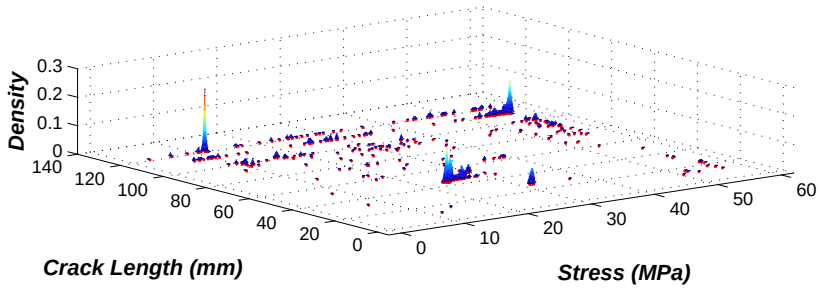

Figure 4.49: AE Hit distribution with applied load at various crack lengths for Test 4 with Stress range of 52.2 MPa and R ratio of 0.1

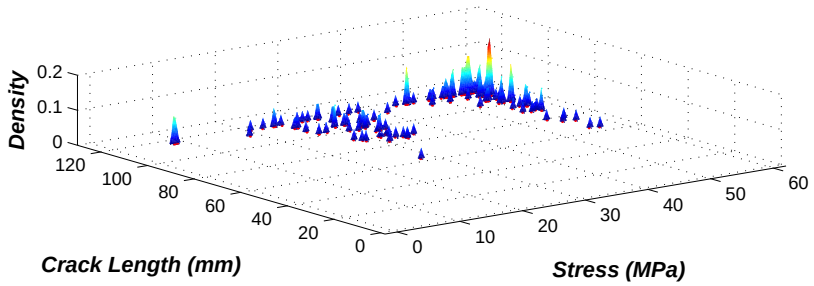

Figure 4.50: AE Hit distribution with applied load at various crack lengths for Test 5 with Stress range of 52.2 MPa and R ratio of 0.1

Batch 3 material

The results for Tests 6 and 7 are illustrated in Figure 4-51 and Figure 4-52 respectively. Both results exhibited similarities to the previous test in that AE Hits were observed close to the maximum of the loading range for periods of crack growth, particularly at the early stages and in the period approaching failure. Also, the AE Hits were seen to occur almost across the entire loading range at sample failure with a concentration of AE Hits around the mean stress in the period leading up to failure. At crack lengths between 45 mm and 70 mm where there was a rise to peak and then decline in AE Hit rates, as illustrated in Figure 4-19 and Figure 4-20, AE Hits were observed to have occurred in the bottom half of the loading cycles as previously reported for Tests 1 – 3 on Batch 1 material.

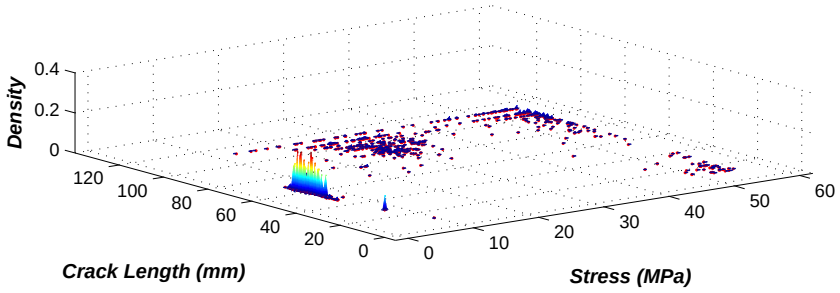

Figure 4.51: AE Hit distribution with applied load at various crack lengths for Test 6 with Stress range of 52.2 MPa and R ratio of 0.1

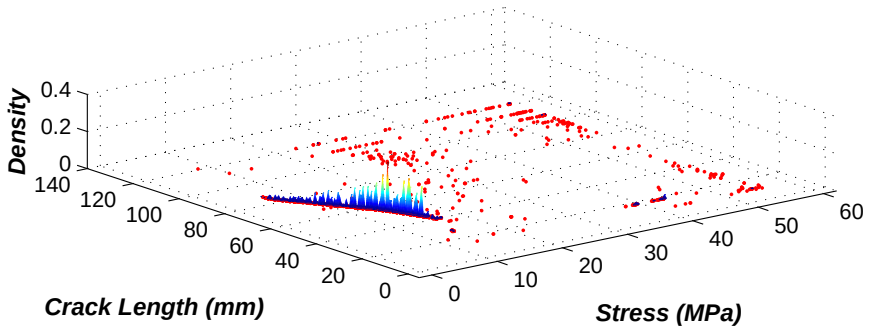

Figure 4.52: AE Hit distribution with applied load at various crack lengths for Test 7 with Stress range of 52.2 MPa and R ratio of 0.1

The data of cyclic load values at various crack lengths for Tests 1 – 7 were added together to identify characteristic behaviour. The distribution of cyclic loads at each crack length was again determined using the Kernel Density Estimation (KDE) method and the results are shown in Figure 4-53. Four significant trends can be identified as follows:

1. **Trend 1:** At early crack lengths AE is observed to occur around the mean stress but subsequently occurred at lower loads with increasing crack length until a crack length of about 75 mm. The highest rates of AE are also observed in this region.

2. **Trend 2:** AE occurred close to the maximum of the loading range for periods of crack growth, particularly at the early stages and just before failure.

3. **Trend 3:** A concentration of AE occurred around the middle of the loading range with the sample approaching failure.

4. **Trend 4:** At the failure crack length AE appears to be spread across the loading range.

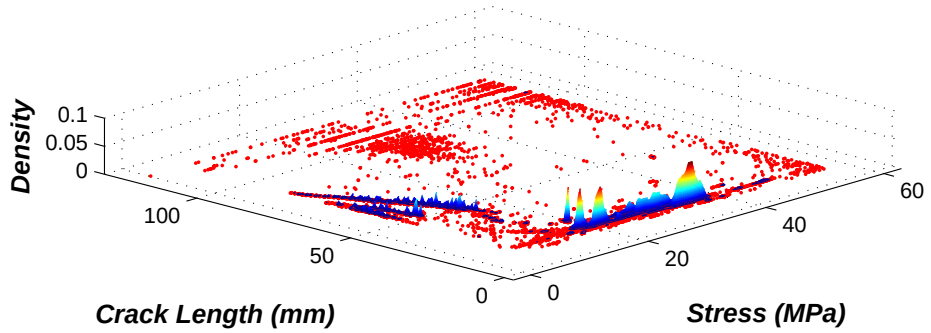

Figure 4.53: AE Hit distribution with applied load at various crack lengths for Tests 1 – 7 with Stress range of 52.2 MPa and R ratio of 0.1

Comparing the result in Figure 4-53 to the average AE Hit rates at similar crack lengths illustrated in Figure 4-21, it can be observed that the initial peak up to 1600 Hits/mm and decline to about 20 Hits/mm in AE Hit rates at crack lengths less than 20 mm (Stage 1) occurred in the mid quarters of the loading range. For Stage 2 between crack lengths of 20 – 50 mm with minimal AE Hit rates less than 30 Hits/mm, AE signals can be seen to occur in the lower third of the loading range as well as close to the maximum stress. In Stage 3 where there was another increase and then decrease in AE Hit rates between crack lengths of 55 – 70 mm, the AE signals occurred mainly in the lower third of the loading range with even further decreasing values of load with increased crack length, although AE signals could also be seen to occur close to the maximum of the loading range. Stage 4 constitutes AE signals occurring around the mean stress as well as close to the maximum stress between crack lengths of 80 – 100 mm, after which they appeared across the loading range.

Effect of sample geometry

The results for Tests 8 and 9 are shown in Figure 4-54 to Figure 4-56 and Figure 4-57 to Figure 4-59 respectively for the different location groups. Test 8 was characterised by AE Hits occurring almost entirelyacross the loading range at crack lengths less than 40 mm as well as AE Hits were occurring around the maximum and minimum of the loading range with the highest peaks in AE activity observed towards the bottom of the loading cycles. These bear some similarities with Tests 1 – 7 as previously described, however the most significant difference was in the AE Hits occurring around the mean stress at crack lengths approaching sample failure which were absent in the tests on MT samples.

The AE Hit rates for Test 9 were significantly less than those recorded for Test 8 at similar crack lengths, as previously described, however similarities can be seen in AE Hits occurring across the loading range at crack lengths just before final failure. Noticeable comparisons with Tests 1 – 7 can also be made in the AE Hits occurring close to the maximum of the loading cycles for periods of crack growth.

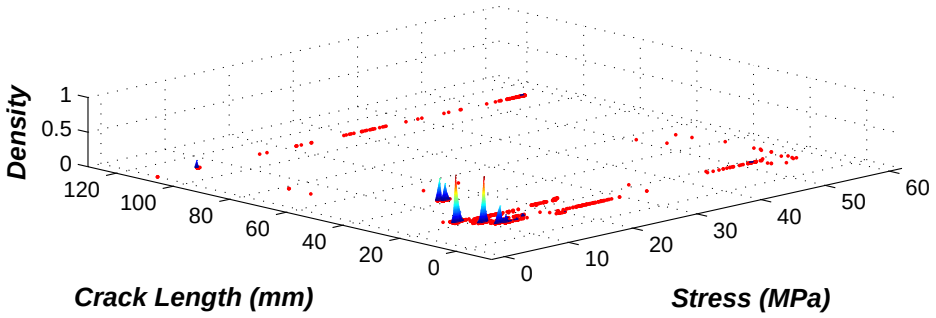

Figure 4.54: AE Hit distribution with applied load at various crack lengths for sensors 1 and 2 in Test 8 with Stress range of 52.2 MPa and R ratio of 0.1

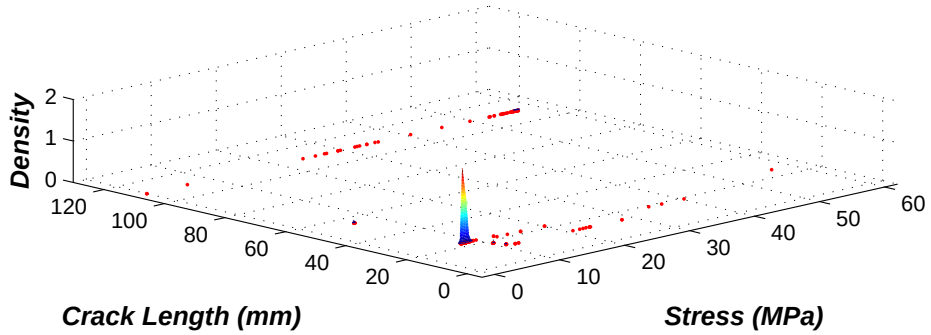

Figure 4.55: AE Hit distribution with applied load at various crack lengths for sensors 3 and 4 in Test 8 with Stress range of 52.2 MPa and R ratio of 0.1

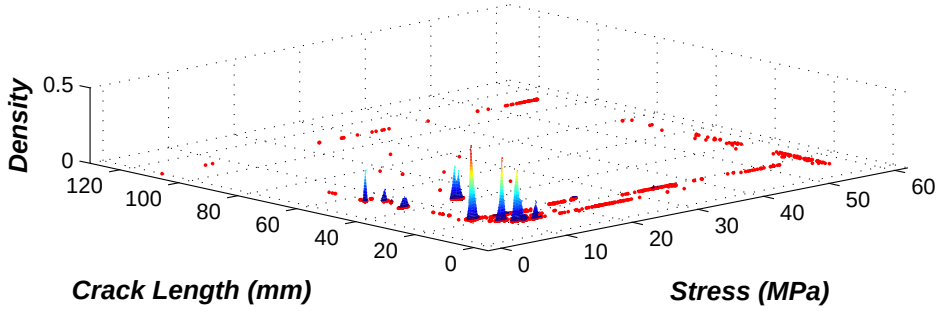

Figure 4.56: AE Hit distribution with applied load at various crack lengths for sensors 5 and 6 in Test 8 with Stress range of 52.2 MPa and R ratio of 0.1

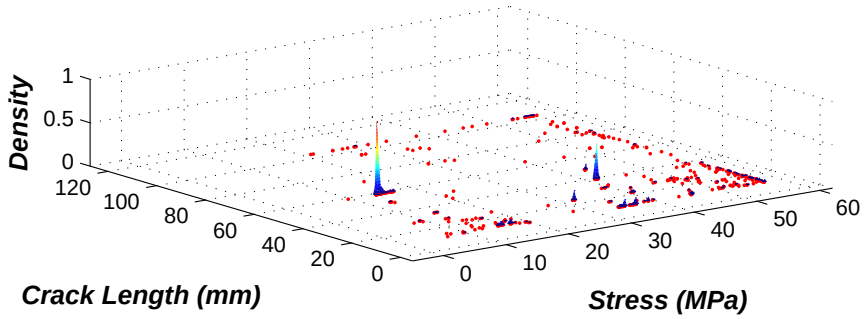

Figure 4.57: AE Hit distribution with applied load at various crack lengths for sensors 1 and 2 in Test 9 with Stress range of 52.2 MPa and R ratio of 0.1

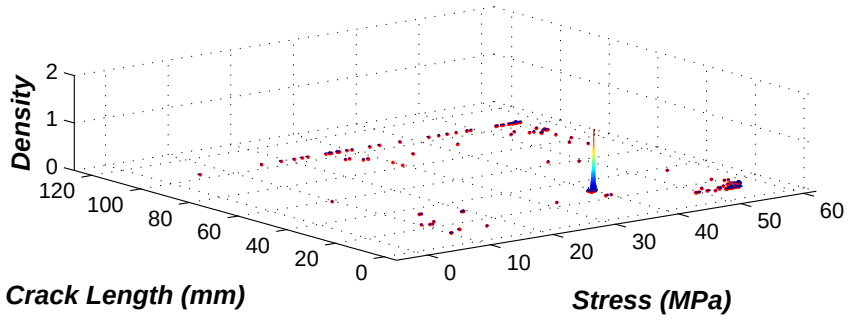

Figure 4.58: AE Hit distribution with applied load at various crack lengths for sensors 3 and 4 in Test 9 with Stress range of 52.2 MPa and R ratio of 0.1

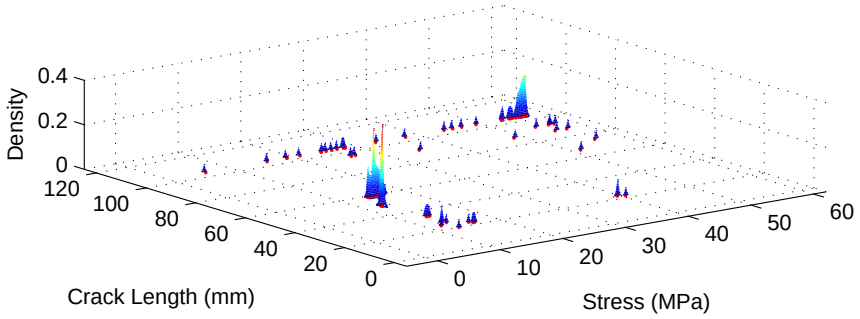

Figure 4.59: AE Hit distribution with applied load at various crack lengths for sensors 5 and 6 in Test 9 with Stress range of 52.2 MPa and R ratio of 0.1

Effect of increased loading frequency

MT Samples

The result of Test 10 which was performed on an MT sample with increased loading frequency of 4 Hz is shown in Figure 4-60 and Figure 4-61 for Location

Groups 1 and 2 respectively. It was observed that at particular crack lengths less than 40 mm AE Hits occurred almost across the entire loading range with the highest peaks in AE activity seen towards the bottom of the loading cycles in both plots. Also, AE Hits occurred close to the maximum of the loading cycles for periods of crack growth as well as across the loading range at crack lengths just before final failure. These trends are similar to those observed in the Tests 8 and 9.

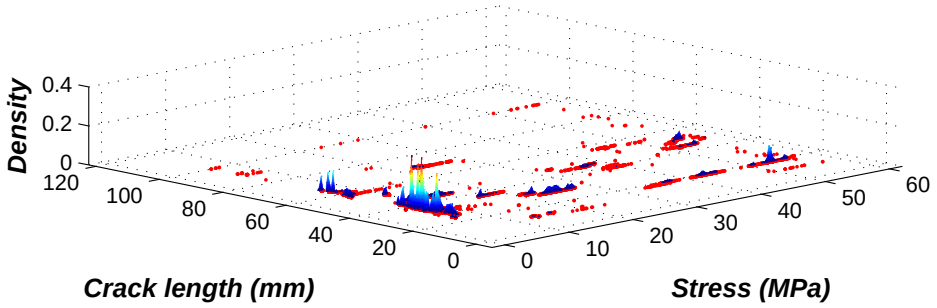

Figure 4.60: AE Hit distribution with applied load at various crack lengths for sensors 1 and 2 in Test 10 with Stress range of 52.2 MPa, R ratio of 0.1 and frequency of 4 Hz

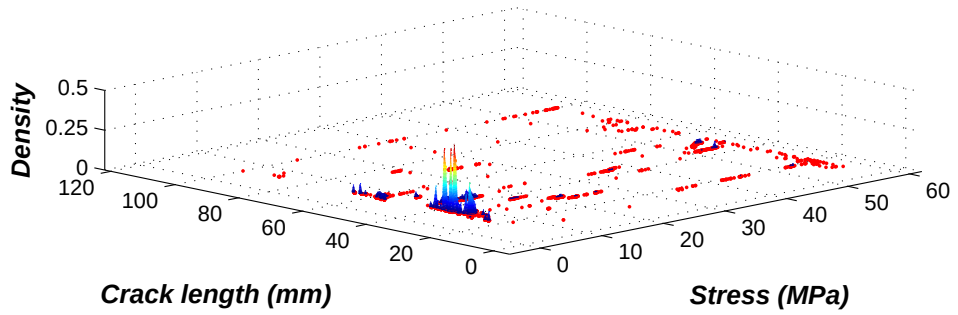

Figure 4.61: AE Hit distribution with applied load at various crack lengths for sensors 5 and 6 in Test 10 with Stress range of 52.2 MPa, R ratio of 0.1 and frequency of 4 Hz

Effect of Reduced Stress Range

SEN Samples

The result of AE Hits distribution with applied load cycles at various crack lengths for Test 11 is shown in Figure 4-62. It can be seen that for the extent of crack growth during the test the distribution was similar to Trend I observed in Tests 1 – 7 with stress range of 52.2 MPa, where the initial peak in AE

Hit rates at early crack lengths occurred in the middle to lower portions of the loading cycles and then decreased with crack growth until a crack length of about 75 mm. The major difference however was that there was a marked absence of AE Hits between crack lengths of about 16 mm and 35 mm.

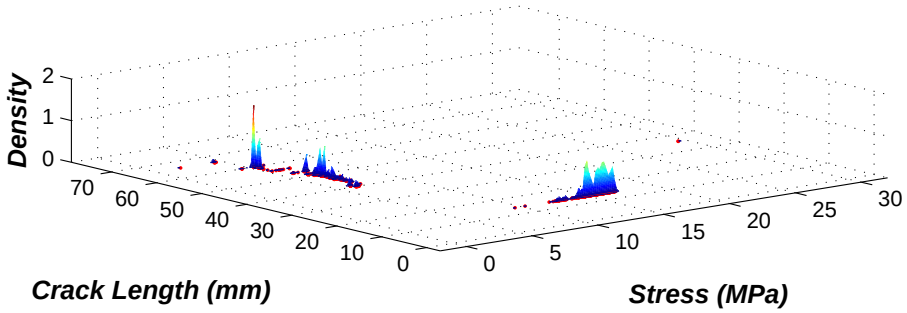

Figure 4.62: AE Hit distribution with applied load at various crack lengths for Test 11 with Stress range of 27 MPa and R ratio of 0.1

The results of AE Hits distribution with applied load cycles at various crack lengths for both Location Groups are illustrated in Figure 4-63 to Figure 4-64 for Test 12, Figure 4-65 to Figure 4-66 for Test 13 and Figure 4-67 to Figure 4-68 for Test 14. The results appear almost identical; exhibiting all the characteristics observed in Tests 1 to 7 as previously described but was more evident in comparison.

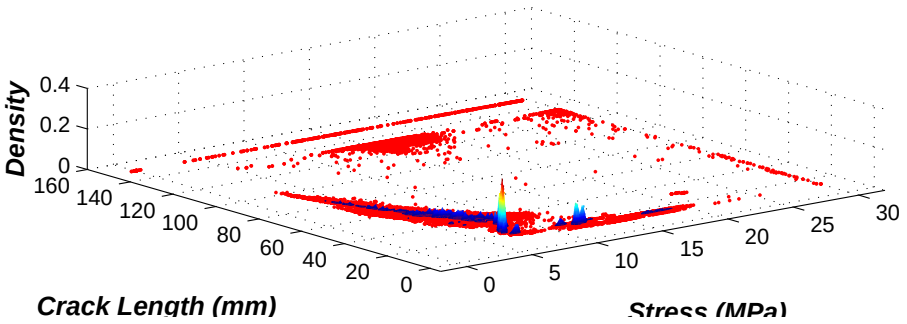

Figure 4.63: AE Hit distribution with applied load at various crack lengths for sensors 1 and 2 in Test 12 with Stress range of 27 MPa and R ratio of 0.1

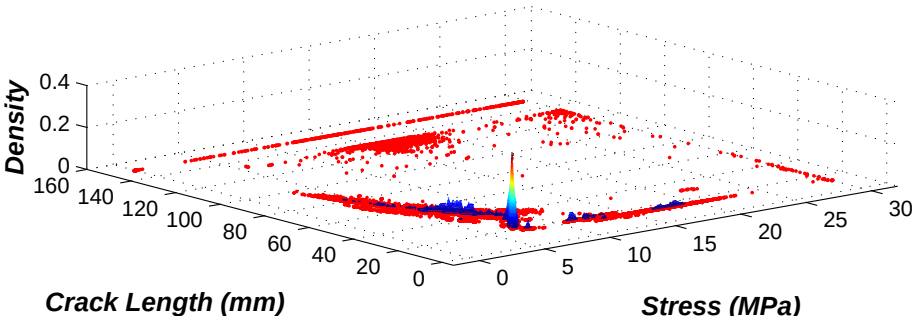

Figure 4.64: AE Hit distribution with applied load at various crack lengths for sensors 5 and 6 in Test 12 with Stress range of 27 MPa and R ratio of 0.1

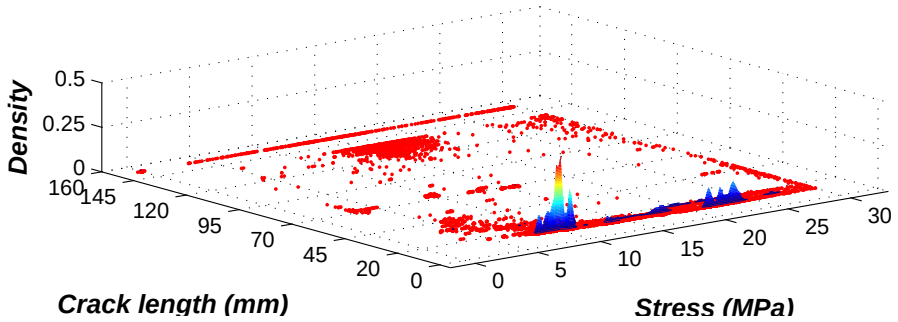

Figure 4.65: AE Hit distribution with applied load at various crack lengths for sensors 1 and 2 in Test 13 with Stress range of 27 MPa and R ratio of 0.1

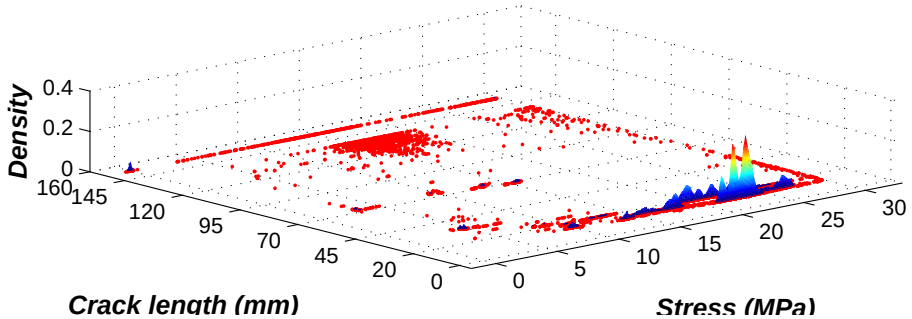

Figure 4.66: AE Hit distribution with applied load at various crack lengths for sensors 5 and 6 in Test 13 with Stress range of 27 MPa and R ratio of 0.1

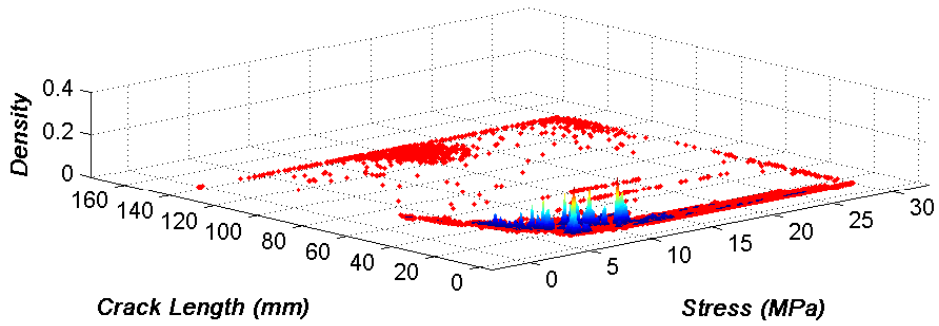

Figure 4.67: AE Hit distribution with applied load at various crack lengths for sensors 1 and 2 in Test 14 with Stress range of 27 MPa and R ratio of 0.1

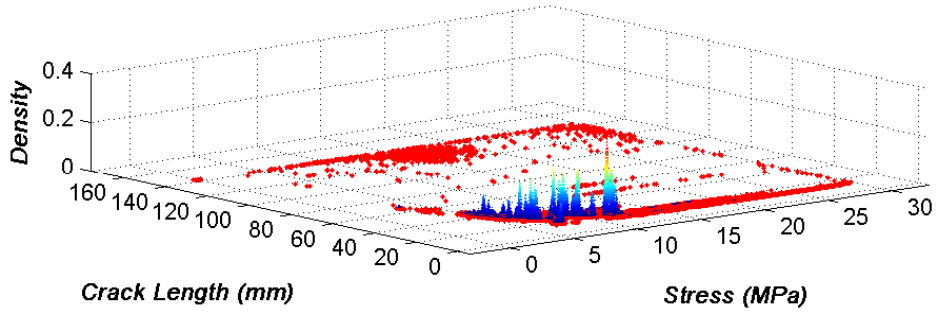

Figure 4.68: AE Hit distribution with applied load at various crack lengths for sensors 5 and 6 in Test 14 with Stress range of 27 MPa and R ratio of 0.1

MT Samples

The results of AE Hit distribution with applied load at various crack lengths for Test 15 are shown in Figure 4-68 and Figure 6-69 for Location Groups 1 and 2 respectively. Both plots are almost identical and trends observed are quite similar to other tests conducted on MT samples but they are much more pronounced because of the larger amount of AE Hit rates recorded in the test.

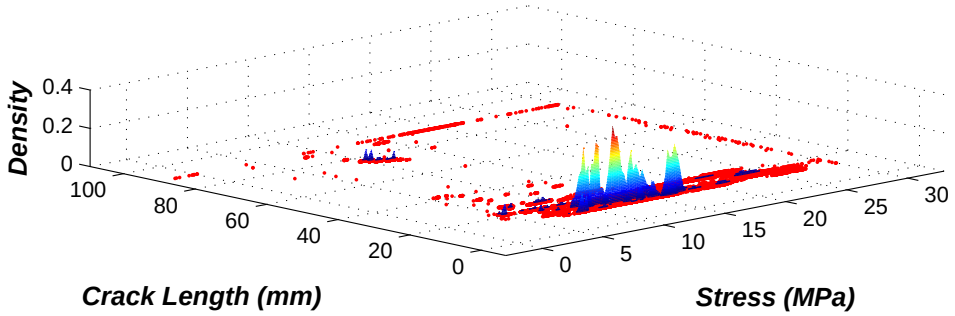

Figure 4.69: AE Hit distribution with applied load at various crack lengths for sensors 1 and 2 in Test 15 with Stress range of 27 MPa, R ratio of 0.1 and frequency of 4 Hz

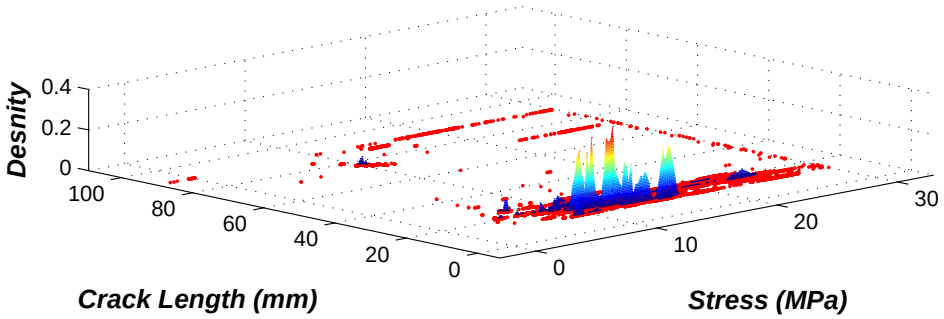

Figure 4.70: AE Hit distribution with applied load at various crack lengths for sensors 5 and 6 in Test 15 with Stress range of 27 MPa, R ratio of 0.1 and frequency of 4 Hz

Effect of increased mean stress

SEN Samples

The results of AE Hit distribution with applied load at various crack lengths for Test 16 are shown in Figure 4-71 and Figure 4-72 for Location Groups 1 and 2 respectively. It is observed that both sets of results were very similar, characterised by AE Hits occurring exclusively at the maximum of the loading cycles for the majority of crack propagation and then across the loading rang as the test sample approached failure. These observations are similar to Trends 1 and 4 as previously described. The peak seen at the failure crack length in both data sets occurred well below the minimum Stress which is not necessarily true. This can be attributed to the failsafe mechanism of the test machine triggered at times of test sample failure where the actuator is completely disengaged and in situations where AE Hits are still being recorded when this function is triggered they are hence correlated with the minimum load.

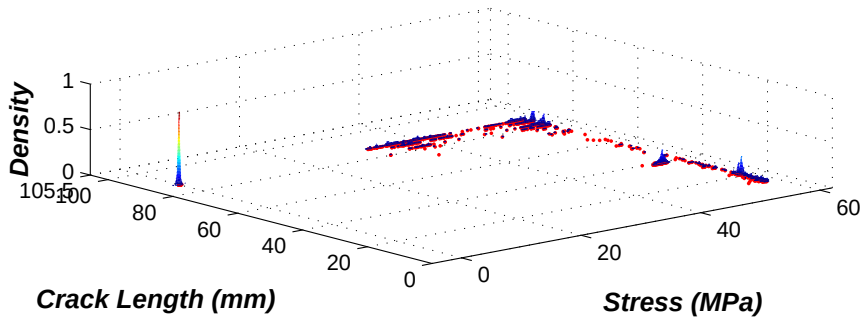

Figure 4.71: AE Hit distribution with applied load at various crack lengths for sensors 1 and 2 in Test 16 with Stress range of 27 MPa and R ratio of 0.5

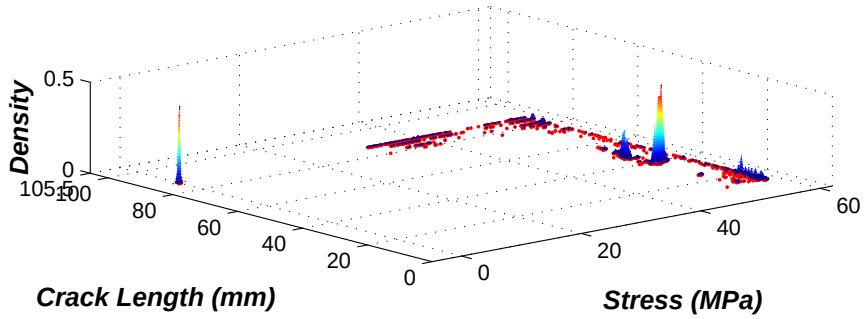

Figure 4.72: AE Hit distribution with applied load at various crack lengths for sensors 5 and 6 in Test 16 with Stress range of 27 MPa and R ratio of 0.5

Effect of stress intensity range

The results of AE Hits distribution with applied load for Test 17 are shown in Figure 4-73 with the load measurements normalised to the maximum cyclic load for each stress range considered at the various crack lengths. It can be seen that AE signals occurred close to the maximum and minimum of the normalised stress range. At a total crack length of 42 mm AE signals were seen to occur almost across the entire normalised stress range, with the greatest densities observed in the bottom where all subsequent Hits were also recorded.

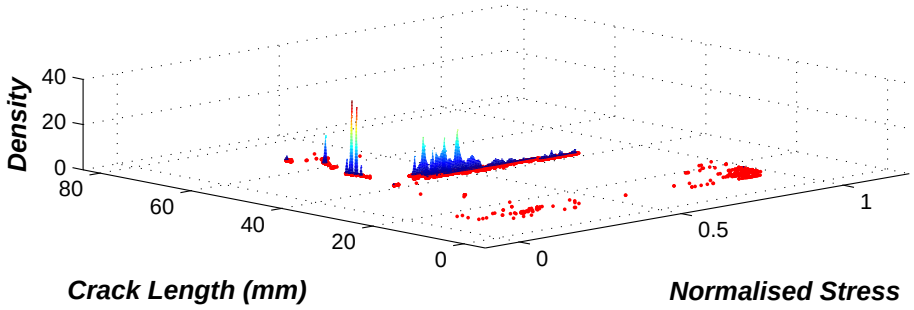

Figure 4.73: AE Hit distribution with applied load at various crack lengths in Test 17 performed with quasi-constant ΔK

Effect of variable amplitude loading

The results of the distribution of AE signals with load for Location Groups 1 and 2 are illustrated in Figure 4-71 and Figure 4-72 respectively for Test 18. Both sensor arrays exhibit similar characteristics. It is observed that AE signals mainly occurred at the maximum peak loads in the spectrum almost throughout the test as well as the lower third of the maximum loading range

for the towards sample failure where the majority of AE signals were observed. This bears some similarities with Trends 1 and 3 as observed in the constant amplitude tests of SEN samples with maximum stress of 58 MPa in Section 4.3.1.1.

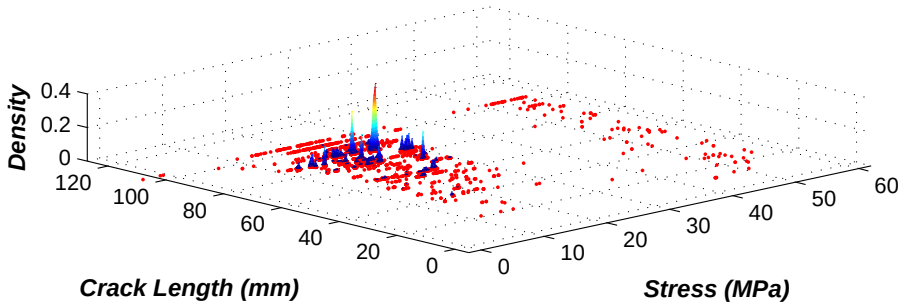

Figure 4.74: AE Hit distribution with applied load at various crack lengths for sensors 1 and 2 in Test 18 with sample under constant amplitude loading

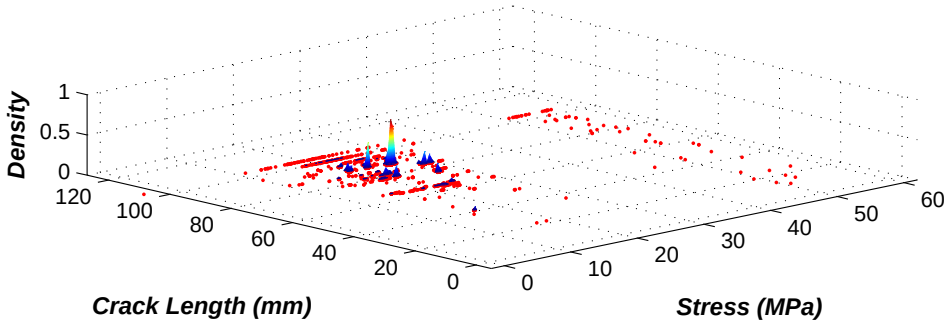

Figure 4.75: AE Hit distribution with applied load at various crack lengths for sensors 5 and 6 in Test 18 with sample under constant amplitude loading

4.4.3 Metric 3 – Probability of Hit (POH)

This is the probability point estimate of successful detection of AE signals generated from a particular fatigue crack length over several observations from different test samples with sensors positioned at a fixed location. This approach is similar to the Hit/miss model for generating POD curves used to asses manual NDT techniques where binary indications of damage are derived based on predefined signal response levels [89]. However, in this case binary indicators of success and failure of crack detection were used with the criteria for successful detection defined as the sensors receiving a number of AE signals (Hits) which exceed an assumed threshold. Values for POH were derived using the expression in Equation 4.5.

$$POH_i = \frac{m(h)_i}{n}, \cap h > T \tag{4.5}$$

Where,

h - *Number of hits*
T - *Threshold for succesful detection*
m - *Number of succesful detections* i - *Crack length*
n - *Number of samples*

After the POH values were calculated for various crack lengths the resulting trend was represented with a best-fit Fourier series model using the curve fitting toolbox in MATLAB.

SEN Samples

POH values were determined at various crack lengths using Equation 4-5 and assuming a detection threshold (T) of 1 hit/mm of crack growth in Tests 1 – 7 performed on SEN samples with a stress range of 52.2 MPa. This was performed using the Fourier series model with an R-squared of value of 0.46. The results are shown in Figure 4-76 where it can be seen that the POH values from crack initiation increases and peaks at a crack length about 15 mm after which it steadily declined with its minimum at a crack length of about 42 mm and then fluctuations were observed with peaks at 60 mm, 85 mm and 108 mm. Correlating this trend with the averaged AE hit rates shown in Figure 4-21, it can be seen that the initial peak at 15 mm corresponds with Stage 1, the trough around 40 mm corresponds to Stage 2 and the subsequent values can be loosely associated with Stages 3 and 4.

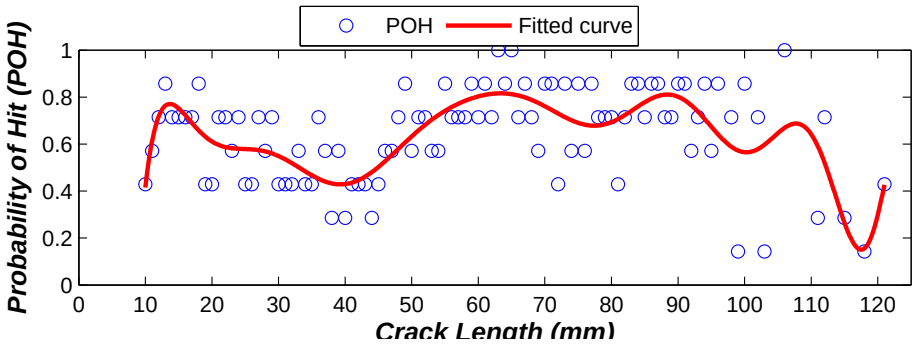

Figure 4.76: Probability of detecting at least 1 AE signals per mm of crack growth for 7 identical tests on SEN samples

Another iteration of the process to determine POH at various crack lengths was performed assuming a higher detection threshold of 10 hits/mm and the results are illustrated in Figure 4-77. This was also performed using the Fourier series model with an R-squared of value of 0.64. The trend observed takes a much closer resemblance to the averaged AE hit rates shown in Figure 4-21 with clear correlations to Stages 1, 2, 3 and 4, although the POH values in Stages 1, 2 and 4 appear reduced in magnitude compared to the trend observed with T=1 in Figure 4-76.

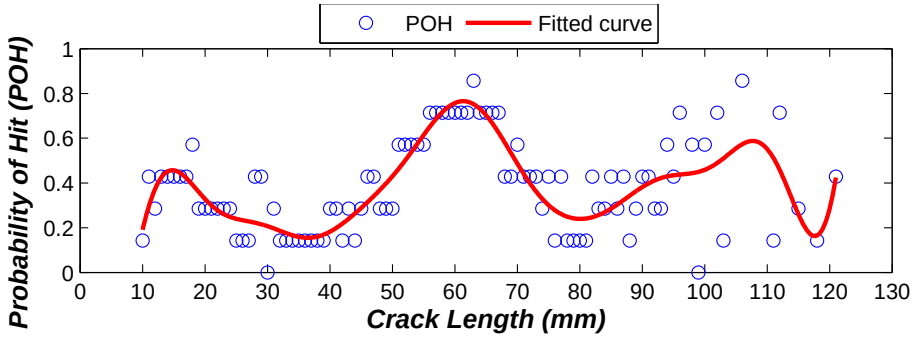

Figure 4.77: Probability of detecting at least 10 AE signals per mm of crack growth for 7 identical tests on SEN samples

MT Samples

POH values at various crack lengths were determined using Equation 4.5 and assuming a detection threshold (T) of 1 hit/mm of crack growth. This was performed considering only Location Groups 1 and 3 in the tests of Samples 8 and 9 as the sensor locations were equidistant from the expected propagation paths of the right and left hand cracks respectively. The results are shown in Figure 4-78, with an R squared value of 0.5, where high values of POH were observed from crack initiation up to a crack length of about 30 mm, after which it declined to 0.2 until 90 mm where there was an increase until final failure.

Another iteration was performed with an increased detection threshold (T) of 10 hits/mm of crack and the results are shown in Figure 4-79, with an R squared value of 0.63. A similar trend was observed compare with Figure 4-78 in terms of the high POH values for crack growth up to a crack length of 30 mm; however the proceeding period until a crack length of 90 mm had POH values less than 0.1.

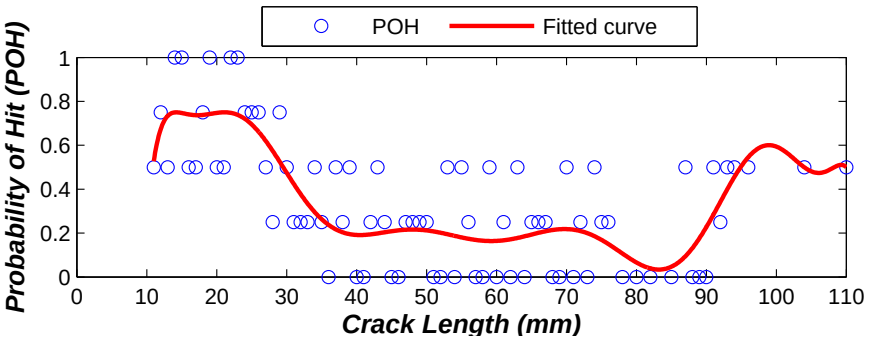

Figure 4.78: Probability of detecting at least 1 AE signals per mm of crack growth for 2 identical tests on MT samples

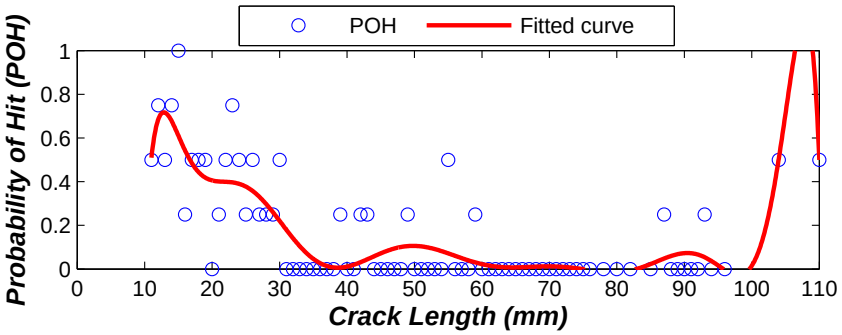

Figure 4.79: Probability of detecting at least 10 AE signals per mm of crack growth for 2 identical tests on MT samples

4.5 Concluding Remarks

Fatigue tests performed under the various loading configurations exhibited expected behaviour in terms of crack growth rates. Spatial filtering methods were applied in the AE setup to ensure exclusive acquisition of AE signals generated from fatigue cracks. Novel metrics developed were used to quantitatively and qualitatively characterise the detection of AE signals generated during fatigue crack growth.

Chapter 5

Characterisation of AE Source Location and Classification

5.1 Introduction

This chapter extends the work done in the previous chapter on verifying AE technique performance in detecting fatigue crack in coupon samples. The data recorded in the various tests conducted, shown in Chapter 4, were analysed in terms of AE source location and AE event classification. A novel metric was developed for characterising the 1D location accuracy and analysis of 2D location estimates with crack growth was performed. Also, a method based on Principal Component Analysis (PCA) and k-means clustering was adopted to study the errors in AE event classification.

5.2 1D Fatigue Crack Location

5.2.1 Metric 4 – Probability of Location (POL)

The accuracy of the AE system in locating AE events generated during fatigue crack growth was characterised using the Probability of Location (POL) metric as stated in Equation 5.1. This was introduced in Section 4.1.1. It is essentially the cumulative probability of errors in location estimates obtained. The error in each location estimate is characterised by error vectors between the estimated and actual crack tip location. Figure 5.1 illustrates an example of a 1D error vector along the vertical axis with respect to the horizontal crack plane.

$$POL(x_i) = \frac{number of observations \leq x_j}{n+1}, x_1 \leq x_2 \leq ... \leq x_n \tag{5.1}$$

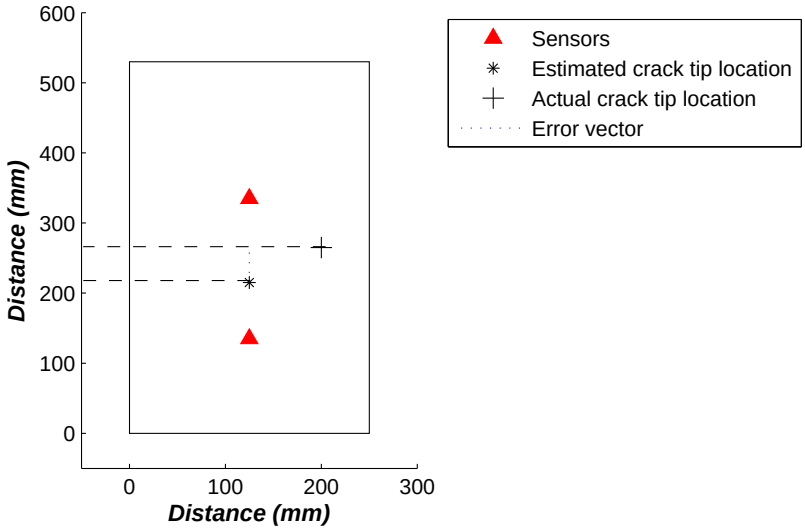

Figure 5.1: 1D location error vector along the vertical axis with respect to the horizontal plane

The POL metric was applied the location estimates obtained in Tests 1 to 7 which were all performed on SEN samples with a maximum stress range of 52.2 MPa, stress ratio of 0.1 and frequency of 2 Hz ,as outlined in Table 4-2, to quantify the 1D location accuracy. The location errors were obtained by determining the magnitude of the error vectors for each estimated location in the tests with a signal detection threshold of 49 dB, after which they were ranked in ascending order and then cumulative probabilities were computed for the various levels of location error. The location performance was characterised by the error margin at 90% cumulative probability of location errors. The POL results for Tests 1 to 7 are illustrated in Figure 5-2. It can be observed that at 90% cumulative frequency the largest location error was 41 mm, obtained both in Tests 4 and 6, and the smallest location 19 mm which was obtained in Test 1.

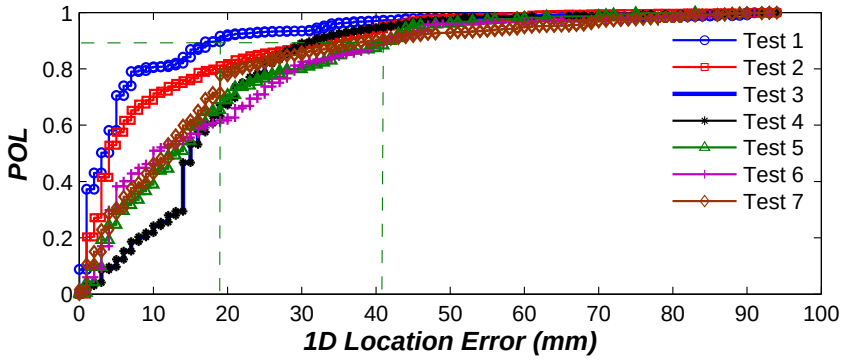

Figure 5.2: POL for Tests 1 to 7 conducted under constant amplitude loading with stress range of 52.2 MPa, stress ratio of 0.1 and loading frequency of 2 Hz

The AE data from Tests 1 – 7 was split, according the trends observed in the distribution of AE Hits with applied load cycles at various crack lengths described in Section 4.3.1.1, into 3 parts defined as follows:

1. **Section I** – AE signals occurring close to the maximum of the loading cycles for crack growth up until a crack length of 75 mm. This corresponds to Trend 2 for Tests 1 – 7 as shown in Figure 4-53.

2. **Section II** – AE signals occurring in the lower two thirds of the loading range for crack growth up until a crack length of 75 mm. This corresponds to Trend 1 for Tests 1 – 7 as shown in Figure 4-53.

3. **Section III** – AE signals occurring around the middle of the loading range for crack lengths approaching sample failure and across the loading range at final failure. This corresponds to Trends 3 and 4 for Tests 1 – 7 as shown in Figure 4-53.

The location errors for the AE data in each of these partitions were determined with an AE signal detection threshold of 49 dB, as previously described, and the corresponding sections in Tests 1 – 7 were grouped together. This resulted in a total of 838 AE events in Section I, 35594 AE events in Section II and 1103 AE events in Section III. The POL metric was also applied to these three sections and the results are illustrated in Figure 5-3. It was observed that the AE events located in Section II gave the best performance with 90% of the AE events located within 30 mm of the fatigue crack. The second best performance was observed for Section III with an error margin of about 40 mm at 90% cumulative frequency and worst performance was seen for Trend 1 with an error margin of 68 mm at 90% cumulative frequency. It was also

observed that although the number of AE events in Section II was 43 times greater than those in Section I and 32 times greater than those in Section III, the vast majority AE events in this portion were more accurate.

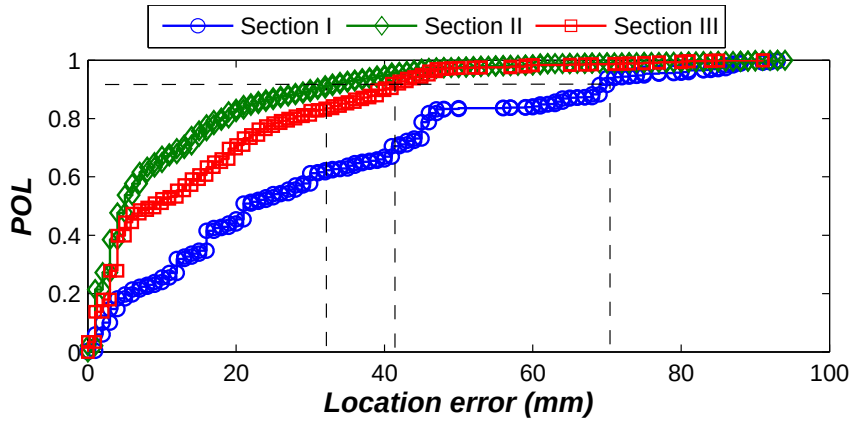

Figure 5.3: POL for Sections I, II and III from Tests 1 to 7 conducted under constant amplitude loading with stress range of 52.2 MPa, stress ratio of 0.1 and loading frequency of 2 Hz

The amplitude distribution of the AE events occurring in these sections of the AE data are shown in Figure 5-4 for Sections I, II and III. This was performed using the Gaussian distribution function in MATLAB. It can be seen that the peak amplitude distribution of AE events were around 52 dB in the case of Section I, 57 dB in Section II and 66 dB in Section III. It can also be seen that the variances in the distribution of Sections II and III were larger compared with that of Section I as there was a wider spread in their distribution towards higher amplitudes. The signals in Section I which had amplitudes closest to the set detection threshold of 49 dB gave the worst location performance and the signals in Section II which had the greatest amplitudes with respect to the detection threshold gave the best location performance.

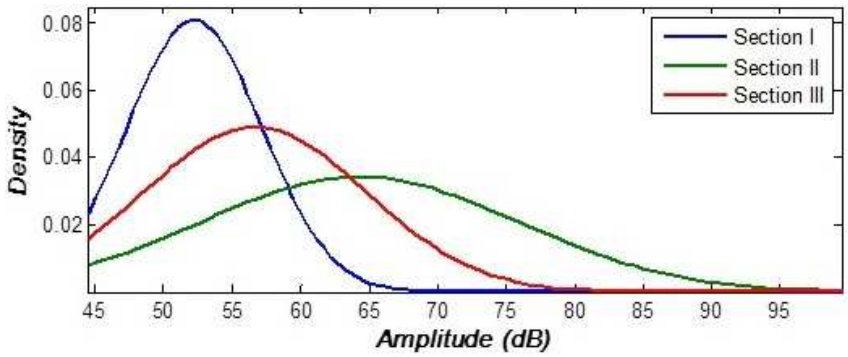

Figure 5.4: Amplitude distribution for Sections I, II and III from Tests 1 to 7 conducted under constant amplitude loading with stress range of 52.2 MPa, stress ratio of 0.1 and loading frequency of 2 Hz

5.3 2D Fatigue Crack Location

The 2D location of AE events for Tests 12, 13 and 14 on SEN samples with stress range of 27 MPa, stress ratio of 0.1 and loading frequency of 4 Hz as outlined in Table 4-2 was performed using timing information from a combination of sensor Location Groups 1 and 2 as described in Chapter 3. This was done for discrete periods of crack growth between 10 – 30 mm, 30 – 60 mm, 60 – 90 mm, 90 – 120 mm and 120 mm to final failure. The Kernel Density Estimation (KDE) method, as described in Section 2.4.3.3 was used to represent the distribution of the estimated 2D AE events in each of these partitions and the results are shown in Figure 5-5, Figure 5-6 Figure 5-7 for Tests 12, 13 and 14 respectively.

In Figure 5-5 which shows the results Test 12 it was observed that there was considerable amount of scatter in the location estimates, however the densities in their distribution could be seen in the superimposed contour plots. For crack growth up to 30 mm the greatest density was seen at a similar location of crack growth along the crack plane but in the case of subsequent increments of crack growth up to 90 mm the greatest density was at the same location as previously observed for crack growth up to 30 mm. The AE events generated during crack growth between crack lengths of 90 and 120 mm can be seen to be located in that vicinity along the crack plane. Final failure of the test sample occurred at 153 mm and the greatest density of the AE location estimates can be seen in the region leading up to the failure crack length.

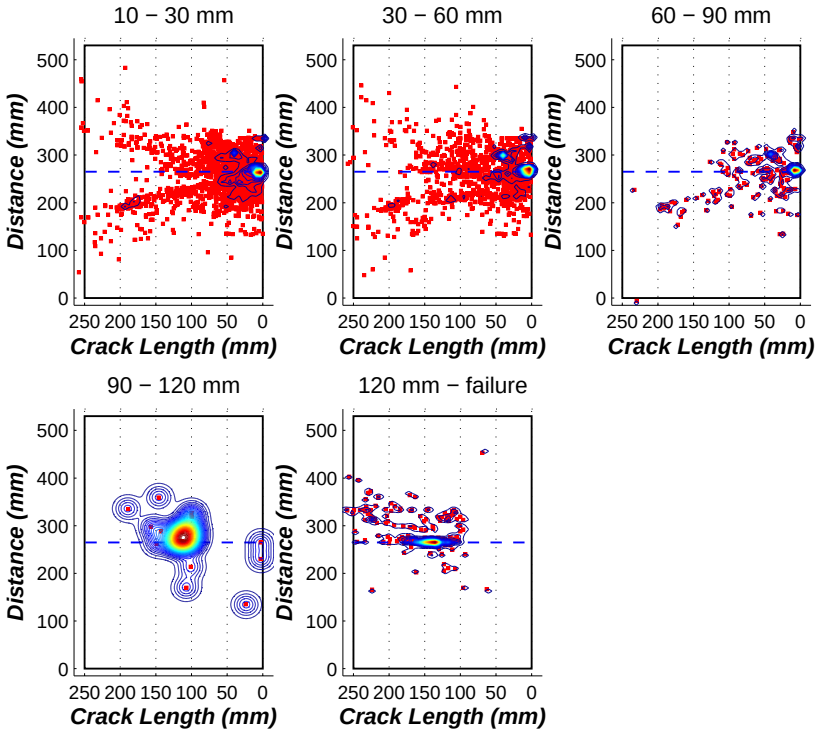

Figure 5.5: Distribution of AE events locations estimates for increments of crack growth until final failure for Test 12 performed on an SEN sample with σ= 27 MPa, f = 2 Hz and R = 0.1

In Figure 5-6 which shows the results Test 13 it was observed that for crack growth up to 30 mm the greatest densities of the location estimates were from the edge of the sample up to about 40 mm along the crack plane. For crack growth between crack lengths of 30 and 60 mm the highest densities of location estimates can also be seen to extend from the edge of the sample, however this time it was up to 55 mm along the crack plane. In the case of crack growth between crack lengths of 60 and 90 mm it was observed that the location estimates previously seen extending from the right edge of the sample was absent and the location estimates were sparsely distributed between 70 and 120 mm along the crack plane with no clear definition of it highest density. The largest cluster of AE events generated during crack growth between crack lengths of 90 and 120 mm can be seen to be located between 90 and 140 mm along the crack plane. Final failure of the test sample occurred at 150 mm and the greatest density of the AE location estimates can be seen around this region on the crack plane.

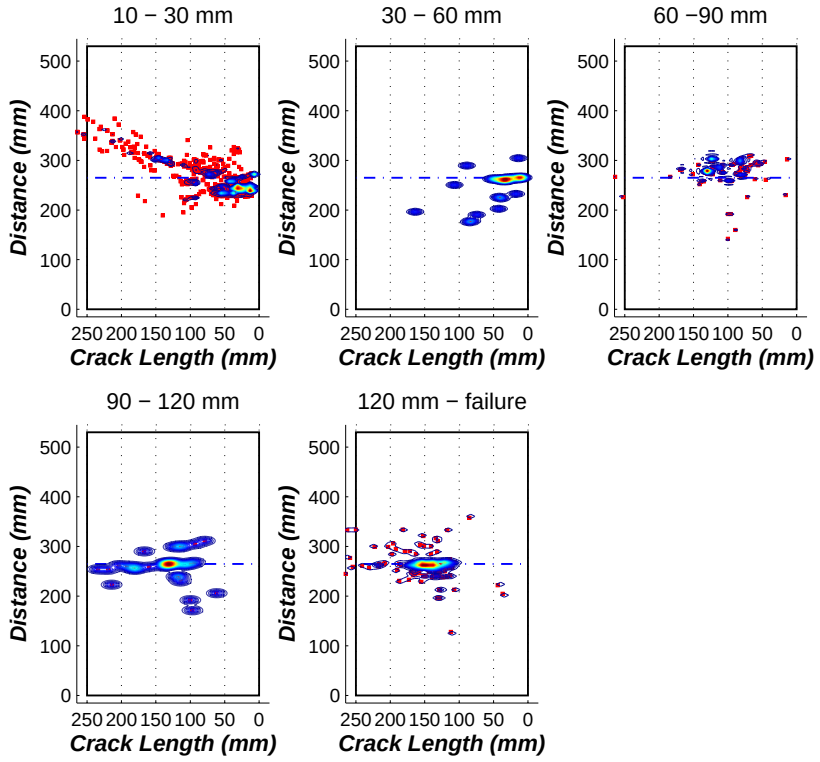

Figure 5.6: Distribution of AE events locations estimates for increments of crack growth until final failure for Test 13 performed on an SEN sample with σ= 27 MPa, f = 2 Hz and R = 0.1

In Figure 5-7 which shows the results Test 14 it was observed that there was some scatter in the AE event location estimates for the first two increments of crack growth up to a crack length of 60 mm, although it appeared significantly less compared with similar regions of crack growth in Test 12, shown in Figure 5-5. For crack growth up to 30 mm the greatest densities of the location estimates was around the region of the initiating notch root, extending to about 20 mm along the crack plane. Between crack lengths of 30 mm and 60 mm AE events can be seen along this region of crack growth and peaks in the density of the distribution can also be seen at 40 mm and 60 mm as well as around the notch root, as previously seen in Figure 5-5 and Figure 5-6 for Tests 12 and 13 respectively. In the case of crack growth between crack lengths of 60 and 90 mm two distinct clusters of AE event location estimates were observed, one of which was in the region of crack growth and the other was around the notch root, as observed in previous tests. The AE events generated during crack growth between crack lengths of 90 and 120 mm can be seen to be located in that vicinity along the crack plane. Final failure of the test sample

occurred at 143 mm and the greatest density of the AE location estimates can be seen in the region leading up to the failure crack length.

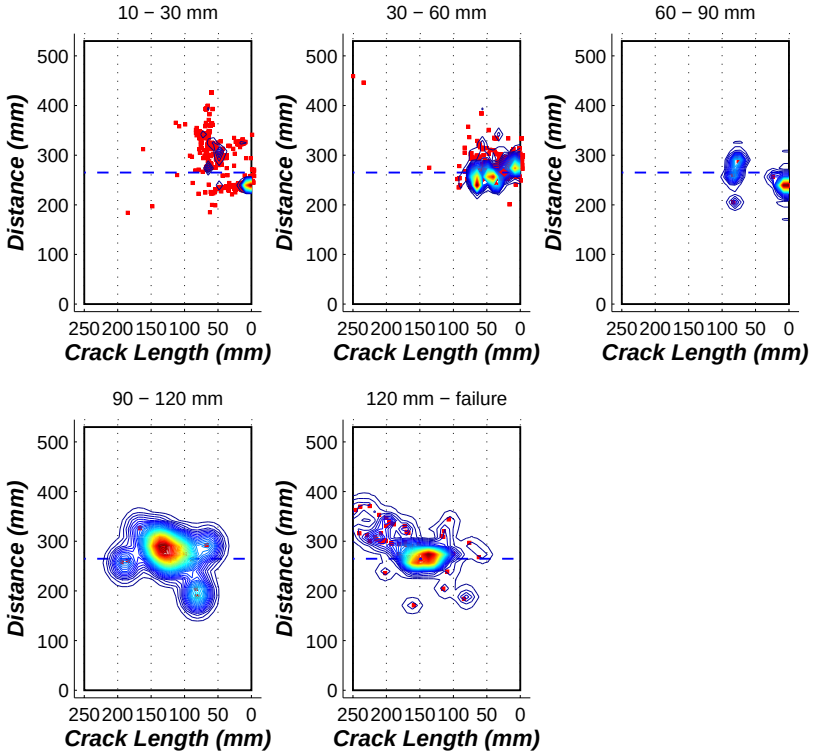

Figure 5.7: Distribution of AE events locations estimates for increments of crack growth until final failure for Test 14 performed on an SEN sample with σ= 27 MPa, f = 2 Hz and R = 0.1

The 2D location of AE events for Tests 15 conducted on an MT sample with stress range of 27 MPa, stress ratio of 0.1 and loading frequency of 4 Hz as outlined in Table 4-2 was also performed. This was done cumulatively for all location estimates obtained during the test until final failure and the distribution was determined using the Kernel Density Estimation (KDE) method, as described in Section 2.4.3.3. The results are shown in Figure 5-8. It can be seen that although there is significant scatter in the location estimates, they also appear to be delineated into two parts which would correspond to the fatigue cracks emanating from either side of the notch, located between 115 – 135 mm on the horizontal plane. The greatest densities in AE event location estimates appear to be in the left-hand region of the distribution where it can be seen to be located between 100 – 130 mm which approximately corresponds to the period of growth between half crack lengths of 10 – 30 mm.

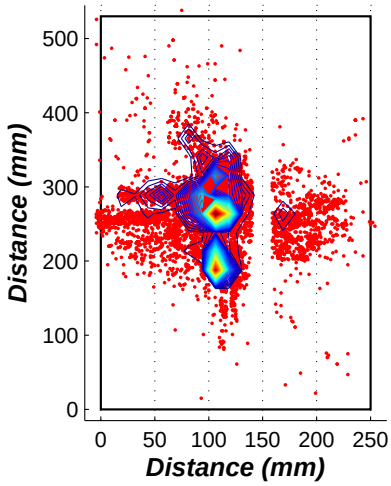

Figure 5.8: Distribution of cumulative AE events locations estimates for Test 15 performed on an MT sample with σ = 27 MPa, f = 2 Hz and R = 0.1

5.4 Classification

Different sources of AE signals can be distinguished by performing dimensionality reduction of AE signal features using Principal Component Analysis (PCA) along with k-Means clustering, as described in Section 2.4.3.1. A supervised process for quantifying classification errors obtained with these methods was performed in the following steps:

1. Normalise the AE data set by dividing the values of each feature by their respective standard deviations.
2. Assign indices to the various observations of the AE features.
3. Perform PCA on all AE features.
4. Perform k-means clustering on the resulting principal components using the known number of AE sources in the data set as the target cluster, incorporating at least 95% variance in the data set.
5. Correlate the latent variables from PCA to the original AE data using the previously assigned indices.

Step i was necessary as the AE signal features were of different units which could cause a bias in the PCA output towards the AE signal features with larger physical dimensions [69]. There is no general means of deciding how many principal components or how much percentage variance is needed to adequately

represent a data set [62], hence a minimum threshold of percentage variance of at least 95% is adopted for all iterations of this process. This procedure was implemented in MATLAB using the princomp and kmeans functions to perform PCA and k-means clustering respectively. AE signals from various sources were generated and the influence of AE signal propagation distance on AE source classification was investigated.

5.4.1 Effect of propagation distance on AE signal features

Investigations on the effect of AE signal propagation distance on AE signal features were conducted on AE data recorded from performing pencil lead breaks (PLBs) in two cases. The first considers AE signals from PLBs at distributed locations across the area of test samples with different sensor locations, while the second considers AE from repeated PLBs at specific locations on test samples with fixed sensor locations.

AE signals with similar propagation distance

For the first case PLBs were performed at various distributed locations on a 1 x 2 m aluminium sheet with a 3-sensor configuration and a 450 x 550 mm with both 3 and 4-sensor configurations as illustrated in Figure 4-4, Figure 4-5 and Figure 4-6. The three AE data sets were identical apart from the relative distances from the PLB location to the sensors where they were detected which varied from sample to sample and was generally larger in the 1 x 2 m sample compared to the 450 x 550 mm sample. Steps i to iii were undertaken to perform PCA on all the 14 AE signal features, listed in Table 3-5. The results for the first two principal components are shown in Figure 5-9 where it was observed that three clusters can be identified with each of them corresponding to AE events recorded in the three AE data sets. However, separation between these clusters was not distinct as there were areas of overlap particularly between the two AE data sets obtained in the 450 x 550 mm sample.

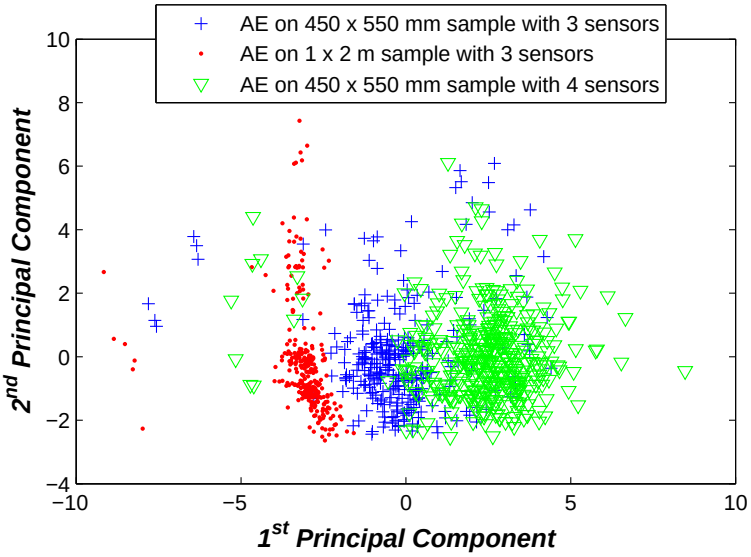

Figure 5.9: PCA of AE signals generated from PLBs performed at distributed locations across the area of test samples with different sensor locations

AE signals with different propagation distances

For the second case repeated PLBs were performed at three locations on a 250 x 530 mm aluminium sample with two sensors as illustrated in Figure 5-10. AE data exclusively recorded at sensor 2 was considered to ensure similar propagation distances for AE signals originating from the same location. The approximate distance to sensor 2 from PLB location 3 was 135 mm, 70 mm for PLB location 2 and at least 170 mm for PLB location 1.

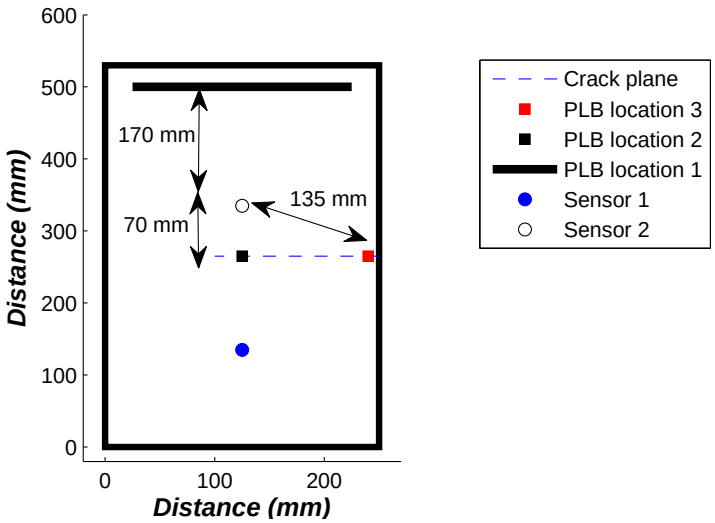

Figure 5.10: PLB and sensor locations on test sample

Steps i to iii were undertaken to perform PCA on all AE signal features and the results for the first two principal components are shown in Figure 5-11. It was observed that the clusters corresponding to the AE signals from the different PLB locations were visibly separated. Most notably the PLBs at location 1 which had the farthest propagation distance appeared more distinct from the other two data sets which had shorter propagation distances in comparison. Some outlying data points were also observed for each of the data sets.

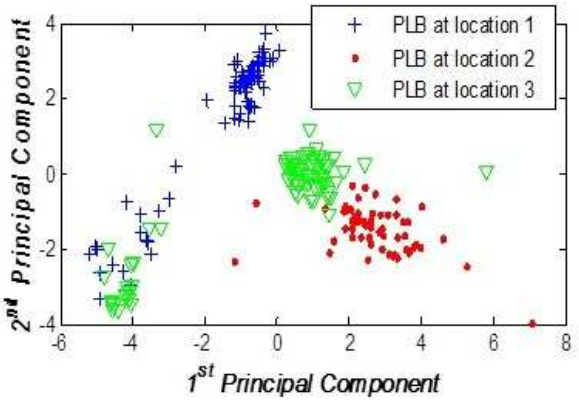

Figure 5.11: PCA of AE signals from PLBs performed at specific locations on test samples with fixed sensor locations

5.4.2 Effect of propagation distance on AE signal classification

Investigations on the effect of AE signal propagation distance on AE signal classification errors were conducted on AE data recorded from performing pencil lead breaks (PLBs) along with AE data from fatigue crack propagation and test machine grip fretting. This was performed in two scenarios, considering AE signals from different sources with similar propagation distance in the first and then AE signals from different sources with different propagation distances in the second.

AE signals with similar propagation distance

AE data sets were generated from PLBs, test machine grip fretting and fatigue crack propagation on a 250 x 530 mm aluminium sample. The machine grip fretting AE data was generated by subjecting a test sample without a crack initiating notch to constant amplitude sinusoidal fatigue loading and recording

the resulting AE signals which may have been generated from either or both grips. AE data from fatigue crack propagation was obtained from Test 1, as listed in Table 4-2, including all the AE signals generated throughout the test until final failure. Finally, two sets of AE data from PLBs were generated by performing distributed PLBs across the crack plane and span of the test machine grip. To ensure similar propagation distance for all the AE signals generated from different AE sources, only AE signals detected at sensor 2 were considered in this data set.

PCA was applied to the AE data from fatigue crack propagation together with AE data from PLBs performed across the crack plane and the results of the first and second principal components are illustrated in Figure 5-12. It can be observed that there were some outlying data points; however the clusters corresponding to the different data sets can be seen to overlap in some areas. Clustering was performed on the first seven principal components which accounted for 97% of variance in the entire data set. The results of supervised classification based on the clustering outcome are represented in a confusion matrix shown in Table 5-1 where classification errors of 61% can be observed for the AE signals generated from fatigue crack and 32% for the AE signals generated from PLBs.

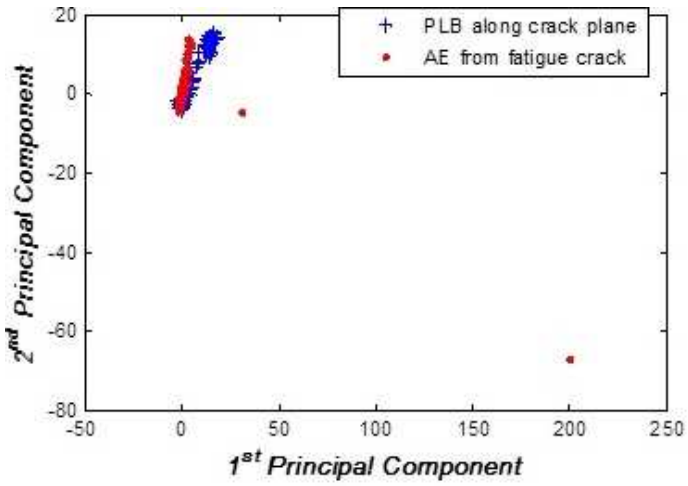

Figure 5.12: PCA of AE signals from PLBs performed along the crack plane and AE signals from fatigue crack propagation with fixed sensor locations

Table 5.1: Confusion matrix of classification errors between AE signals from PLBs performed along the crack plane and AE signals from fatigue crack propagation

		Predicted Class	
		PLB	Crack
Actual Class	PLB	61 (68%)	28 (32%)
	Crack	4670 (61%)	3015 (39%)

The feature reduction and classification process previously described was applied to the AE data from test machine grip fretting together with AE data from PLBs performed across the span of the test machine grip and the results of the first and second principal components are illustrated in Figure 5-13. It was observed that although the extreme regions of the clusters corresponding to the different AE sources were separate, they can also be seen to converge about a common point.

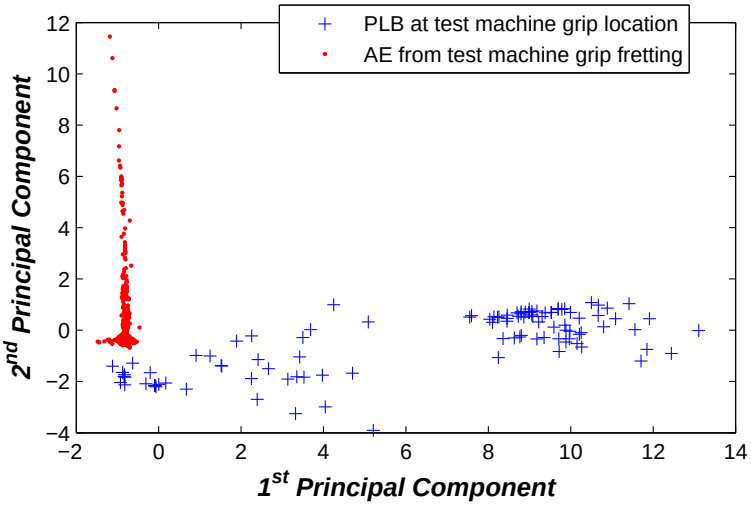

Figure 5.13: PCA of AE signals from PLBs performed along the span of the test machine grip location and AE signals from fatigue crack propagation with fixed sensor locations

Clustering was also performed on the first seven principal components which accounted for 97.1% of variance in the entire data set. Supervised classification of the results are shown in Table 5-2 where there was no misclassification of the AE signals from test machine grip fretting however there was an error of 39% was observed for the AE signals from PLBs.

Table 5.2: Confusion matrix of classification errors between AE signals from PLBs performed along the span of the test machine grip location and AE signals from fatigue crack propagation

		Predicted Class	
		PLB	Fretting
Actual	PLB	68 (61%)	44 (39%)
Class	Fretting	0	843 (100%)

AE signals with different propagation distances

AE signals from fatigue crack propagation obtained in Test 1, as specified in Table 4-2, together with AE signals from PLBs at location 2 on the crack plane, as shown in Figure 5-10, were considered as a data set. The AE data consisted of AE signals detected at sensor 2 with an approximate propagation distance of 70 mm for those generated from PLBs and up to 135 mm for those generated from fatigue crack propagation across the width of the sample. There were a total of 56 AE signals from the PLBs and 7685 AE signals from fatigue crack growth.

PCA was applied to all 14 features of the AE signals in these data sets and the results of the first two principal components are illustrated in Figure 5-14. It was observed that there were two clusters with each of them corresponding to AE events from either of the AE sources. In comparison with similar analysis done on AE data from fatigue crack and PLBs across the crack plane, shown in Figure 5-10, separation between the two clusters appear to be marginally wider.

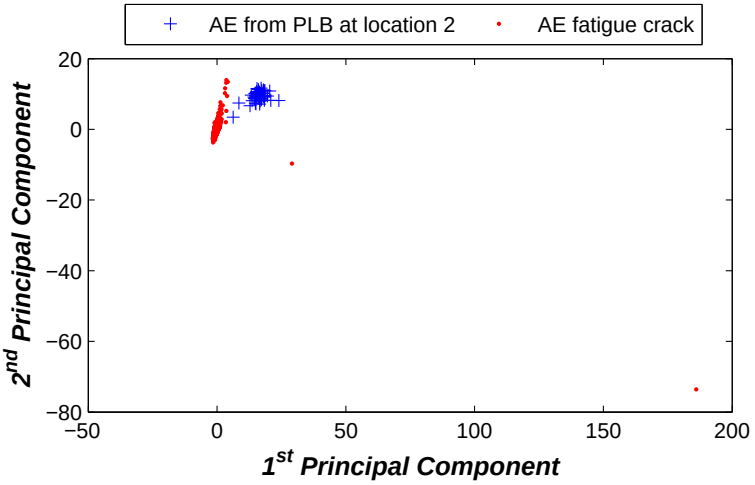

Figure 5.14: PCA of AE signals from PLBs performed at Location 2 along the crack plane and AE signals from fatigue crack propagation with fixed sensor locations

Clustering was also performed on the first seven principal components which accounted for 97.6% of variance in the entire data set. The results were compared with the actual origins of the AE signals and represented in a confusion matrix shown in Table 5-3. In comparison with the results for AE data from fatigue crack and PLBs across the crack plane, shown in Table 5-2, it was observed that the classification error was improved for the AE signals from PLB, however a classification error of 60% was observed for the AE signals from the fatigue crack.

Table 5.3: Confusion matrix of classification errors between AE signals from PLBs performed at Location 2 along the crack plane and AE signals from fatigue crack propagation

		Predicted Class	
		PLB	Crack
Actual	PLB	56 (100%)	0
Class	Crack	4667 (60%)	3018 (40%)

The feature reduction and classification process was applied to the AE data from test machine grip fretting together with AE data from PLBs performed at location 2 on the crack plane, as shown in Figure 5-10. This consisted of AE signals detected at sensor 2 with an approximate propagation distance of 70 mm for those generated from PLBs and at least 170 mm for those generated

from test machine grip fretting. There were a total of 56 AE signals from the PLBs and 843 AE signals from test machine grip fretting. The results of the first and second principal components are illustrated in Figure 5-15.

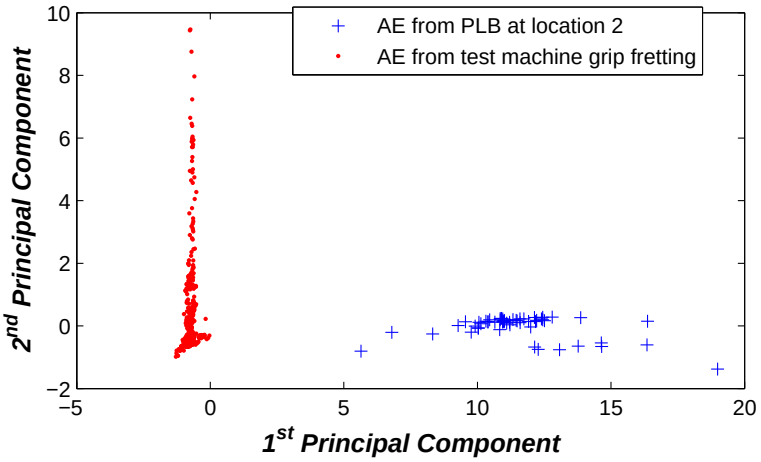

Figure 5.15: PCA of AE signals from PLBs performed at Location 2 along the crack plane and AE signals from test machine grip fretting with fixed sensor locations

Clustering was also performed on the first seven principal components which accounted for 97.3% of variance in the entire data set and the results were compared with the actual origins of the AE signals and represented in a confusion matrix shown in Table 5-4. Comparing this with the results for AE data from test machine grip fretting and PLBs across the span of grip, shown in Table 5-2, it was observed that they were much improved with no classification errors.

Table 5.4: Confusion matrix of classification errors between AE signals from PLBs performed at Location 2 along the crack plane and AE signals from test machine grip fretting

		Predicted Class	
		PLB	Fretting
Actual	PLB	56 (100%)	0
Class	Fretting	0	843 (100%)

5.5 Concluding Remarks

The accuracy of the AE technique in performing 1D location of fatigue crack in various tests was determined to be between 19 mm and 41 mm. It was also observed that the AE signals associated with Trend 1, where they were produced in the lower two-thirds of the loading range for crack growth up to a total length of 80 mm, were of greater amplitudes compared with the other signals generated. Better location accuracy was also obtained with these signals.

For SEN samples, the majority of AE signals generated from crack growth up to a length of 80 mm were seen to be produced mainly between crack lengths of 10 mm and 20 mm, even after crack growth beyond this region.

AE event classification using PCA and k-means clustering was also performed on different AE data sets which showed that the ability to correctly distinguish between AE signals from different sources in more sensitive to the effects of propagation distances than the inherent characteristics of the different source.

Chapter 6

Validation of AE Detection and Location in a Wing-box Structure

6.1 Introduction

Chapters 4 and 5 dealt with performance verification of the AE technique in fatigue crack detection, location and AE source classification under controlled conditions, using coupon samples. This chapter on the other hand deals with another important aspect of performance evaluation which is concerned with validation of the technique in realistic structures. The AE results of tests performed on a wing-box structure are given in this chapter.

6.2 Wave velocity calibration

The AE system's built-in Automatic Sensor Test (AST) function, described in Section 3.2.3, was used to determine the arrival time delay between sensor pairs. With the sensors mounted in the assembled wing-box structure, the AST function was used to send 50 pulse signals, with 5 μs length and 100 ms delays between pulses, to each sensor in a Location Group. The average time delay of AE arrival was recorded. Given a distance of 290 mm between sensors in the same spar, the average wave velocity was calculated. The results for the different interrogation paths are shown in Table 6-1.

Table 6.1: Average time delay and wave velocity with acousto-ultrasonic interrogation between the two pairs of sensors

Sensor interrogation (sending-receiving)	Average Δt (μs)	Wave velocity kms
5-6	105	2.76
6-5	103	2.81
3-4	118	2.45
4-3	102	2.84
	Mean	2.72

6.3 Test 1 – Tension-Tension

6.3.1 1D AE source location

Test 1 was performed for a total of 66,033 fatigue load cycles with interruptions at 6815, 21018 and 55018 cycles for independent verification of crack growth using a Borescope and an Eddy Current probe without disclosure of the crack location. The results of AE event location estimates for Location Groups 1 and 2 are illustrated in Figure 6-1 and Figure 6-2 respectively, assuming an average wave velocity of 2.72 km/s. In Figure 6-1, it is shown that the distribution of AE event location estimates was between 270 – 300 mm along the horizontal axis. The greatest peak occurred at approximately 280 mm, corresponding to a position between Holes 11 and 12, as shown in Table 3-7. A few AE events were also detected by Location Group 2 despite not containing a seeded crack, as shown in Figure 6-2. These were located between 280 – 310 mm along the horizontal axis, corresponding to the region between Holes 11 and 13.

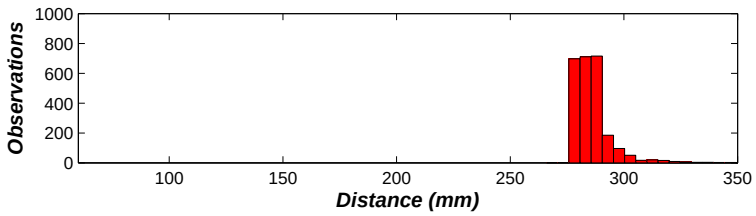

Figure 6.1: Distribution of 1D AE event location estimates in Test 1, with detection threshold of 45 dB and high-pass filtering $\geq$ 75 dB using Location Group 1 (sensors 5 and 6)

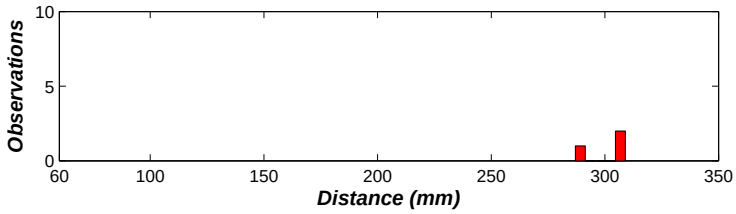

Figure 6.2: Distribution of 1D AE event location estimates in Test 1, with detection threshold of 45 dB and high-pass filtering $\geq$ 75 dB using Location Group 2 (sensors 3 and 4)

6.3.2 2D AE source location

Using the AE arrival time delay measurements from both Location Groups 1 and 2, 2D damage location estimates were performed also assuming a propagating wave velocity of 2.72 km/s. These results are presented in Figure 6-3. Both the 2D location estimates, as well as their distribution determined using the Kernel Density Estimation (KDE) method are shown superimposed over a drawing of the wing-box structure plan view. It was observed that there was one main cluster of AE events with its peak displaced from the test spar by 50 mm along the vertical axis of the wing-box. In the horizontal direction, this peak was located at approximately 600 mm from the tip of the wing-box, corresponding approximately to Hole 10.

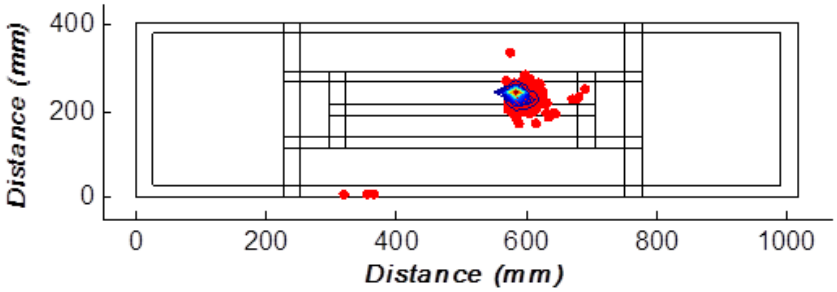

Figure 6.3: Distribution of 2D AE event location estimates on wing-box structure in Test 1 using KDE

6.3.3 AE distribution with applied load cycles

The distribution of recorded AE signals from the sensors in both Location Groups 1 and 2 across the applied load range with increased fatigue load cycles was obtained using the Kernel Density Estimation (KDE) method described in Section 2.4.3.3. The results are shown in Figure 6-4. It can be observed

that in the period from the start of the test up to 30,000 fatigue load cycles AE signals occurred across the loading range with the vast majority of them occurring close to the maximum. For the remaining period of the test AE signals were observed to occur sparsely across the loading range compared to the previous period and their greatest densities were close to the minimum applied load.

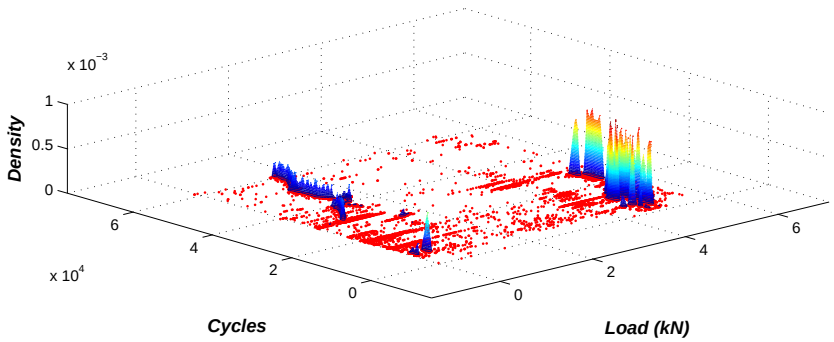

Figure 6.4: AE Hit distribution in the applied load range with increasing load cycles for both Location Group 1 and 2

6.4 Test 2 – Tension-Compression

6.4.1 1D AE source location

Test 2 was performed for an additional 15000 fatigue load cycles with the location of the crack still undisclosed. The results for AE location estimates for Location Group 1 and 2 are illustrated in Figure 6-5 and Figure 6-6 respectively, also assuming an average wave velocity of 2.72 km/s. It was observed that the location distribution ranged from 240 – 300 mm, with its peak occurring at 250 mm, corresponding approximately to Hole 10 as shown in Table 3-7. An almost identical distribution was observed for Location Group 2; however, with fewer AE signals were detected.

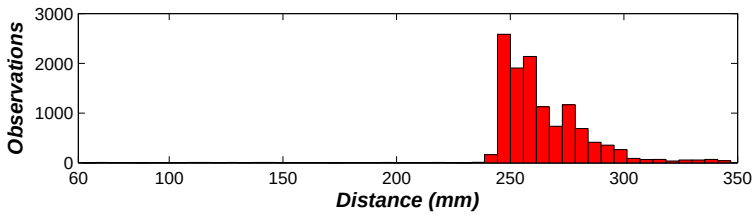

Figure 6.5: Distribution of 1D AE event location estimates in Test 2, with detection threshold of 45 dB and high-pass filtering $\geq$ 90 dB using Location Group 2 (sensors 5 and 6)

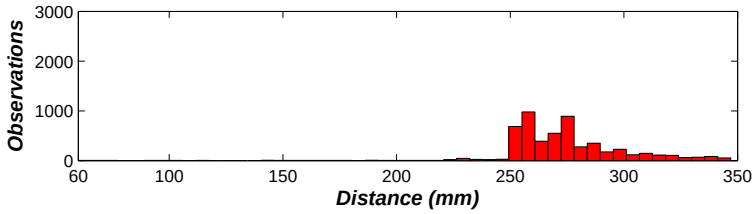

Figure 6.6: Distribution of 1D AE event location estimates in Test 2, with detection threshold of 45 dB and high-pass filtering $\geq$ 90 dB using Location Group 2 (sensors 3 and 4)

6.4.2 2D AE source location

The 2D location estimates were also performed using the AE arrival time delay measurements from both Location Groups 1 and 2, and the results are illustrated in Figure 6-7. It can be observed that there was significantly more scatter in damage location estimates as compared with Test 1. The peak of the location estimate distribution was displaced from the test spar by 100 mm on the horizontal axis. On the vertical axis, the peak was located between 570 - 600 mm, corresponding to the region between Holes 9 and 11.

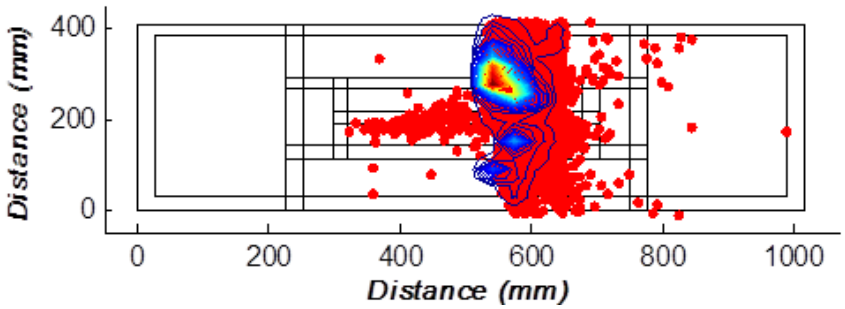

Figure 6.7: Distribution of 2D AE event location estimates on wing-box structure in Test 2 using KDE

6.4.3 AE distribution with applied load cycles

The distribution of recorded AE signals from the sensors in both Location Groups 1 and 2 across the applied load range with increased fatigue load cycles was obtained using Kernel Density Estimation (KDE) and the results are shown in Figure 6-8. It was observed that from the onset AE signals were distinctly generated close to the maximum of the loading range as well as around 0 kN. This trend was sustained for prolonged period.

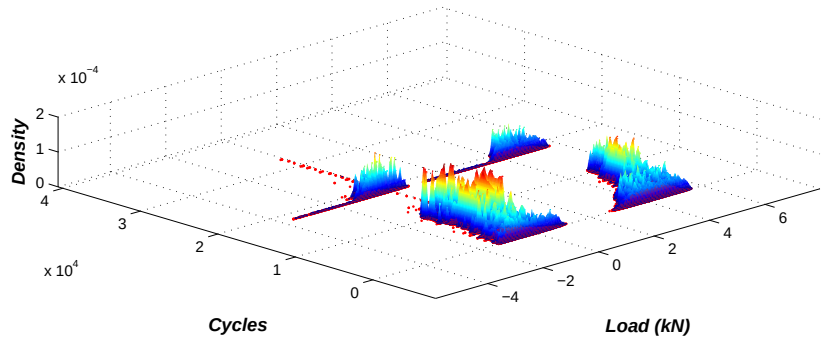

Figure 6.8: AE Hit distribution in the applied load range with increasing load cycles for both Location Group 1 and 2

6.5 Non Destructive Inspection (NDI) of wing-box

Non Destructive Inspection (NDI) was independently performed by the National Research Council of Canada (NRC) on the entire wing-box using Eddy Current, Ultrasonic and Fluorescent Penetrant techniques and the results for the test spar are given in Table 6-2. These inspections identified the location of the 'hidden' crack to be at Hole 11. It was observed that other holes had not develop fatigue cracks, apart from Hole 9 which showed a crack-like indication with the Eddy Current technique, which could not be confirmed using the ultrasonic and fluorescent penetrant methods. Also, no other cracks were found in other parts of the wing-box, although there were some signs of minor damage around some fastener holes.

Table 6.2: Non Destructive Inspection of wing-box structure

Hole number	Eddy Current inspection	Ultrasonic inspection	Dye-penetrant inspection	Notes
9	Yes	No	No	Crack-like indication < 0.76 mm
11	Yes	Yes	Yes	Confirmed 4.2 mm crack

6.6 Concluding remarks

The experimental setup was very representative of a realistic damage monitoring situation. The AE system was configured to detect and locate AE sources in the structure. This resulted successful location of the 'hidden' fatigue crack with an accuracy of 6 mm in Test 1 and 24 mm in Test 2. The complex propagation paths in the structure were also uniquely exploited to perform wider area monitoring with the same sensor set.

Chapter 7

Discussion

7.1 Introduction

The aim of this work was to quantitatively characterise the performance of AE technique in detecting and locating fatigue crack for structural health monitoring purposes. Tests were performed to monitor fatigue crack growth in both coupon samples and a representative wing-box structure. The results presented in preceding chapters are discussed here in context of validation and verification of the performance of the AE technique, in light of current state of the art. A novel approach for fatigue crack length estimation is also presented in this chapter.

7.2 Variability in AE generation from fatigue crack

With the spatial filtering methods adopted in the test setup described in Section 3.2.4 the AE signals recorded during the various tests conducted are assumed to be associated with fatigue crack growth. However, it was also important to understand if there was any significant effect of sensor position relative to the crack at various points of growth on their sensitivity in detecting the AE signals generated. Potential influencing factors are attenuation with increased propagation distance or directionality in the radiation pattern of the signals for example [84; 104]. For this reason two pairs of sensors were used in the guard sensor configuration to simultaneously and independently monitor AE signals during the tests. For the tests performed on SEN samples, variation in AE hit rates by less than a factor of 2 was typically observed for any given crack length, although greater rates were consistently observed, particularly at crack lengths less than 20 mm, with Location Group 1 (sensors 1 and 2) which was positioned closer to the initiating notch, compared to Location Group 2 (sensors 5 and 6) which was in the middle of the sample. This may not have

any notable difference for tests where large amounts of AE signals were observed but could be more significant in the tests where minimal amounts of AE signals were generated.

For the tests performed on MT samples, the AE signals detected by the different pairs of sensors were more intermittent at various crack lengths and exhibited larger levels of variation by up to a factor of 15 were observed for crack lengths less than 30 mm and even greater values up to a factor 40 for subsequent crack growth. This can be attributed to the fact that two cracks were present and may not necessarily have exhibited identical behaviour.

The intensity of AE signals generated from fatigue cracks varied quite widely across tests performed on different samples and batches of material under nominally identical loading conditions. The sum of AE hits for four identical ranges of crack growth are shown in Table 7-1 for Tests 1 to 7 which were performed on SEN samples under identical loading conditions. The coefficient of variance for the various stages was calculated and also shown in Table 7-1. These were anomalous as they exceeded the expected maximum of 1 [105]. This is because the data is heavily polarised with ranges up to 36362 units, which can lead to very inaccurate estimation of the mean and consequently standard deviation values greater than the mean. This can be attributed to the small sample size; however this nonetheless indicates the high level of variability in the data.

The AE Hit distribution with applied load cycles for Tests 1 to 7, illustrated in Figure 4-53, shows the four distinct trends observed which are believed to be representative of fatigue processes present during crack growth in SEN samples. However it appeared that some of them were completely absent in certain tests, particularly for those with samples from Batch 2 material. This would counter-intuitively suggest that some of these processes did not occur in some of the tests which is implausible, especially as the mechanical characteristics of the different batches of material were very similar as shown in Table 3-1 and Table 3-2. One possible explanation for this behaviour could be that due to the sensors being located in the middle of the samples for Tests 1 to 7, they were less sensitive to AE signals generated at early crack lengths, as noted earlier.

Table 7.1: Variation in total AE hits for identical periods of crack growth in Tests 1 to 7 performed on SEN samples under identical loading conditions

	Stage 1 (10-20) mm	Stage 2 (20-55) mm	Stage 3 (55-70) mm	Stage 4 (70 mm -failure)
Test 1	13860	46	1030	446
Test 2	36362	4554	1614	660
Test 3	918	2568	2342	660
Test 4	18	208	34	594
Test 5	0	0	6	244
Test 6	46	284	898	834
Test 7	206	3526	2888	1414
Mean	7344	1598	1258	648
Standard deviation	13769	1915	1095	391
Coefficient of variance	1.87	1.19	0.87	0.60

Probability of Detection (POD) curves are the generally accepted means of characterising techniques, with uncertainty requirements in damage that POD detection is using NDT increasing with discontinuity size [106; 107]. As a result prescribed functions are used to represent POD data which are typically monotonically increasing curves with increase in discontinuity size. At the time of preparing this thesis, no probabilistic methods for characterising AE generation during fatigue crack growth until final failure were uncovered.

The Probability of Hit (POH) metric, described in Section 4.3.3, is one of the novel developments in this work. It was applied to AE data from Tests 1 to 7 and the results showed that for a detection criterion of 1 Hit/mm, POH values between 0.6 and 1 were obtained for the majority of crack growth. For an increased detection criterion of 10 Hits/mm a rapid decline in POH values was observed, exhibiting peaks and troughs particularly similar to the stages in the averaged AE Hit rates observed for Test 1 to 7, shown in Figure 4.19. Relating the two plots to each other shows that although the greatest AE Hit rates were observed in Stage I, greater POH values were obtained for Stage III.

7.3 Evolution of AE during fatigue crack growth

In the results for Tests 1 to 7 performed on SEN samples with a stress range of 52.2 MPa and stress ratio of 0.1, presented in Section 4.3, it was intriguing to observe the four trends in AE Hit distribution with applied load cycles as shown in Figure 4-53. In Trend 1, AE signals were seen to be generated around the mean stress for crack lengths between 10 – 20 mm and then subsequently occurring at lower loads with increasing crack length, as seen in Figure 4-53. Scanning Electron Microscope (SEM) inspection of fracture surfaces revealed debris collection at various points of crack growth, as shown in Figure 4-12. This suggested that there were points of contact between the fracture surfaces as the samples underwent cyclic fatigue loading. This observation can be linked with crack closure as described in Section 2.5.

The effects of fatigue crack closure have been widely studied in the past 40 years; Newman (1984) presented a general crack opening stress equation for constant amplitude loading as a function of stress ratio (R), stress level (σ_{max}) and three dimensional constraint (α) as shown in Equation 7-1 to 7-6.

$$\frac{\sigma_{open}}{\sigma_{max}} = A_0 + A_1 R + A_2 R^2 + A_3 R^3, for R \geq 0 \tag{7.1}$$

And,

$$\frac{\sigma_{open}}{\sigma_{max}} = A_0 + A_1 R, for -1 \leq R < 0 \tag{7.2}$$

Where,

$\sigma_{open}/\sigma_{max}$ - Normalised crack opening stress

When $\sigma_{open} \geq \sigma_{min}$, the coefficients were:

$$A_0 = (0.85 - 0.3\alpha + 0.05\alpha^2) \left[cos(\pi\sigma_{max}/2\sigma_0)\right]^{1/\alpha} \tag{7.3}$$

$$A_1 = (0.415 - 0.071\alpha)\sigma_{max}/\sigma_0 \tag{7.4}$$

$$A_2 = 1 - A_0 - A_1 - A_3 \tag{7.5}$$

$$A_3 = 2A_0 + A_1 - 1 \tag{7.6}$$

The relation between normalised crack opening stresses ($\sigma_{open}/\sigma_{max}$) and stress ratio (R) for various applied stress levels (σ_{open}/σ_0) under plane stress condition as shown in Figure 7-1 [108], where σ_0 is termed the flow stress which is the average between the uniaxial yield stress and uniaxial ultimate tensile strength of the material. It was also noted that at high stress ratios, the applied stress has little influence on the crack opening stress.

With the measured yield and ultimate tensile strength of the test presented in Section 3.2, the flow stress was calculated as 465 MPa, 466.5 MPa and 466.5 MPa for Batches 1, 2 and 3 materials respectively. This indicates that for both sets of tests conducted with maximum stress of 58 MPa and 30 MPa, crack opening was calculated to occur at 51% and 53% of the respective maximum stress as illustrated in Figure 7-1.

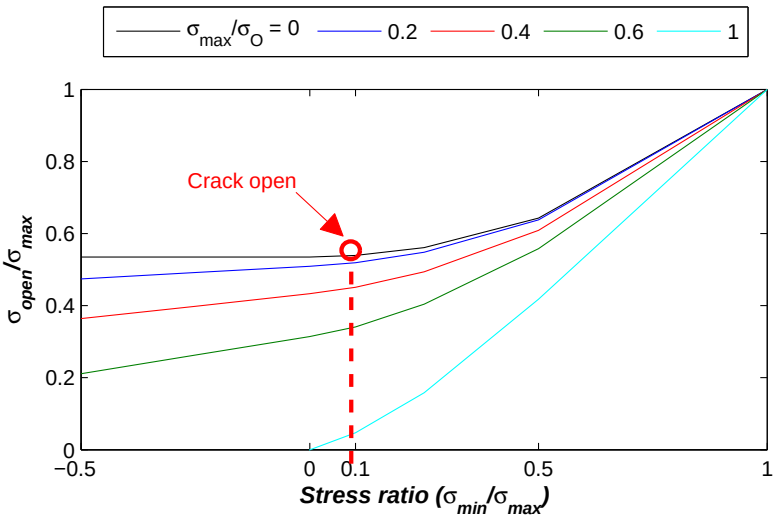

Figure 7.1: Normalised crack-opening stress as a function of stress ratio (R) and stress level for plane-stress conditions

In the cumulative plot of AE Hits distribution with applied load cycles for Tests 1 – 7 shown in Figure 4-53, it can be seen that the greatest densities in the distribution at crack lengths up to 80 mm occurred below about 35 MPa or 60% of the maximum stress in the cycle. This suggests that crack opening at crack lengths less than 20 mm occurred at this point, which is comparable to the generalised prediction calculated to be 51% for the test configuration. Tests 12 and 13 performed on SEN samples with a stress range of 27 MPa and

stress ratio of 0.1, presented in Section 4.3, also showed a similar behaviour where the majority of AE signals associated with Trend 1 occurred below about 51% of the maximum load. However, Test 10 was somewhat exceptional with a significant amount of the AE signals occurring up to 76% of the loading range at similar crack lengths.

2D location estimates for the AE signals associated with Trend 1 was performed for Tests 12 and 14, as listed in Table 4-2, by filtering out AE signals occurring above 70% of the loading range for crack growth up to a crack length of 90 mm. The results for Test 12 are shown in Figure 7-2 for three increments of crack growth, where it can be seen that although there is a significant amount of scatter, the peak in the distribution was located at about 20 mm along the crack plane for each of the increments of crack growth. This shows that these AE signals associated with Trend 1 occur at a particular point close to the initiating notch, even though the crack tip had advanced beyond this region.

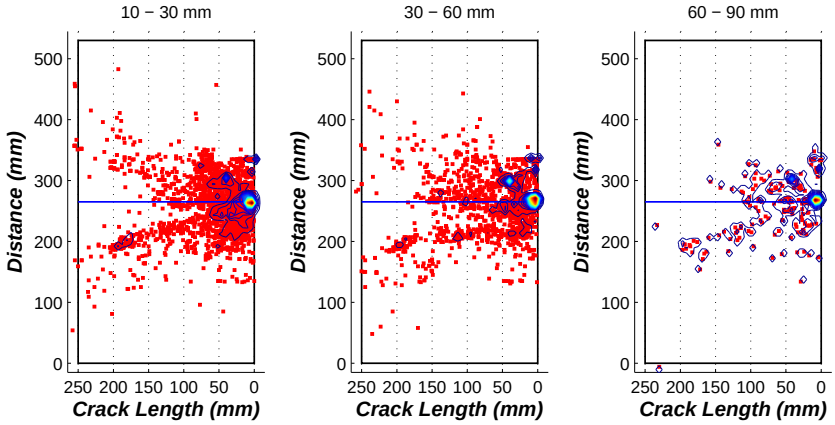

Figure 7.2: Distribution of 2D location estimates for AE signals associated with Trend 1 in Test 12

The results for Test 14 are shown in Figure 7-3 for identical increments of crack growth as in Test 12 which is shown in Figure 7-2. This shows less scatter in the location estimates compared with Test 12, however, a very similar behaviour was also observed in the distribution peak occurring at crack lengths less than 20 mm for each increment of crack growth considered. This corroborates previous observations made in Test 12. It was also interesting to observe that for crack growth between 30 – 60 mm and 60 -90 mm, other peaks in the distribution of location estimates were seen in regions of the crack plane corresponding to the tip. This suggests that the AE signals associated with crack closure occurs close to the notch root, even when the crack tip had

advanced beyond that region of the crack plane, as well as at the crack tip.

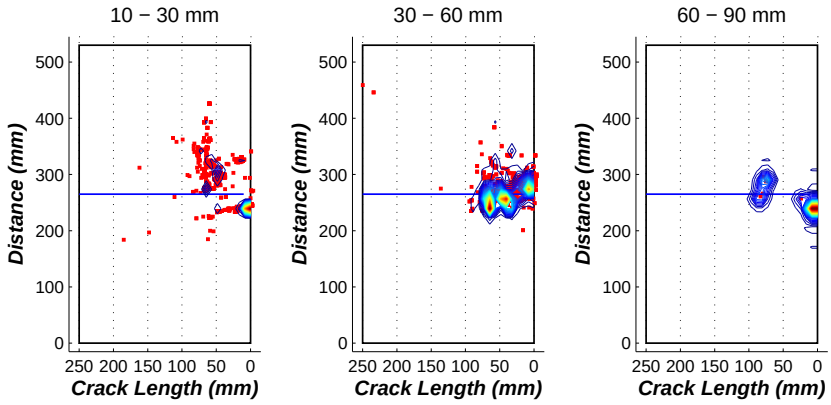

Figure 7.3: Distribution of 2D location estimates for AE signals associated with Trend 1 in Test 14

The averaged AE Hit rates with increasing crack length for the AE signals associated with Trend 1 was performed and the results are shown in Figure 7-4. It can be observed that the hit rates were almost identical to those observed for the entire loading range of Tests 1 to 7, shown in Figure 4-21. In both cases, it can be seen that the peak hit rate for crack lengths less than 20 mm was about 1600 AE Hits/mm, also the hit rates for the majority of crack lengths between 20 – 45 mm were less than 30 AE Hits/mm and less than 120 AE Hits/mm for subsequent crack growth until final failure. This verifies that the vast majority of AE signals generated were associated with Trend 1.

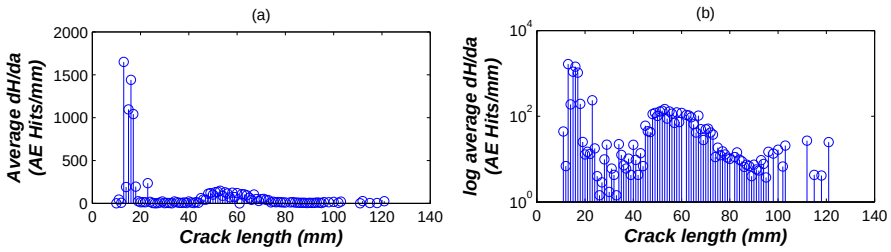

Figure 7.4: Averaged AE Hit rates versus crack length for AE signals associated with Trend 1 in Tests 1 to 7

The decline in AE Hit rates observed in Stage II occurring between 20 – 55 mm, where low AE Hit rates of less than 30 Hits/mm as illustrated in Figure 4-21, could similarly be traced to changes in Trend 1 where minimal AE Signals were also observed at almost identical crack lengths.

Similar periods of minimal AE signal generation from edge cracks, akin to

Stage II, after an initial surge in activity, where they were reported to last up to last up to 80% of the samples fatigue life [52; 87]. In comparison with the averaged AE Hit rates for Tests 1 to 7, this was observed to be 27% of the sample fatigue life. However, it was noted that Daniel et al. (1997) performed the said tests with a much greater stress range of 154 MPa, although with the same stress ratio of 0.1. The difference in these set of results follows the previously observed behaviour where a higher stress range results in longer duration of 'Stage II'.

In the cases of Tests 12 to 14 performed with stress range of 27 MPa and stress ratio of 0.1 which were presented in Section 4.3.2.4, Stage II of the AE Hit rates as previously observed was almost non-existent, which was also evident in the distribution of AE Hits with applied load as shown in Figure 4-63 toFigure 4-68. This suggest that there may be two mechanisms responsible for generating the AE signals associated with Trend 1, corresponding to the crack growth between 10-20 mm and 20 – 50 mm respectively in Tests 1 to 7 and was almost merged together with reduced stress range.

In Trend 2, AE signals were observed close to the maximum of the load cycles. The AE signals associated with Trend 2 were sparsely generated compared with Trend 1 as shown in Figure 7-5 for Trend 2 where maximum hit for the entire period of crack growth was seen to be less than 100 AE Hits/mm. It was also observed to be most prominent at crack lengths less than 50 mm and for crack lengths greater than 80 mm until final failure.

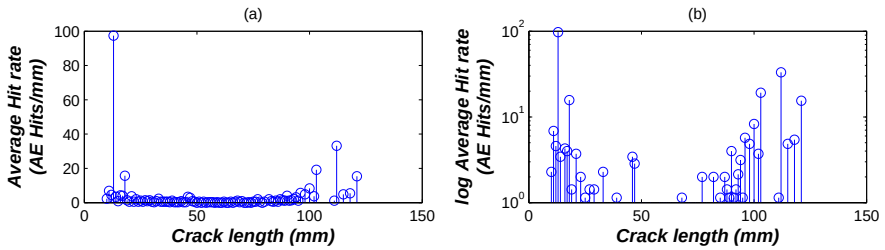

Figure 7.5: Averaged AE Hit rates versus crack length for AE signals associated with Trend 2 in Tests 1 to 7

Trend 2, where AE signals were seen to occur close to the maximum of the applied load cycles, was also observed for Tests 12 to 14 performed on SEN samples with a stress range of 27 MPa and stress ratio of 0.1. This was an intriguing behaviour as such a trail of AE signals occurring at a stress of around 30 MPa with crack growth was not observed for Tests 1 to 7 at similar stress

values, even though it was exceeded in every stress cycle. This suggests that the occurrence of this group of AE signals is more dependent on the turning point of the stress cycle than the stress level.

Similar observations have been made in available literature and these signals are associated with fatigue processes at the crack tip [56; 57]. They are sometimes referred to as primary or material AE, attributed to fracture of inclusions as well as crack extension [2; 82] which can be expected to occur close to the peak of the applied load cycles where the crack tip stress intensity range is at a maximum. This group of AE signals has been the focus of many research studies where correlation of changes in their features with stress intensity range has been demonstrated in performing crack growth rate prediction [31; 46; 55-57;109].

Evidence of the correlation between the crack tip position and the location estimates obtained from the AE signals occurring close to the maximum load in the tests performed was uncovered by filtering out AE events occurring below 70% of the maximum of the load cycles and observing the location estimates with incremental crack growth. From Figure 5-5, Figure 5-6 and Figure 5-7, which show the distribution of 2D location estimates for Tests 12, 13 and 14 respectively, it can be seen that the peak densities of AE location estimates for crack growth from 90 mm until final failure clearly corresponded with the position of the crack tip. Therefore, further data processing was performed for AE data recorded for crack growth up to 90 mm. The results for Test 14 are shown in Figure 7-6 where it can be seen that the different groups of AE events also followed progressive crack growth. This was particularly evident for crack lengths between 60 – 90 mm.

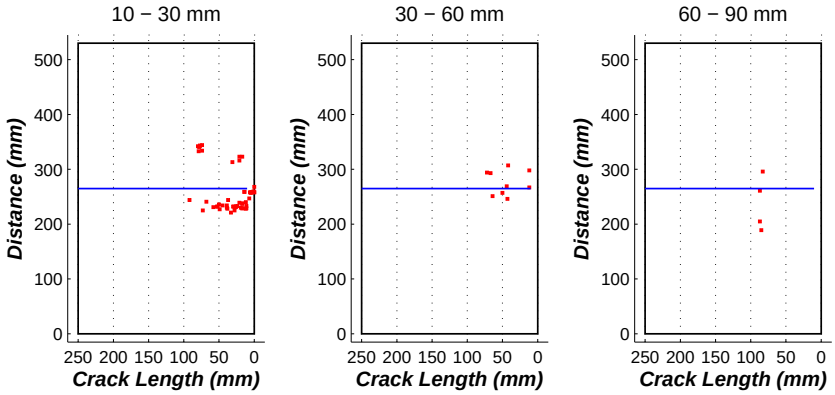

Figure 7.6: AE event location estimates for AE signals occurring in the top 30% of the loading cycles with incremental crack growth

Trends 3 and 4, as illustrated in Figure 4.49, where AE signals were seen to occur around the mean stress with the sample approaching failure and eventually spread across the loading range at failure crack length, were also consistently observed in Tests 12 to 14. They occurred in the final 6% of the samples fatigue life, as shown in Figure 4-22, which is in the period of unstable crack growth before final failure.

In the plots of AE Hit distribution with applied cyclic load for both Tests 12 and 13, shown in Figure 4-63 Figure 4-66, it can be seen that the AE signals were generated at a crack length of 100 mm until final failure. The sources of the AE signals are not known; however, one potential source could be overload fracture [110], where the fracture process occurs almost instantaneously.

The Amplitude distribution of AE signals observed in the various trends of AE Hit distribution with applied loading range for Tests 1 to 7 was presented in Section 5.1 and illustrated in Figure 5-4. It was also quite interesting to note that even for nominal identical loading conditions AE signals associated with Trend 2 were of greater amplitudes, compared with the other groups of signals in the tests, which is favourable to more accurate timing measurements using the first threshold crossing method. Furthermore, superior 1D location accuracy was also observed for the group of signals in Trend 1 as shown in Figure 5-3, which strongly suggests their viability in reliably locating fatigue crack damage. These findings are somewhat contrary to the common notion that AE signals produced during the lower 60% of the loading range are mainly of the continuous type and considered as 'noise' [46; 55].

7.4 Effects of loading parameters and geometry

The effects of loading parameters and geometry of samples in the various tests are summarised in Table 7.1 in terms of the averaged total number of AE signals recorded for periods of crack growth corresponding to the stages in AE generation from fatigue crack growth in SEN samples as described in page 85 and presented in Figure 4-21. Stage 1 was considered to be for crack lengths less than 20 mm, Stage 2 for crack lengths between 20 – 55 mm, Stage 3 was between 55 – 70 mm and subsequent crack growth leading to final failure for Stage 4. Comparisons were made against the averaged total AE Hits obtained

in the Tests 1 to 7 performed with a nominal stress range of 52.2 MPa and stress ratio of 0.1 on SEN samples.

In the case of MT samples, comparisons were made in the averaged total number of AE signals recorded for crack growth at lengths less than 20 mm, designated 'Stage 1' in Table 7-2, and for subsequent growth leading to final failure which was designated 'Stage 2' in Table 7-2. The nominal loading configuration was considered to be a stress range of 52.2 MPa and stress ratio of 0.1.

Table 7.2: Summary of the effects of loading parameters and sample geometry on AE generation from fatigue crack showing the averaged total AE signals for different periods of crack growth

Load parameter	Geometry	Stage 1 (10-20) mm	Stage 2 (20-55) mm	Stage 3 (55-70) mm	Stage 4
Nominal ($\Delta\sigma$=52.2 MPa; R=0.1)	SEN	12852	2796	2203	4524
Reduced stress range	SEN	162894	243425	7650	4655
Increased stress ratio	SEN	264	1862	964	
Variable amplitude loading	SEN	264	1862	964	
Nominal ($\Delta\sigma$=52.2 MPa; R=0.1)	MT	1392	3320		
Reduced stress range	MT	417026	29677		

Reduction of stress range from the nominal value of 52.2 MPa at a constant stress ratio of 0.1 brought about a marked increase in the AE Hit rates for the majority of crack growth in both cases of SEN and MT samples. For Tests 12 to 14 performed on SEN samples with a reduced stress range of 27 MPa and stress ratio of 0.1, an increase by a factor of 12 and 87 respectively for Stages 1 and 2 was observed compared to the averaged total AE Hits at similar lengths of crack growth in Tests 1 to 7. This increase was mainly observed for the AE signals associated with Trend 1 in the distribution of AE signals with applied

load, as shown in Figure 7-4 Figure 4-21 where it can be seen that the hit rates at every given crack length for the AE signals associated with Trend 1 varied by less than a factor of 1, in comparison to the data recorded across the entire loading range. This behaviour can be expected, as the applied stress range is reduced and consequently the crack opening displacement, there would be greater propensity for the fracture surfaces to come into contact under fatigue loading at a constant stress ratio.

For Stages 3 and 4 in Tests 12 to 14, the averaged total AE Hits were more comparable with an increase by a factor of 3 in Stage 3 and almost identical values observed in Stage 4.

Similar increase was also observed for Test 15 performed on an MT sample with reduced stress range of 27 MPa and stress ratio of 0.1. For crack lengths less than 20 mm the averaged total AE hits was seen to increase by a factor of 299. As can be seen in Figure 4-69 Figure 4-70 which shows the distribution of AE signals with applied load, the vast majority AE signals in this period of crack growth were generated below 60% of the maximum stress in the loading range; this finding is also agreeable to the calculated normalised crack opening stress which was 53% for a maximum stress of 30 MPa. Therefore, the increase in AE signals at these crack lengths can be attributed to the prevalence of crack closure effects.

For subsequent crack growth until final failure significantly fewer AE signals were recorded compared with the preceding period of crack growth. Nonetheless, in comparison to similar periods of crack growth in Tests 13 and 14, an increase by a factor of 8 was observed.

An increase in the stress ratio to 0.5 in Test 16 performed on an SEN sample brought about a decrease in the total number of AE Hits by a factor of 4 compared to the averaged total AE Hits in Tests 1 to 7. The major difference was seen in the previously observed AE signals associated with Trend 1 in the distribution of AE signals with applied load which were completely absent in the case of Test 16, as can be seen in Figure 4-71 Figure 4-72. These findings are in line with previous observations for tests performed with stress ratio of 0.1, because as the stress ratio is increased and consequently the crack opening displacement, there would be less propensity for the fracture surfaces to come into contact under fatigue loading.

The outcome of Test 18 performed on an SEN sample under variable amplitude

loading was quite similar to Test 16 performed with stress ratio of 0.5 in terms of the absence of AE signals produced that are nominally classified as 'Trend 1'. It should be noted that the FALSTAFF spectrum used in Test 18 was formatted to suit the load capacity of the test machine, described in Section 3.2.2, and as a result the stress ratio of the load cycles was increased compared with the original form of the spectrum. Figure 3-7 illustrates the Rain-flow count for one sequence of the formatted FALSTAFF load spectrum where it can be seen that the majority of stress cycles had a stress ratio of about 0.7.

In Table 7-2, it can be seen that the averaged total AE Hits in Stages 1 to 3 was less than those observed in Tests 1 to 7, under nominal load conditions, by a factor of 1168, 11 and 2 respectively, while an increase was observed in Stage 4 by a factor of 2.

The effect of a change in sample geometry from SEN to MT was not very clear in the tests performed with stress range of 52.2 MPa. However, for the tests performed with reduced stress range of 27 MPa much clearer distinctions can be made because many more AE signals appeared to be generated. The main difference can be seen in the almost complete absence of AE signals generated from crack lengths between 20 mm until just before final failure in the MT samples, compared with those for SEN samples. A complete explanation for this difference in behaviour is not known.

7.5 Novel approach for fatigue crack length estimation

A new approach for fatigue crack growth prediction was developed based on the characteristics of Trend 1 observed in Tests 1 to 7, illustrated in Figure 4.49, where the AE signals were seen to be generated at increasingly reduced levels of applied load with crack growth. It relates the average normalised loads at which AE signals occur in the loading range with crack growth.

The first step in this process was performed by normalising the values of stress for all the detected AE signals in Tests 1 to 7 for crack lengths between 20 – 80 mm.

A linear best-fit model was determined for the combined AE data for Tests 1 to 7 and the results are show in Figure 7-7, with indications of 95% upper and

lower confidence limits. This clearly captures the trend of AE signals occurring at increasingly reduced loads with increasing crack length as observed in the tests performed on the SEN samples.

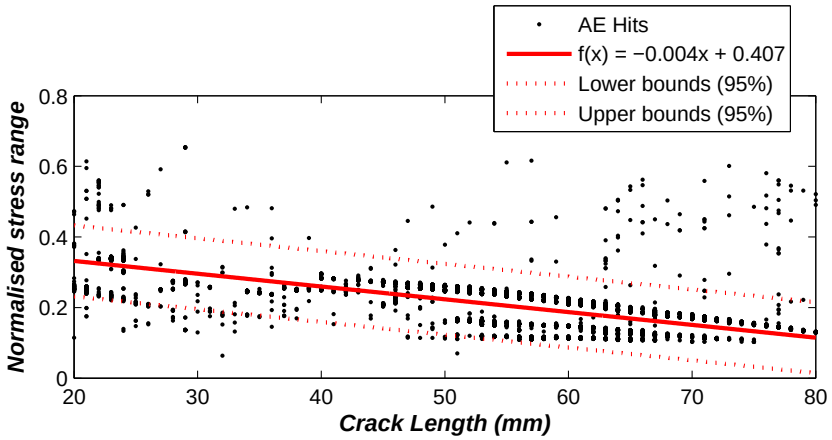

Figure 7.7: AE Hits occurring in normalised stress cycles at various crack lengths

The derived model was compared against AE data recorded in Tests 12 and 14 performed on SEN samples, despite being conducted with a stress range of 27 MPa and stress ratio of 0.1. This was performed using Equation 7-7 which is the inverse expression for the derived linear model. The input variable of normalised stress range as an average of the stress values at which the AE signals occur in the nominal region of Trend 1, which is in the lower 66% of the stress range, as expressed in Equation 7-8, for the period of crack growth under consideration.

$$\alpha = \frac{ML(i) - 0.407}{-0.004} \tag{7.7}$$

And,

$$ML(i) = \frac{1}{n}\left[\sum_{x=1}^{n} L(x;l)_i\right] \cap l < q \tag{7.8}$$

Where,

a - *Estimated crack length*
ML - *Averaged load*
n - *AE signal index*
L - *Measure load*
a - *66% of maximum stress range*

The results of this process performed on AE data recorded by the various sensor pairs are shown in Figure 7-8, where a close agreement between the derived model and the calculated data points can be seen, particularly for Test 12, with the majority of calculated data points located within the confidence bounds, although there were a few outliers.

A comparison of the estimated crack lengths with the actual crack for the various sensor location groups and the results are shown Figure 7-9. It can be seen that identical estimates are obtained for AE data monitored by different location groups in a test sample. The errors in each of these estimates were calculated and shown in Figure 7-10, where errors of less than 5 mm were obtained for both location groups in Test 12, although larger errors up to 20 mm were obtained for crack lengths up to 28 mm. On the other hand, larger errors up to 20 mm were obtained for both sensor location groups in Test 14.

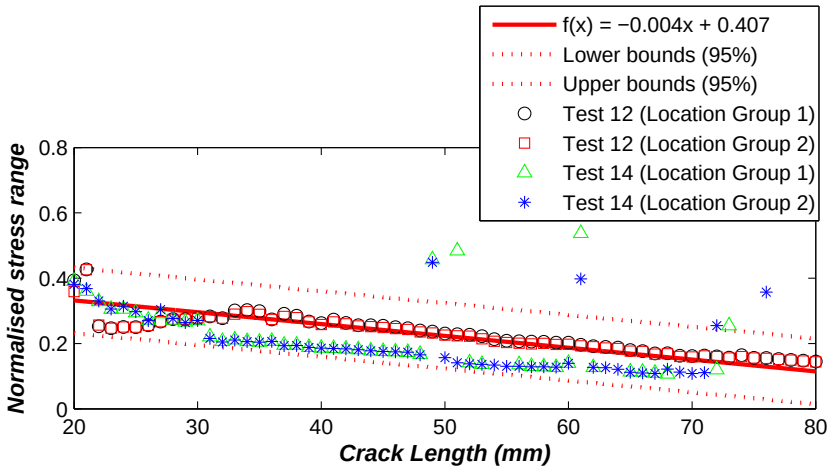

Figure 7.8: Comparison of the averaged normalised stress where AE signals are generated for Tests 12 and 14 with the derived linear model from Tests 1 to 7

This proposed approach for fatigue crack length estimation is highly dependent on the loading configuration as well as geometry of the subject component, thereby limiting its range of application. In the case of the model derived in this work, it would be only be applicable to cases of cracks emanating from the edge of thin samples under tensile loading.

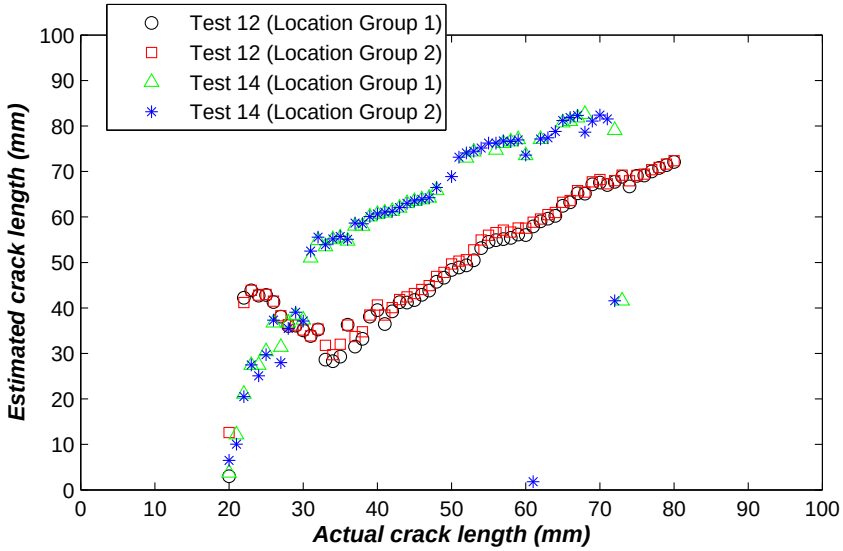

Figure 7.9: Crack length estimation using derived model

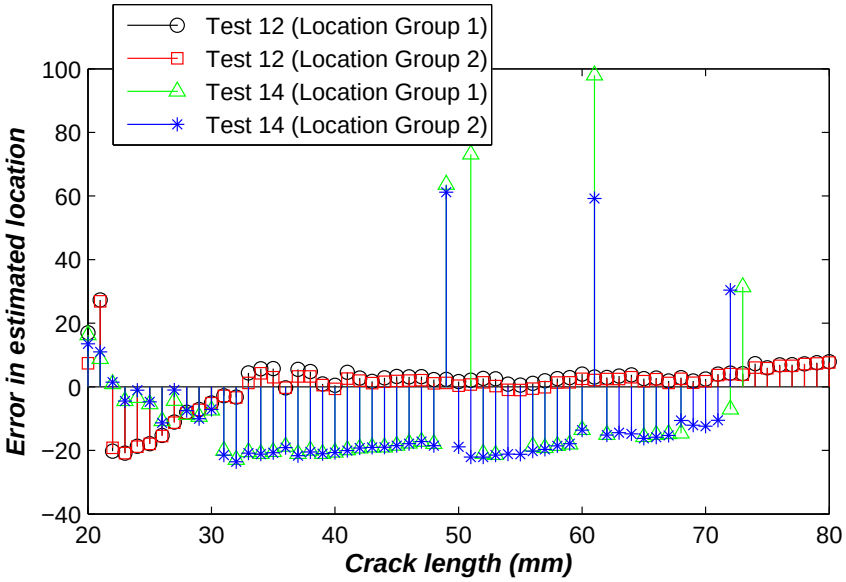

Figure 7.10: Errors in crack length estimation using derived model at various crack lengths

Prognostic methods are either physics-based where the accuracy of predictions is a function of the level of understanding of the underlying physical principles or data-driven, where the accuracy of predictions is a function of the amount or quality of data utilised. The model derived in this thesis is data-driven and can benefit from more using more data which would minimise errors obtained in crack length estimates. Also, modifications can be made such as deriving

a nonlinear model or perhaps incorporating methods such as a Kalman filter which can be used to determine a statistically optimal estimate of the underlying state of a time-dependent system [111].

7.6 AE system installation in realistic structures

Installing an AE system to perform structural health monitoring tasks in a realistic structure would imply very restricted or no access to it and the reliability of the system during operation needs to be known before hand. The fatigue processes underlying AE generation during crack growth in the structural component of interest is a significant factor that would influence the output of the AE system. The behaviour of AE signals generated in a structural component can be characterised but may change after assembly with other structural components, for example in terms of their propagating wave velocities.

During the tests performed on the wing-box structure, it was observed that wave velocity property in the assembled structure was significantly different from that obtained for the aluminium spar alone. This was expected given the change in geometry with the combined thickness of the spar and skin. The wave velocity of AE signals propagating in the representative wing-box structure was characterised using an acousto-ultrasonic method and the value obtained was used to detect and locate the 'hidden' fatigue crack source.

Comparing the peak in each of the distributions with the position of the actual crack, the location accuracy was found to be within 6 mm in Test 1, shown in Figure 6-1, and 24 mm in Test 2, as shown in Figure 6-5. The NDI results verified that the other holes had not developed fatigue cracks, apart from Hole 9 which showed a crack-like indication with the Eddy Current technique, which could not be confirmed using the ultrasonic and fluorescent penetrant methods.

The application of a standard aerospace sealant between them would have undoubtedly contributed in matching their acoustic impedance (ratio of acoustic pressure to acoustic volume flow [112]) which is generally higher for fluid media compared with air and aided AE signal coupling between the components. This behaviour was even more evident in the fact that AE signals generated from the crack on the test spar were detected by a pair of sensors on an adjacent spar, which strongly suggests AE signal coupling between the spar and skin

as well as transmission across the skin. This led to the possibility of performing 2D planar location of the seeded fatigue crack in a complex 3D structure, which shows some potential for global area monitoring with a reduced sensor set based on the transmission path characteristics of the structure. The accuracy of such a system would however be greatly dependent on the accuracy in estimating the wave velocity of the different materials in the propagation path.

Demonstration of such capability of the AE technique in wide area coverage in a complex 3D structure was not been encountered in available literature. This forms another unique aspect of this thesis, where the currently known capability of such a popular technique has been extended with validated results.

Also, in realistic structures there is the possibility of several AE sources being present in a particular region of interest. Principal Component Analysis (PCA) alongside k-means clustering can be used in performing AE signal discrimination as described in Sections 2.4.3.1 and 2.4.3.2 respectively. These methods were applied to AE data from different sources in coupon samples as a function of their propagation distances; it was found that the distance travelled by the signal had a significant effect on the outcome of their classification. This observation was made in the case where AE signals generated from PLBs performed at distributed locations across the area of test samples with different sensor locations as shown in Figure 5-9. It was found that although the signals were produced from the same source type, there was visible separation between the signals as a function of the different sensor configurations.

Performing this analysis on data recorded by a single sensor reduced this effect as suggested in Eaton et al. (2011) [113]. This can be seen in Figure 5-11 where AE signals from PLBs with different propagation distances to a sensor at fixed location showed even visible separation between the different groups.

However it was also found that the ability of this method to correctly distinguish between AE signals from different sources is more sensitive to the effects of propagation distances than the inherent characteristics of different AE sources. This observation was made in the instance where AE signals generated from Pencil Lead Breaks (PLBs) performed across the span of the test machine grip location and those from test machine grip fretting against the sample was analysed, as presented in Figure 5-13 and Table 5-2. It was observed that an error of 39% was obtained in correctly classifying the AE signals from PLBs compared to the case where the same sources of AE signals were considered with different propagation distances and no classification

errors were found. Similar observations were made in other cases considering AE signals from PLBs and fatigue crack growth as shown in Figure 5-12Figure 5-14 as well as Table 5-1 Table 5-3 were errors up to 61% were found. This behaviour diminishes the effectiveness of PCA for AE source classification.

Chapter 8

Conclusions and Contributions

1. There was significant variation in AE Hit rates at particular crack lengths across different samples in tests performed under nominally identical conditions. In a series of 7 tests the cumulative number of AE signals detected during crack growth between crack lengths of 10 - 20 mm varied from 0 - 36362. The POH metric developed can be used to quantify the reliability of fatigue crack detection in potential SHM installations.

2. Common trends could be identified in almost all samples. There was significant variation in AE Hit rates with crack growth. The mean number of AE signals detected from the onset of crack growth up to a length of 25 mm was as high as 1600 AE Hits/mm but rapidly declined to less than 30 AE Hits/mm until a crack length of 55 mm where they were up to 120 AE Hits/mm for subsequent growth until final failure. This has implications of periods of crack growth with significantly reduced opportunity of crack detection in potential SHM applications.

3. For particular periods of crack growth a reduction in applied stress range resulted in an increase in AE Hit rates by a factor of 12, increase in stress ratio resulted in a reduction by a factor of 9 and a change in sample geometry resulted in an increase by a factor of 32. All of these observations are consistent with changes in crack closure effects. This has implications on the loading and geometric conditions necessary for optimal use of the AE technique in SHM applications.

4. Analysis of AE Hit distribution with applied load showed that the majority of AE signals generated during fatigue crack growth are produced in the lower two-thirds of the stress range and can be associated with crack closure. Changes in loading and sample geometry parameters brought about corresponding changes in the intensity of this group of signals. Time of flight location estimates showed that they occurred both at the crack tip and crack mouth. This demonstrates the added potential of loads monitoring alongside AE monitoring for fatigue crack damage diagnosis.

5. Similar analysis of AE Hit distribution with applied load showed that the group of AE signals produced close to the maximum stress are dependent on the turning points of the stress cycles rather than particular maximum values of stress.

6. A new approach for fatigue crack length estimation based on monitoring loads corresponding with AE signal generation has been developed. Predictions can be obtained with increasing performance with errors of 80% at crack lengths around 25 mm and less than 10% at crack lengths around 80 mm. This significantly extends the capability of the AE technique in performing prognostics where remaining useful life estimates of a component can be obtained.

7. The amplitudes of the signals associated with crack closure were greater than those of the other signals produced in the tests and as a result more superior accuracy in location estimation can be achieved with errors less than 30 mm at 90% cumulative, compared to the locations errors obtained with the AE signals occurring close to the maximum of the load cycles which was 68 mm at 90% cumulative frequency, using the first threshold crossing method for signal detection.

8. AE signal classification based on the Principal Components Analysis (PCA) and k-means clustering is more sensitive to signal propagation distance than differences in inherent characteristics of the AE signals generated from different sources, which can lead to classification errors up to 60%.

9. The AE technique was able to detect and locate a 'hidden' fatigue crack in complex wing-box structure with 1D location accuracy between 6 – 24 mm.

10. The 2D location estimates of the 'hidden' fatigue crack demonstrated the feasibility of exploiting complex propagation paths of AE signals in intricate structures to enable wide area sensing coverage with a reduced sensor set. The accuracy was found to be within 50 mm of the distribution peak in location estimates.

Future Work

The work done in this thesis should be extended to other materials, sample geometries and loading configuration to establish the effects of such changes on AE generation and consequently the reliability of the AE technique. Also, development of finite element modelling approaches alongside experiments for even further understanding of the AE signal propagation and detection process. This can be used to characterise the reliability of the AE technique for sensors positioned at different locations which can inform the optimal choice in a particular installation.

Appendix A

Survey of SHM Techniques

Structural Health Monitoring (SHM) is the process of implementing continuous or on-demand diagnosis of structural integrity as well as damage detection via permanently installed sensors. This is an enabler for condition based maintenance where a structure is only taken out of service when repair and maintenance is needed hence eliminating costly and unnecessary precautionary inspections. The potential benefits include reduced maintenance cost, as well as minimising errors due to human factors by using automated sensing data acquisition and analysis. The benefits of SHM can be valuable in several industries including civil, aerospace, marine and transport, where safety and reliability is essential. This scope of this thesis is however focused on the aerospace sector.

Significant research effort in SHM has been devoted to aerospace structures over the last 30 years [114]. As a result, a plethora of techniques with various levels of capability have been developed. A majority of the SHM techniques have overlapping underlying principles, methods of implementation and signal processing techniques. The pyramid structure for classifying SHM techniques, shown below, is used to derive a representative snapshot of the state of SHM techniques with clear distinction between them.

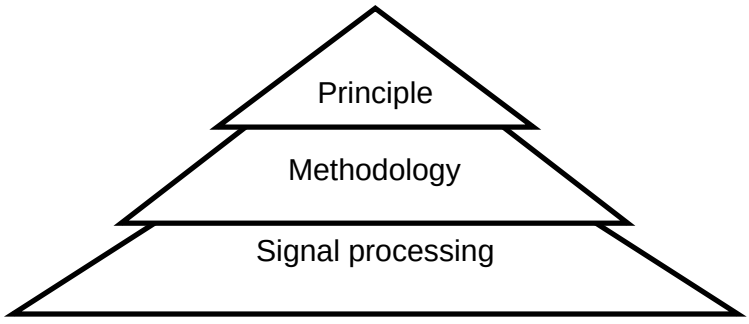

Figure A.1: Pyramid for SHM techniques classification

As Figure A-1 illustrates with its narrow tip, there is a limited set of principles which SHM techniques are derived from and significantly more methods of implementation and signal processing operations applied based on these set

of principles. The clearest distinction between SHM techniques can be seen at the principle level which can be broadly classified as: stress and ultrasonic waves, vibration, impedance and continuity measurements.

Stress and ultrasonic waves-based techniques use a variety of methods to generate guided waves which either inherently carry structural state signatures or interact with structural features and defects to give structural health information [22-28; 115; 116]. Vibration-based techniques on the other hand, correlates a structures vibration response to the presence of damage [117; 118], while impedance sensors use impedance measurements and continuity sensors measure a break in continuity of a sensing parameter to correlate with failure modes [119-124]. A selection of popular SHM techniques classified according to their underlying physical principle is outlined in Figure A-2.

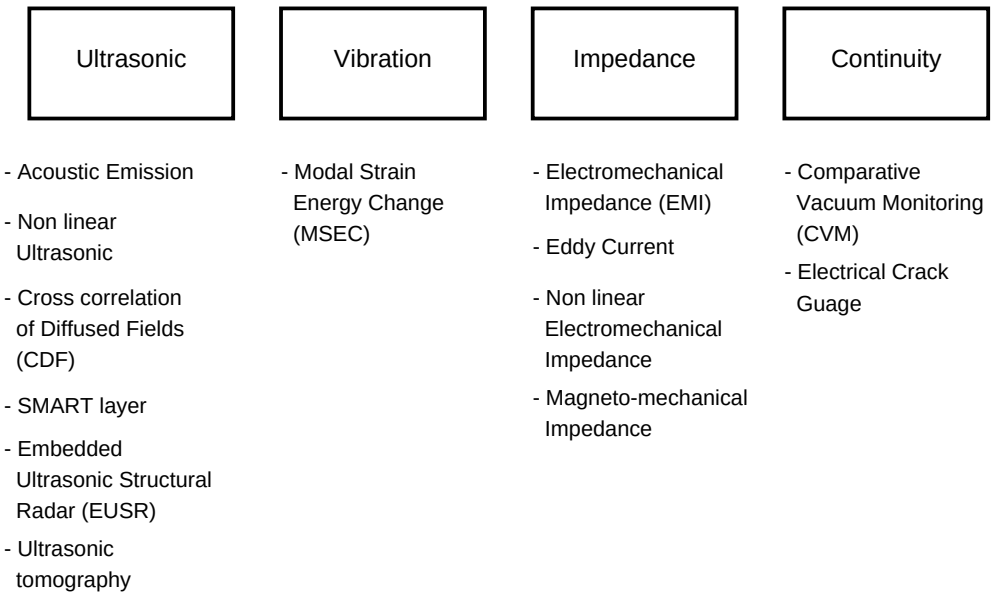

Figure A.2: A selection of SHM technique classified in terms of underlying physical principle

A qualitative study was performed to compare the performance of the collection of SHM techniques shown in Figure 2.18 based on a set of criteria for effective operation in aerospace applications which are highlighted below;

- ***Accuracy:*** The capability of derived parameters to characterize damage in terms of size (percentage variation) and location (mm) with a certain degree of confidence will be factors considered for this criterion; establishing the relationship between damage progression and the acquired parameter.

- ***Sensitivity:*** This criterion is assessed based on the smallest detectable defect size (mm), type and the availability of associated probabilities of detection (POD) for a range of defect sizes. In the case of POD, scores are awarded in a binary fashion; maximum scores will be awarded to the techniques with POD curves available and minimum scores awarded otherwise.
- ***Weight, volume and sensor density:*** Savings in this context could potentially translate into savings in fuel costs or perhaps freeing-up physical space, creating allowance for other purposes. Estimated weight (Kg), volume (mm3) and sensor density (sensor/m2) for sensing and data communication techniques are considered for this criterion. In the case of communication media, scores are awarded in a binary fashion; maximum scores will be awarded to the techniques with wireless media and minimum scores awarded for wired media.

The results of the survey are given in Table 2.1 which shows values of reported performance of the techniques considered. Where information was unavailable the fields were left blank. It can be seen from the results that the majority of techniques are sensitive to damage sizes less than 1 mm. This would be considered excellent by the standards of current NDT operations, and bodes well for the eventual use of any of these approaches to damage detection in a health monitoring or prognostic application.

Also it can be seen that, with the exception of sensitivity to defects, there is a lack of quantitative information on the other aspects of performance considered; indicating a lopsided trend of development in SHM techniques. Information on their POD is especially important as this metric is used to characterise and certify NDT techniques in aerospace applications. The Eddy Current and Comparative Vacuum Gauge techniques were however observed to have the most comprehensive quantitative information and the Cross-correlation of Diffuse Fields technique was the least documented.

Acoustic emission by virtue of its maturity has some data available but is notably deficient in POD or equivalent metric of representing the techniques performance. This void can be filled by understanding and characterizing the variability in obtaining and processing measurements; which will give values of confidence that can be expressed in probability densities. The acoustic emission technique was hence chosen as the main focus of this thesis.

Table A.1: Summary of the reported performance of SHM techniques

Monitoring Techniques	**Sensitivity (mm)**	**POD (mm)**	**Location accuracy (mm)**
Acoustic Emission (AE)	0.55 [101]	Unavailable	14 [27]
Guided ultrasonic	0.3 [125]	0.3 [125]	Unavailable
Non linear ultrasonic	0.5 [126]	Unavailable	Unavailable
Cross-correlation of Diffuse Fields (CDF)	0.63 [127]	Unavailable	Unavailable
Embedded Ultrasonic Structural Radar (EUSR)	1.57 [128]	Unavailable	Unavailable
Modal Strain Energy Change (MSEC)	6 [129]	Unavailable	Unavailable
Electro-Mechanical Impedance (EMI)	5 [130]	Unavailable	Unavailable
Eddy Current	0.25 [119]	2 [131]	
Comparative Vacuum Monitoring (CVM)	0.58 [120]	0.58 [120]	Unavailable

Appendix B

Tensile Tests

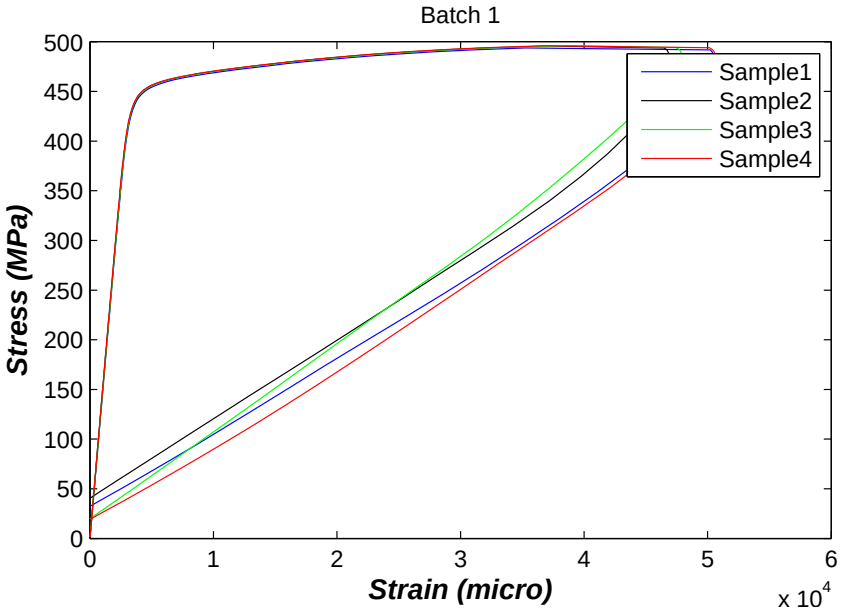

Figure B.1: Stress-strain curve for samples from Batch 1 material

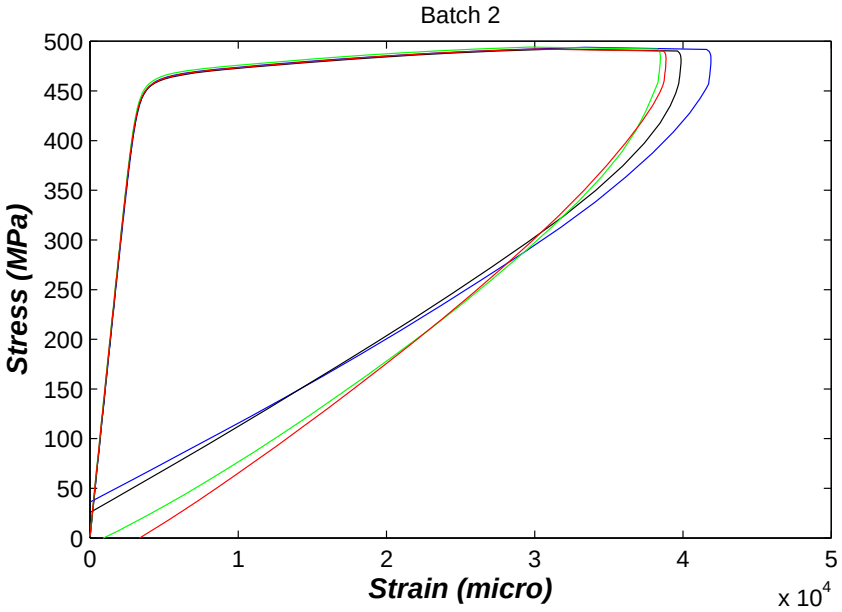

Figure B.2: Stress-strain curve for samples from Batch 2 material

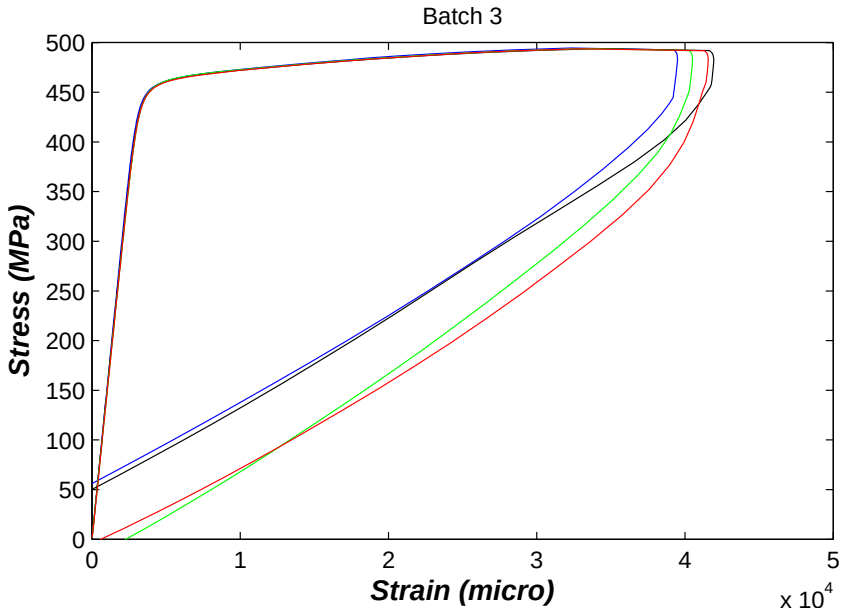

Figure B.3: Stress-strain curve for samples from Batch 3 material

Appendix C

Crack growth data

Test 1		Test 2		Test 3	
Crack length (mm)	Cycles	Crack length (mm)	Cycles	Crack length (mm)	Cycles
11	11682	11	17882	11	11751
12	16722	12	26382	12	18351
13	20442	13	34081	13	25671
14	24522	14	41081	14	30591
15	28002	15	45482	15	35391
16	31722	16	49282	16	40191
17	34962	17	53282	17	44991
18	37962	18	59282	18	47991
19	40482	19	64082	19	51591
20	42882	20	68282	20	54111
21	45402	21	70682	21	57111
22	47922	22	74282	22	59631
23	49842	23	77281	23	62631
24	51762	24	80393	24	65031
25	53562	25	82793	25	67551
26	55122	26	85193	26	69351
27	57042	27	87882	27	71391
28	58842	28	90282	28	72951
29	60402	29	92183	29	74271
30	61482	30	94583	30	75471
31	62202	31	95783	31	76571
32	63042	32	98183	32	77871
33	64122	33	99983	33	79071
34	65442	34	101183	34	80221
35	66282	35	102383	35	81171
36	67242	36	103383	36	82071
37	68082	37	104283	37	83121
38	68442	38	104923	38	84021
39	68922	39	105553	39	84871
40	69522	40	106163	40	85671
41	70122	41	106763	41	86121
42	70602	42	107443	42	86501
43	71202	43	108043	43	86881
44	71562	44	108403	44	87191
45	72042	45	108883	45	87471
46	72402	46	109343	46	88221
47	72642	47	109783	47	88871
48	73002	48	110243	48	89471
49	73362	49	110703	49	89971
50	73602	50	111043	50	90471
51	73842	51	111333	51	91388
52	74082	52	111573	52	92238

53	74322	53	111813	53	92988
54	74442	54	112013	54	93328
55	74702	55	112273	55	93589
56	74922	56	112493	56	93709
57	75062	57	112633	57	93969
58	75262	58	112833	58	94189
59	75382	59	112953	59	94329
60	75522	60	113093	60	94529
61	75682	61	113253	61	94649
62	75802	62	113373	62	94789
63	75922	63	113493	63	94949
64	76042	64	113613	64	95069
65	76142	65	113713	65	95189
66	76182	66	113753	66	95309
67	76362	67	113933	67	95409
68	76402	68	113973	68	95589
69	76442	69	114013	69	95629
70	76522	70	114093	70	95669
71	76602	71	114173	71	95749
72	76642	72	114213	72	95829
73	76722	73	114293	73	95869
74	76762	74	114333	74	95949
75	76802	75	114373	75	95989
76	76850	76	114421	76	96029
77	76890	77	114461	77	96077
78	76930	78	114501	78	96117
79	76962	79	114533	79	96157
80	76982	80	114553	80	96189
81	77010	81	114581	81	96209
82	77034	82	114605	82	96237
83	77062	83	114633	83	96261
84	77082	84	114653	84	96289
85	77102	85	114673	85	96309
86	77122	86	114693	86	96329
87	77142	87	114713	87	96349
88	77158	88	114729	88	96369
89	77170	89	114741	89	96385
90	77190	90	114761	90	96397
91	77198	91	114769	91	96417
92	77206	92	114777	92	96425
93	77214	93	114785	93	96433
94	77226	94	114797	94	96441
95	77234	95	114805	95	96453
96	77242	96	114813	96	96461

98	77250	98	114821	98	96469
100	77258	100	114829	99	96477
102	77266	102	114837	100	96485
106	77278	106	114849	102	96493
112	77286	112	114857	106	96505
118	77294	121	114865	111	96513
				115	96523

Test 4		Test 5		Test 6	
Crack length (mm)	Cycles	Crack length (mm)	Cycles	Crack length (mm)	Cycles
11	8209	11	12001	11	21353
12	13249	12	17521	12	26393
13	16969	13	22681	13	30113
14	21049	14	25801	14	34193
15	24529	15	28441	15	37673
16	28249	16	32041	16	41393
17	31489	17	35161	17	44633
18	34489	18	37681	18	47633
19	37009	19	40201	19	50153
20	39409	20	42481	20	52553
21	41929	21	44041	21	55073
22	44449	22	46441	22	57593
23	46369	23	48121	23	59513
24	48289	24	49561	24	61433
25	50089	25	51361	25	63233
26	51649	26	52681	26	64793
27	53569	27	53881	27	66713
28	55369	28	54481	28	68513
29	56929	29	56041	29	70073
30	58009	30	57001	30	71153
31	58729	31	58441	31	71873
32	59569	32	59161	32	72713
33	60649	33	60241	33	73793
34	61969	34	60601	34	75113
35	62809	35	61561	35	75953
36	63769	36	62161	36	76913
37	64609	37	63001	37	77753
38	64969	38	63361	38	78113
39	65449	39	63961	39	78593
40	66049	40	64321	40	79193
41	66649	41	65401	41	79793
42	67129	42	65761	42	80273
43	67729	43	66121	43	80873

44	68089	44	66361	44	81233
45	68569	45	66721	45	81713
46	68929	46	67201	46	82073
47	69169	47	67441	47	82313
48	69529	48	67681	48	82673
49	69889	49	67921	49	83033
50	70129	50	68161	50	83273
51	70369	51	68401	51	83513
52	70609	52	68521	52	83753
53	70849	53	68881	53	83993
54	70969	54	69001	54	84113
55	71229	55	69121	55	84373
56	71449	56	69241	56	84593
57	71589	57	69361	57	84733
58	71789	58	69481	58	84933
59	71909	59	69601	59	85053
60	72049	60	69721	60	85193
61	72209	61	69841	61	85353
62	72329	62	69961	62	85473
63	72449	63	70081	63	85593
64	72569	64	70201	64	85713
65	72669	65	70321	65	85813
66	72709	66	70441	66	85853
67	72889	67	70501	67	86033
68	72929	68	70561	68	86073
69	72969	69	70681	69	86113
70	73049	70	70751	70	86193
71	73129	71	70801	71	86273
72	73169	72	70861	72	86313
73	73249	73	70921	73	86393
74	73289	74	70961	74	86433
75	73329	75	71011	75	86473
76	73377	76	71051	76	86521
77	73417	77	71091	77	86561
78	73457	78	71131	78	86601
79	73489	79	71161	79	86633
80	73509	80	71221	80	86653
81	73537	81	71251	81	86681
82	73561	82	71281	82	86705
83	73589	83	71301	83	86733
84	73609	84	71311	84	86753
85	73629	85	71331	85	86773
86	73649	86	71351	86	86793
87	73669	87	71371	87	86813

88	73685	88	71391	88	86829
89	73697	89	71399	89	86841
90	73717	90	71411	90	86861
91	73725	91	71421	91	86869
92	73733	92	71431	92	86877
93	73741	93	71441	93	86885
94	73753	94	71451	94	86897
95	73761	96	71461	95	86905
96	73769	98	71471	96	86913
98	73777	100	71481	98	86921
100	73785	103	71491	100	86929
102	73793	106	71501	102	86937
106	73805	112	71510	106	86949
112	73813			112	86957
121	73821			121	86965

Test 7			
Crack length (mm)	Cycles	Crack length (mm)	Cycles
11	4942	55	72170
12	9442	56	72290
13	13642	57	72510
14	17642	61	73110
15	21242	62	73270
16	24742	63	73390
17	28042	64	73510
18	31042	65	73630
19	34042	66	73730
20	36562	67	73910
21	38962	68	73950
22	41482	69	73990
23	43782	70	74070
24	45882	71	74150
25	47782	72	74190
26	49382	73	74270
27	50982	74	74310
28	52382	75	74350
29	53702	76	74398
30	54902	77	74438
31	56002	78	74478
32	57202	79	74510
33	58352	80	74530
34	59352	81	74558
35	60302	82	74582

36	61202	83	74610
37	62102	84	74630
38	62952	85	74650
39	63652	86	74670
40	64252	87	74690
41	64702	88	74706
42	65082	89	74718
43	65462	90	74738
44	65772	91	74746
45	66052	92	74754
46	66802	93	74762
47	67452	94	74774
48	68052	95	74782
49	68552	96	74790
50	69052	98	74798
51	69969	99	74806
52	70819	100	74814
53	71569	102	74826
54	71909	106	74834
58	72650	114	74844
59	72850		
60	72970		

Test 12		Test 13		Test 14	
Crack length (mm)	Cycles	Crack length (mm)	Cycles	Crack length (mm)	Cycles
12	277669	13	31709	12	76560
13	336709	14	90749	13	158280
14	378949	15	132989	14	210613
15	414469	16	168509	15	254893
16	443989	17	198029	16	286573
17	465829	18	219869	17	317893
18	488629	19	242669	18	344773
19	508909	20	262949	19	367093
20	521749	21	275789	20	383293
21	538549	22	292589	21	395293
22	552229	23	306269	22	417613
23	562189	24	316229	23	431533
24	576589	25	321569	24	443533
25	586669	26	332069	25	457333
26	598069	27	343229	26	472573
27	606949	28	353669	27	484813
28	617935	29	363989	28	489733
29	624175	30	372149	29	495853

30	632335	31	379349	30	507253
31	639535	32	387629	31	514333
32	646495	33	393749	32	521533
33	653815	34	401981	33	530773
34	660175	35	407517	34	534973
35	665335	36	412957	35	541093
36	671335	37	420093	36	546253
37	677455	38	425645	37	550333
38	681775	39	431981	38	555493
39	685255	40	436429	39	561613
40	690535	41	439773	40	565333
41	695935	42	444045	41	571813
42	700015	43	448829	42	575053
43	704455	44	453309	43	580093
44	706615	45	457293	44	582733
45	710575	46	460333	45	587173
46	713815	47	464045	46	589813
47	716695	48	467805	47	593413
48	720895	49	471133	48	596773
49	724015	50	474765	49	600253
50	727015	51	477373	50	603253
51	729775	52	479421	51	605773
52	732415	53	482893	52	607933
53	734575	54	485533	53	610813
54	738055	55	487965	54	612973
55	740095	56	490189	55	615373
56	742135	57	492541	56	617773
57	743695	58	494237	57	620053
58	746215	59	496189	58	621853
59	747895	60	498045	59	624253
60	749815	61	499949	60	625813
61	751015	62	501533	61	627133
62	752935	63	503117	62	628733
63	754615	64	504701	63	630342
64	755850	65	506205	64	631782
65	757085	66	507661	65	633422
66	758320	67	508989	66	634662
67	759557	68	510221	67	636022
68	760997	69	511165	68	637062
69	762405	70	512525	69	638422
70	763333	71	513629	70	639622
71	764229	72	514573	71	640822
72	765413	73	515405	72	642102
73	766405	74	516365	73	642902

74	767333	75	517293	74	643942
75	768325	76	518221	75	644782
76	769061	77	519053	76	645542
77	769893	78	519821	77	646262
78	770437	79	520365	78	646942
79	771237	80	521069	79	647582
80	771973	81	521501	80	648142
81	772517	82	521965	81	648782
82	773061	83	522573	82	649422
83	773573	84	523245	83	649942
84	773989	85	523661	84	650622
85	774629	86	524077	85	651222
86	775045	87	524525	86	651502
87	775525	88	524941	87	652002
88	776005	89	525437	88	652502
89	776357	90	525693	89	652595
90	776645	91	526077	90	652835
91	777029	92	526285	91	653107
92	777349	93	526685	92	653427
93	777669	94	526877	93	653779
94	777893	95	527165	94	654019
95	778149	96	527517	95	654211
96	778437	97	527725	96	654451
97	778757	98	527901	97	654643
98	779013	99	528101	98	654931
99	779237	100	528251	99	655043
100	779397	101	528455	100	655283
101	779621	102	528615	101	655411
102	779781	103	528789	102	655555
103	779973	104	528934	103	655715
104	780133	105	529094	104	655859
105	780293	106	529239	105	655971
106	780453	107	529367	106	656099
107	780581	108	529463	107	656227
108	780677	109	529591	108	656339
109	780805	110	529719	109	656403
110	780933	111	529815	110	656515
111	781029	112	529879	111	656595
112	781093	113	529975	112	656707
113	781189	114	530071	113	656771
114	781285	115	530135	114	656851
115	781349	116	530199	115	656915
116	781413	117	530263	116	656979
117	781477	118	530327	117	657043

118	781541	119	530391	118	657091
119	781605	120	530423	119	657139
120	781637	121	530455	120	657171
121	781669	122	530519	121	657219
122	781733	123	530551	122	657251
123	781765	124	530615	123	657299
124	781829	125	530647	125	657347
125	781861	126	530679	126	657363
126	781893	127	530711	127	657395
127	781925	128	530743	128	657411
128	781957	129	530775	130	657459
129	781989	130	530807	131.5	657475
131	782021	131	530839	132.5	657493
133	782053	132	530871	134	657507
135	782085	133	530903	135	657523
138	782117	134	530935	137	657539
153	782149	150	530965	139.5	657555
				143	657571
				150	657587

Test 15 - MT			
Crack length (mm)	Cycles	Crack length (mm)	Cycles
11	15870	48	44380
12	19170	49	44380
13	25380	50	44380
14	30330	51	44380
15	35790	52	44380
16	40440	53	44380
17	44380	54	44380
18	44380	55	44380
19	44380	56	44380
20	44380	57	44380
21	44380	59	44380
22	44380	60	44380
23	44380	61	44380
24	44380	62	44380
25	44380	63	44380
26	44380	64	44380
27	44380	65	44380
28	44380	66	44380
29	44380	67	44380
30	44380	68	44380
31	44380	69	44380

32	44380	70	44380
33	44380	71	44380
34	44380	72	44380
35	44380	73	44380
36	44380	74	44380
37	44380	75	44380
38	44380	76	44380
39	44380	87	44380
40	44380	88	44380
41	44380	89	44380
42	44380	90	44380
43	44380	91	44380
44	44380	92	44380
45	44380	93	44380
46	44380	94	44380
47	44380	96	44380
		104	112617

Test 16			
Crack length (mm)	Cycles	Crack length (mm)	Cycles
12.5	120	51	819280
13	111480	52	824240
14	174960	53	829200
15	240600	54	835440
16	271560	55	839880
17	338640	56	843960
18	381920	57	849120
19	425200	58	854400
20	468480	59	856320
21	511760	60	858720
22	528560	61	860520
23	549560	62	861300
24	578360	63	862080
25	607400	64	862860
26	624933	65	863640
27	642466	66	867720
28	660000	67	869760
29	664920	68	872380
30	669840	69	875040
31	674760	70	876960
32	688200	71	879120

33	697440	72	881280
34	706680	73	883320
35	711720	74	885360
36	723000	75	887160
37	728160	76	889200
38	741240	77	891360
39	744360	78	892784
40	754680	79	894208
41	761760	80	895632
42	768960	81	897056
43	772080	82	898480
44	781440	83	899904
45	787560	84	901328
46	792720	85	902752
47	797880	86	904176
48	803520	87	905600
49	809160	88	907024
50	814320	89	908448
		90	909876

REFERENCES

[1] Stephens R.W.B. and Pollock A.A. (1971), "Waveforms and frequency spectra of acoustic emissions", *Journal of the Acoustical Society of America,* vol. 50, no. 3 pt 2, pp. 904-910.

[2] Holford, K. M. (2000), "Acoustic emission - basic principles and future directions", *Strain,* vol. 36, no. 2, pp. 51-54.

[3] McBride, S. L., MacLachlan, J. W. and Paradis, B. P. (1981), "Acoustic emission and inclusion fracture in 7075 aluminum alloys", *Journal of Nondestructive Evaluation,* vol. 2, no. 1, pp. 35-41.

[4] Rose, J. L. (1999), *Ultrasonic waves in solid media,* First ed, Cambridge University Press, USA.

[5] Tolstoy, I. (1973), *Wave propagation,* First ed, McGraw-Hill, USA.

[6] Egle, D. (1987), "Wave Propagation", in Miller, R. K. and McIntire, P. (eds.) *Non-Destructive Testing Handbook,* Second ed, pp. 91.

[7] Rose, J. L. (2003), "Dispersion curves in guided waves testing", *Mater.Eval.,* vol. 61, no. 1, pp. 20.

[8] Kolsky, H. (1964), "Stress waves in solids", *Journal of Sound and Vibration,* vol. 1, no. 1, pp. 88-110.

[9] Holroyd, T. J. (2000), "Basic Concepts and Theory", in Hunt, T. M. (ed.) *Acoustic Emission and Ultrasonics,* Coxmoor, , pp. 17.

[10] Rose, J. L. (1999), "Waves in Plates", in *Ultrasonic Waves in Solid Media,* Cambridge, , pp. 101.

[11] Rose, J. L. (1999), "Interface Waves", in *Ultrasonic Waves in Solid Media,* Cambridge University Press, , pp. 132.

[12] Haldorsen, J., Johnson, D., Plona, T., Sinha, B., Valero, H. and Winkler, K. (2006), "Borehole Acoustic Emission", vol. 18, no. 1, pp. 33.

[13] Rose, J. L. (1999), "Layer on a half-space", in *Ultrasonic Waves in Solid Media,* Cambridge University Press, , pp. 137.

[14] Love, A. E. H. (1911), *Some Problems of Geodynamics,* Cambridge University Press.

[15] Lord Rayleigh (1885), "On waves propagated along the plane surface of an elastic solid", *Proceedings of the London Mathematical Society,* vol. 17, no. 1, pp. 4.

[16] Ciampa, F. and Meo, M. (2010), "Acoustic emission source localisation and velocity determination of the fundamnetal mode A0 using wavelet analysis and a Newton-based optimisation technique", *Smart Mater.Struct.,* vol. 19.

[17] Gorman, M. R. (1991), "Plate wave acoustic emission", *J.Acoust.Soc.Am.,* vol. 90, no. 1.

[18] Reddy, J. N. (2006), *Theory and Analysis of Elastic Plates and Shells,* Second ed, , London.

[19] H C Kim and, H. K. P. (1984), "Laser interferometry system for measuring displacement amplitude of acoustic emission signals", *Journal of Physics D: Applied Physics,* vol. 17, no. 4, pp. 673.

[20] Liang, S., Zhang, C., Lin, W., Li, L., Li, C., Feng, X. and Lin, B. (2009), "Fiber-optic intrinsic distributed acoustic emission sensor for large structure health monitoring", *Optics Letters,* vol. 34, no. 12, pp. 1858-1860.

[21] Giurgiutiu, V. (2010), "Piezoelectric wafer active sensors for structural health monitoring - State of the art and future directions", *American Society of Mechanical Engineers, Pressure Vessels and Piping Division (Publication) PVP,* Vol. 6, pp. 1115.

[22] Ciampa, F. and Meo, M. (2010), "A new algorithm for acoustic emission localization and flexural group velocity determination in anisotropic structures", *Composites Part A: Applied Science and Manufacturing,* vol. 41, no. 12, pp. 1777-1786.

[23] Gangadharan, R., Prasanna, G., Bhat, M. R., Murthy, C. R. L. and Gopalakrishnan, S. (2009), "Acoustic emission source location and damage detection in a metallic structure using a graph-theory-based geodesic approach", *Smart Materials and Structures,* vol. 18, no. 11.

[24] Jcong, H. J. and Jaiig, Y. -. (2000), "Fracture source location in thin plates using the wavelet transform of dispersive waves", *IEEE transactions on ultrasonics, ferroelectrics, and frequency control,* vol. 47, no. 3, pp. 612-619.

[25] Kirikera, G. R., Shinde, V., Schulz, M. J., Ghoshal, A., Sundaresan, M. and Allemang, R. (2007), "Damage localisation in composite and metallic structures using a structural neural system and simulated acoustic emissions", *Mechanical Systems and Signal Processing,* vol. 21, no. 1, pp. 280-297.

[26] Maji, A. K., Satpathi, D. and Kratochvil, T. (1997), "Acoustic emission source location using lamb wave modes", *Journal of Engineering Mechanics,* vol. 123, no. 2, pp. 154-161.

[27] Baxter, M. G., Pullin, R., Holford, K. M. and Evans, S. L. (2007), "Delta T source location for acoustic emission", *Mechanical Systems and Signal Processing,* vol. 21, no. 3, pp. 1512-1520.

[28] Holford, K. M. and Carter, D. C. (1999), "Acoustic emission source location", *Key Engineering Materials,* vol. 167, pp. 162-171.

[29] Gerberich, W. W. and Hartbower, C. E. (1967), "Some observations on stress wave emission as a measure of crack growth", *International Journal of Fracture Mechanics,* vol. 3, no. 3, pp. 185-192.

[30] Morton, T. M., Harrington, R. M. and Bjeletich, J. G. (1973), "Acoustic emissions of fatigue crack growth", *Engineering Fracture Mechanics,* vol. 5, no. 3.

[31] Roberts, T. M. and Talebzadeh, M. (2003), "Acoustic emission monitoring of fatigue crack propagation", *Journal of Constructional Steel Research,* vol. 59, no. 6, pp. 695-712.

[32] Gong, Z., DuQuesnay, D. L. and McBride, S. L. (1998), "Measurement and Interpretation of Fatigue Crack Growth in 7075 Aluminum Alloy Using Acoustic Emission Monitoring", *Journal of Testing and Evaluation,* vol. 26, no. 6, pp. 567-574.

[33] Moorthy, V., Jayakumar, T. and Raj, B. (1996), "Influence of microstructure on acoustic emission behavior during stage 2 fatigue crack growth in solution annealed, thermally aged and weld specimens of AISI type 316 stainless steel", *Materials Science and Engineering A,* vol. 212, no. 2, pp. 273-280.

[34] Roberts, T. M. and Talebzadeh, M. (2003), "Fatigue life prediction based on crack propagation and acoustic emission count rates", *Journal of Constructional Steel Research,* vol. 59, no. 6, pp. 679-694.

[35] Singh, A. (2002), "The nature of initiation and propagation S-N curves at and below the fatigue limit", *Fatigue and Fracture of Engineering Materials and Structures,* vol. 25, no. 1, pp. 79-89.

[36] Harris, D. O. and Dunegan, H. L. (1974), "Continuous monitoring of fatigue-crack growth by acoustic-emission techniques ", *Experimental Mechanics,* vol. 14, no. 2, pp. 71-81.

[37] Enoki, M., Watanabe, M., Chivavibul, P. and Kishi, T. (2000), "Non-contact measurement of acoustic emission in materials by laser

interferometry", *Science and Technology of Advanced Materials,* vol. 1, no. 3, pp. 157-165.

[38] Daniel C Betz and Graham Thursby and Brian Culshaw and Wieslaw,J.Staszewski (2003), "Acousto-ultrasonic sensing using fiber Bragg gratings", *Smart Materials and Structures,* vol. 12, no. 1, pp. 122.

[39] Rao, Y. J. (1999), "Recent progress in applications of in-fibre Bragg grating sensors", *Optics and Lasers in Engineering,* vol. 31, no. 4, pp. 297-324.

[40] Breckenridge, F. R. and Greenspan, M. (1981), "Surface-wave displacement: Absolute measurements using a capacitive transducer", *Journal of the Acoustical Society of America,* vol. 69, no. 4, pp. 1177-1185.

[41] Ozevin, D., Greve, D. W., Oppenheim, I. J. and Pessiki, S. P. (2006), "Resonant capacitive MEMS acoustic emission transducers", *Smart Materials and Structures,* vol. 15, no. 6, pp. 1863-1871.

[42] Dunegan, H. and Harris, D. (1969), "Acoustic emission-a new nondestructive testing tool", *Ultrasonics,* vol. 7, no. 3, pp. 160-166.

[43] Dunegan, H. L., Harris, D. O. and Tatro, C. A. (1968), "Fracture analysis by use of acoustic emission", *Engineering Fracture Mechanics,* vol. 1, no. 1, pp. 105-110,IN23-IN24,111-122.

[44] Physical Acoustics. (2007), *PCI-2 Based Acoustic Emission System-User's Manual* .

[45] Holford, K.M., (2009), "Acoustic emission in structural health monitoring" *Key Engineering Materials,* vols. 413-414, pp. 15-28

[46] Yu, J. and Ziehl, P. (2011), "Fatigue evaluation and prognosis for steel bridges with remote acoustic emission monitoring", *Structural Health Monitoring 2011: Condition-Based Maintenance and Intelligent Structures - Proceedings of the 8th International Workshop on Structural Health Monitoring,* Vol. 1, pp. 1266.

[47] Miller, R. K. and McIntire, P. (eds.) (1987), *Non-destructive testing handbook,* 2nd ed, American Society for Nondestructive Testing.

[48] *ASTM E2191/E2191M-10 "Standard Practice for Examination of Gas-Filled Filament-Wound Composite Pressure Vessels Using Acoustic Emission"*(2010), .

[49] *ASTM F2174-02 "Standard Practice for Verifying Acoustic Emission Sensor Response"*(2008), .

[50] Wilcox, P. D., Lee, C. K., Scholey, J. J., Friswell, M. I., Wisnom, M. R. and Drinkwater, B. W. (2006), "Quantitative structural health monitoring using acoustic emission", *Smart Structures and Materials Proc. SPIE* Vol. 6173, .

[51] Lugo, M., Jordon, J. B., Horstemeyer, M. F., Tschopp, M. A., Harris, J. and Gokhale, A. M. (2011), "Quantification of damage evolution in a 7075 aluminum alloy using an acoustic emission technique", *Materials Science and Engineering A,* vol. 528, no. 22-23, pp. 6708-6714.

[52] Han, Z., Luo, H., Cao, J. and Wang, H. (2011), "Acoustic emission during fatigue crack propagation in a micro-alloyed steel and welds", *Materials Science and Engineering A,* vol. 528, no. 25-26, pp. 7751-7756.

[53] Holford, K. M., Pullin, R., Evans, S. L., Eaton, M. J., Hensman, J. and Worden, K. (2009), "Acoustic emission for monitoring aircraft structures", *Proceedings of the Institution of Mechanical Engineers.Part G: Journal of Aerospace Engineering,* vol. 223, no. 5, pp. 525-532.

[54] Atherton, K. J., Paget, C. A. and O'Brien, E. W. (2005), "Structural health monitoring of metal aircrcaft structures with modified acoustic emission"*, Proc. of SEM X International Conference on Experimental and Applied Mechanics,* California, USA.

[55] Rabiei, M. and Modarres, M. (2013), "Quantitative methods for structural health management using in situ acoustic emission monitoring", *International Journal of Fatigue,* vol. 49, pp. 81-89.

[56] Zárate, B.A., Caicedo, J.M., Yu, J. and Ziehl, P., (2012), "Deterministic and probabilistic fatigue prognosis of cracked specimens using acoustic emissions" *Journal of Construction Steel Research,* vol 76, pp. 68-74

[57] Yu, J., Ziehl, P., Zrate, B. and Caicedo, J. (2011), "Prediction of fatigue crack growth in steel bridge components using acoustic emission", *Journal of Constructional Steel Research,* vol. 67, no. 8, pp. 1254-1260.

[58] Kurz, J. H., Grosse, C. U. and Reinhardt, H. -. (2005), "Strategies for reliable automatic onset time picking of acoustic emissions and of ultrasound signals in concrete", *Ultrasonics,* vol. 43, no. 7, pp. 538-546.

[59] Aljets, D., Chong, A., Wilcox, S. and Holford, K. (2012), "Acoustic emission source location on large plate-like structures using a local triangular sensor array", *Mechanical Systems and Signal Processing,* vol. 30, pp. 91-102.

[60] Tobias, A. (1976), "Acoustic-emission source location in two dimensions by an array of three sensors", *Non-Destructive Testing,* vol. 9, no. 1, pp. 9-12.

[61] Spiesberger, J. L. (2001), "Hyperbolic location errors due to insufficient numbers of receivers", *Journal of the Acoustical Society of America,* vol. 109, no. 6, pp. 3076-3079.

[62] Nabney, I. (2002), "Visualization and latent variable models", in Springer, , pp. 225.

[63] Wu, J. (2012), *Advances in k-means clustering,* Springer, New York.

[64] Nabney, I. (2002), "Density modelling and clustering", in Singh, S. (ed.) *Netlab: Algorithms for Pattern Recognition,* Springer, .

[65] Botev, Z.I., Grotowski, J.F. and Kroese, D.P., (2010), "Kernel Density Estimation via Difussion", *Annal of Statistics,* vol 38(5), 2916-2957

[66] Pullin, R., Eaton, M.J., Hensman, J.J., Holford, K.M., Worden, K. and Evans, S.L., (2008), "A principal component analysis of acoustic emission signals from a landing gear component", *Applied Mechanics and Materials,* vols 13-14, pp. 41-47.

[67] Anastassopoulos, A. A., Kouroussis, D. and Tsimogiannis, A. (2000), "Unsupervised Classification of Acoustic Emission Sources from Aerial Man Lift Devices", *WCNDT,* Rome, .

[68] Sause, M. G., Schultheib, D. and Horn, S. (2008), "Acoustic emission investigation of coating fracture and delamination in hybrid carbon fiber reinforced plastic structures", *J.Acoust.Soc.Am.,* , no. 26.

[69] Meriaux, J., Boinet, M., Fouvry, S. and Lenain, J. C. (2010), "Identification of fretting fatigue crack propagation mechanisms using acoustic emission", *Tribology International,* vol. 43, no. 11, pp. 2166-2174.

[70] Suresh, S. (1998), "Continuum mechanics", in *Fatigue of Materials,* Cambridge, , pp. 18.

[71] Knott, J. F. (1973), "Application of fracture mechanics to crack growth by fatigue", in *Fundamental of Fracture Mechanics,* Butterworths, , pp. 234.

[72] Schijve, J., Skorupa, M., Skorupa, A., Machniewicz, T. and Gruszczynski, P. (2004), "Fatigue crack growth in the aluminium alloy D16 under constant and variable amplitude loading", *International Journal of Fatigue,* vol. 26, no. 1, pp. 1-15.

[73] Hudson, M. C. and Scardina, J. T. (1967), *Effect of stress ratio on fatigue crack growth in 7075-T6 aluminium alloy sheet,* N 68-27473, NASA Langley Research Centre.

[74] Totten, G. E. (2008), "Fatigue Crack Propagation", *Advanced Materials and Processes,*May, pp. 39-41

[75] Wang, C. H. (1996), *Introduction to Fracture Mechanics,* DSTO-GD-0103, DSTO Aeronautical and Maritime Research Laboratory, Melbourne.

[76] Huang, X. and Moan, T. (2007), "Improved modeling of the effect of R-ratio on crack growth rate", *International Journal of Fatigue,* vol. 29, no. 4, pp. 591-602.

[77] Broek, D. and Schijve, J. (1965), *The influence of the mean stress on the propagation of fatigue cracks in aluminium alloy sheet,* NLR-TR M2111, Amsterdam.

[78] Hoeppner, D. W. and Krupp, W. E. (1974), "Prediction of component life by application of fatigue crack growth knowledge", *Engineering Fracture Mechanics,* vol. 6, no. 1, pp. 47-70.

[79] Walker, K. (1970), "The effects of stress ratio during crack propagation and fatige", *American Society for Testing and Materials,* vol. 462, pp. 1-14.

[80] Hopkins, S. W., Mitchell, M. R. and Menigault, J. (2005), ""Role of variable amplitude fatigue standards in improving structural integrity"", *ASTM,* vol. STP 1439, pp. 24.

[81] van Dijk, G. M. and de Jonge, J. B. (1975), *Introduction to aFighterAircraftLoadingSTAndard For Fatigue Evaluations - FALSTAFF,* NLR MP 75017 U, National Aerospace Laboratory.

[82] Ono, K., (2006), "AE methodology for the evaluation of structural integrity", *Advanced Materials Research* vols. 13-14, pp. 17-22

[83] Scala, C. M. and Cousland, S. M. (1983), "Acoustic emission during fatigue crack propagation in the aluminium alloys 2024 and 2124", *Materials Science and Engineering,* vol. 61, no. 3, pp. 211-218.

[84] Scruby, C. B., Baldwin, G. R. and Stacey, K. A. (1985), "Characterisation of fatigue crack extension by quantitative acoustic emission", *International Journal of Fracture,* vol. 28, no. 4, pp. 201-222.

[85] Carpenter, S. H. and Higgins, F. P. (1977), "SOURCES OF ACOUSTIC EMISSION GENERATED DURING THE PLASTIC DEFORMATION OF

7075 ALUMINUM ALLOY.", *Metall Trans A,* vol. 8 A, no. 10, pp. 1629-1632.

[86] Cousland, S. M. and Scala, C. M. (1983), "Acoustic emission during the plastic deformation of aluminium alloys 2024 and 2124", *Materials Science and Engineering,* vol. 57, no. 1, pp. 23-29.

[87] Daniel, I. M., Luo, J. -., Sifniotopoulos, C. G. and Chun, H. -. (1998), "Acoustic emission monitoring of fatigue damage in metals", *Nondestructive Testing and Evaluation,* vol. 14, no. 1-2, pp. 71-87.

[88] Rummel, W. D., Todd Jr., P. H., Rathke, R. A. and Castner, W. L. (1974), "DETECTION OF FATIGUE CRACKS BY NONDESTRUCTIVE TEST METHODS.", *Materials Evaluation,* vol. 32, no. 10, pp. 205-212.

[89] Spencer, F. W. (2001), "Estimating Probability of Detection Curves from Regression Data", *Materials Evaluation,* vol. 59, no. 7, pp. 866-870.

[90] Cheng, R. C. H. and Iles, T. C. (1983), "Confidence Bands for Cumulative Distribution Functions of Continuous Random Variables.", *Technometrics,* vol. 25, no. 1, pp. 77-86.

[91] Rocha, B. (2011), *PhD Thesis, Structural Health Monitoring of Aircraft Structures*Universidad Tecnica de Lisboa, Instituto Superiorir Technico, Lisbon, Portugal.

[92] Fasana, A. and Garibaldi, L., (2007), "Measurement of acoustic emission signals: Influence of the couplant", *Key Engineering Materials* vol. 347, pp. 375-380

[93] Yanishevsky, M., Martinez, M., Mandache, C., Khan, M., Fahr, A. and Backman, D. (2010), "Artificial seeding of fatigue cracks in NDI reference coupons", *Insight: Non-Destructive Testing and Condition Monitoring,* vol. 52, no. 12, pp. 664-671.

[94] Auger, F., Flandrin, P., Goncalves, P. and Lemoine, O., (1996), *Time-Frequency Toolbox v1.2 manual.*

[95] Langley, R. B. (1999), "Dilution of precision", *GPS world,* vol. May, pp. 52-59.

[96] Tanaka, K., Hoshide, T. and Sakai, N. (1984), "Mechanics of fatigue crack propagation by crack-tip plastic blunting", *Engineering Fracture Mechanics,* vol. 19, no. 5, pp. 805-825.

[97] Broek, D. (1983), "Summary of basic problems and concepts", in *Elementary Engineering Fracture Mechanics,* 3rd ed, Martinus Nijhoff, The Hague.

[98] *ASTM Standard E 647-00 "Standard test method for measurement of fatigue crack growth rates," ASTM International, West Conshohocken*(2000), .

[99] ESDU 88007 (1993), *Effect of environment on fatigue crack propagation in aluminium alloy sheet and plate,* ISBN 978 0 85679 639 5.

[100] Chang, H., Han, E. H., Wang, J. Q. and Ke, W. (2009), "Acoustic emission study of fatigue crack closure of physical short and long cracks for aluminum alloy LY12CZ", *International Journal of Fatigue,* vol. 31, no. 3, pp. 403-407.

[101] Pullin, R., Holford, K.M. and Evans, S.L., (2007), "Confidence of detection of fracture signals using acoustic emission", *Applied Mechanics and Materials* vols 7-8, pp. 147-152

[102] Hensman, J., Pullin, R., Eaton, M., Worden, K., Holford, K. M. and Evans, S. L. (2009), "Detecting and identifying artificial acoustic emission signals in an industrial fatigue environment", *Measurement Science and Technology,* vol. 20, no. 4.

[103] Carlyle, J. M. and Scott, W. R. (1976), "Acoustic-emission fatigue analyzer - A new acoustic-emission instrument is used to delineate the relationship between sample load, acoustic-emission rate and number of fatigue cycles", *Experimental Mechanics,* vol. 16, no. 10, pp. 369-372.

[104] Scholey, J. J., Wilcox, P. D., Wisnom, M. R. and Friswell, M. I. (2009), "A practical technique for quantifying the performance of acoustic emission systems on plate-like structures", *Ultrasonics,* vol. 49, no. 6-7, pp. 538-548.

[105] Abdi, H. (2010), "Coefficient of variation", in *Encyclopedia of Research Design,* SAGE, Thousand Oaks, CA.

[106] NASA (2008), *Non destructive evaluation requirements for fracture critical components,* NASA-STD-5009, National Aeronautics and Space Administration.

[107] NASA (1985), *Standard NDE guidelines and reuirements for fracture control programs,* MSFC-STD-1249, National Aeronautics and Space Administration.

[108] Newman Jr., J. C. (1984), "A crack opening stress equation for fatigue crack growth", *International Journal of Fracture,* vol. 24, no. 4, pp. R131-R135.

[109] Baram, J. and Rosen, M. (1981), "Prediction of low-cycle fatigue-life by acoustic emission-2: 7075-T6 aluminum alloy", *Engineering Fracture Mechanics,* vol. 15, no. 3-4, pp. 487-494.

[110] Suresh, S. (1998), "Cyclic deformation and crack initiation in noncrystalline solids", in *Fatigue of Materials,* Cambridge, .

[111] Chan, Y. T., Hu, A. G. C. and Plant, J. B. (1979), "A Kalman Filter Based Tracking Scheme with Input Estimation", *Aerospace and Electronic Systems, IEEE Transactions on,* vol. AES-15, no. 2, pp. 237-244.

[112] DALMONT, J. -. (2001), "ACOUSTIC IMPEDANCE MEASUREMENT, PART I: A REVIEW", *Journal of Sound and Vibration,* vol. 243, no. 3, pp. 427-439.

[113] Eaton, M. J., Pullin, R., Hensman, J. J., Holford, K. M., Worden, K. and Evans, S. L. (2011), "Principal component analysis of acoustic emission signals from landing gear components: An aid to fatigue fracture detection", *Strain,* vol. 47, no. SUPPL. 1, pp. e588-e594.

[114] Farrar, C. R. and Worden, K. (2007), "An introduction to structural health monitoring", *Philosophical Transactions of the Royal Society A,* vol. 365.

[115] Ihn, J.-B., Chang, F.-. and Speckmann, H., (2001), "Built-in diagnostics for monitoring crack growth in aircraft structures", *Key Engineering Matrials*, vols. 204-205, pp. 299-308

[116] Lin, M., Qing, X., Kumar, A. and Beard, S. J. (2001), "SMART Layer and SMART Suitcase for structural health monitoring applications", Vol. 4332, pp. 98.

[117] Fan, W. and Qioa, P. (2010), "Vibration-based Damage Identification Methods: A Review and Comparative Study", *Structural Health Monitoring,* vol. 0, no. 0, pp. 1-29.

[118] Doebling, S. W., Farrar, C. R. and Prime, M. B. (1998), "A summary review of vibration-based damage identification methods", *Shock and Vibration Digest,* vol. 30, no. 2, pp. 91-105.

[119] Wheatley, G., Kollgaard, J., Register, J. and Zaidi, M. (2003), "Comparative vacuum monitoring as an alternate means of compliance", *Structural Health Monitoring 2003: From Diagnostics & Prognostics to Structural Health Management: Proceedings of the 4th International Workshop on Structural Health Monitoring, Stanford University, Stanford, CA, September 15-17*

[120] Roach, D. (2009), "Real time crack detection using mountable Comparative Vacuum monitoring sensors", *Smart Structures and Systems,* vol. 5, no. 4, pp. 317-328.

[121] Zagrai, A. and Giurgiutiu, V. (2002), "Health monitoring of aging aerospace structures using the electro-mechanical impedance method", Vol. 4702, pp. 289.

[122] Zagrai, A. N. and Giurgiutiu, V. (2001), "Electro-mechanical impedance method for crack detection in thin plates", *Journal of Intelligent Material Systems and Structures,* vol. 12, no. 10, pp. 709-718.

[123] Giurgiutiu, V. and Rogers, C. A. (1998), "Recent advancements in the electro-mechanical (E/M) impedance method for structural health monitoring and NDE", Vol. 3329, pp. 536.

[124] Yang, Y., Liu, H. and Annamdas, V. G. M. (2009), "Wireless sensing using piezo-ceramic transducers for structural health monitoring", *Sensors and Smart Structures Technologies SPIE Proc.* Vol. 7292, .

[125] Cobb, A. C., Michaels, J. E. and Michaels, T. E. (2009), "Ultrasonic structural health monitoring: A probability of detection case study", *Proc. 35th Annual Review on Progress in Quantitative Nondestructive Evaluation,* 20-25 July 2005, Vol. 1096, pp. 1800.

[126] Zagrai, A., Donskoy, D., Chudnovsky, A. and Golovin, E. (2006), "Nonlinear acoustic structural health monitoring", Vol. 11, pp. 7897.

[127] Sabra, K. G., Srivastava, A., Lanza Di Scalea, F., Bartoli, I., Rizzo, P. and Conti, S. (2008), "Structural health monitoring by extraction of coherent guided waves from diffuse fields", *Journal of the Acoustical Society of America,* vol. 123, no. 1, pp. EL8-EL13.

[128] Yu, L. and Giurgiutiu, V. (2005), "Multi-damage detection with embedded ultrasonic structural radar algorithm using piezoelectric wafer active sensors through advanced signal processing", *Health Monitoring and Smart Nondestructive Evaluation of Structural Systems SPIE Proc.* Vol. 5768, pp. 406.

[129] Cornwell, P., Doebling, S. W. and Farrar, C. R. (1999), "Application of the strain energy damage detection method to plate-like structures", *Journal of Sound and Vibration,* vol. 224, no. 2, pp. 359-374.

[130] Sun, F. P., Chaudhry, Z. A., Rogers, C. A., Majmundar, M. and Liang, C. (1995), "Automated real-time structure health monitoring via signature pattern recognition", *Smart Structures and Materials SPIE Porc.* Vol. 2443, pp. 236.

[131] Sodano, H. A. (2007), "Development of an automated eddy current structural health monitoring technique with an extended sensing region for corrosion detection", *Structural Health Monitoring,* vol. 6, no. 2, pp. 111-119.

[132] Fowler, T., Blessing, A., Conlisk. P., and Swansong, T., “The Monpac System”, *Journal of Acoustic Emission,* 8(3), 1-8(1989)